PH.D. THESIS

GENOMIC AND GENETIC DISSECTION OF PHEOCHROMOCYTOMA AND PARAGANGLIOMA

AGUIRRE A. DE CUBAS

MADRID, MMXIV

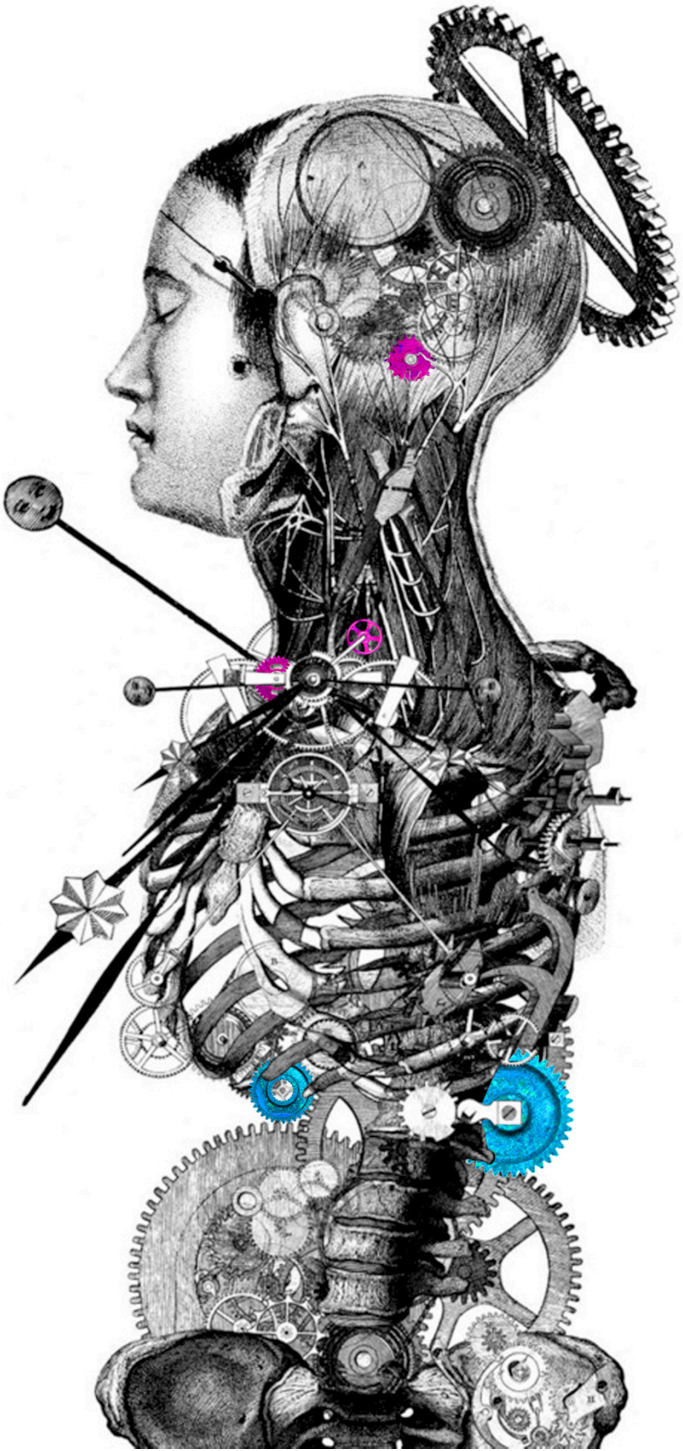

Cover art by Aguirre A. de Cubas, modified original works of "Timenaut Male" and "Timenaut Female" by Paula Braconnot.

UNIVERSIDAD AUTONOMA DE MADRID

DEPARTMENT OF MOLECULAR BIOLOGY
FACULTY OF SCIENCE
AUTONOMOUS UNIVERSITY OF MADRID

GENOMIC AND GENETIC DISSECTION OF PHEOCHROMOCYTOMA AND PARAGANGLIOMA

AGUIRRE A. DE CUBAS

MADRID, MMXIV

DEPARTMENT OF MOLECULAR BIOLOGY
FACULTY OF SCIENCE
AUTONOMOUS UNIVERSITY OF MADRID

GENOMIC AND GENETIC DISSECTION OF PHEOCHROMOCYTOMA AND PARAGANGLIOMA

Doctoral thesis submitted to the Autonomous University of Madrid for the Degree of Doctor of Philosophy (Ph.D.) in Biomolecular Sciences in possession of the following credencials:

M.Sc. in Molecular and Cellular Biology,
B.Sc in Biochemistry,
B.Sc. in Chemistry.

Aguirre Andrés de Cubas

Thesis director
Dr. Mercedes Robledo, Ph.D.

HEREDITARY ENDOCRINE CANCER GROUP
HUMAN CANCER GENETICS PROGREAMME
SPANISH NATIONAL CANCER RESEARCH CENTRE (CNIO)

Centro Nacional de Investigaciones Oncológicas
Melchor Fernández Almagro, 3
E-28029 Madrid, Spain
tel. (+34) 91 224 69 00 ext.3320

FACULTAD DE CIENCIAS
UNIVERSIDAD AUTÓNOMA DE MADRID
Cuidad Universitaria de Cantoblanco
E-28049 Madrid, Spain
tel. (+34) 91 497 48 66

Dr. Mercedes Robledo Batanero, Investigador Primario de Grupo de Cancer Endocrino Hereditario del Centro Nacional de investigaciones Oncológicas (CNIO)

CERTIFICA:

Que Don Aguirre Andres de Cubas, Máster en Biología Molecular por la Universidad de Zaragoza, ha realizado la presente Tesis Doctoral, "**Genomic and Genetic dissection of pheochromocytoma and paraganglioma**" y que a su juicio reúne plenamente todoss los requisitos necessarios para optar al Grado de Doctor (Ph.D) en Biociencias Moleculares, a cuyos efectors será presentado en la Universidad Autónoma de Madrid. El trabajo ha sido realizado bajo mi dirección, autorizando su presentación ante el Tribunal Calificador.

Y para que así conste se extiende el presente certificado,

Madrid, octubre 2014

Madrid, octubre 2014

V° B° del director de la Tesis:

Dr. Mercedes Robledo, Ph.D.
PI Hereditary Endocrine Cancer Lab

V° B° del Tutor de la Tesis

Dr. José Manuel Cuezva, Ph.D.
Dir. Dpt. Molecular & Cell Biology

This thesis, submitted for the degree of Doctor of Philosophy (Ph.D.) in Biomolecular Sciences at the Autonomous University of Madrid, has been elaborated in the Hereditary Endocrine Cancer laboratory at the Spanish National Cancer Research Centre (CNIO), under the tutorship of Dr. José Manuel Cuezva, M.D., Ph.D., and the supervision of Dr. Mercedes Robledo, Ph.D.

This work was supported by the following grants and fellowships:

- La Caixa/CNIO International PhD Fellowship, 2009-2013; Aguirre A. de Cubas
- Fundación Mutua Madrileña, (project AP2775/2008)
- Fondo de Investigaciones Sanitarias (projects PI080883 and PI11/01359)
- European Network for the Study of Adrenal Tumors (ENS@T) - European Union Seventh Framework Programme (FP7/2007-2013) under grant agreement no. HEALTH-F2-2010-2597

DEDICATION

I dedicate this work to my parents and Luisa, who have always supported me during the good times, as well as the bad times. Words are not enough and cannot express my gratitude, appreciation, and love for you all.

I would like to dedicate this work to my loving son Oliver. Maybe you'll read this some day... or not.

Maluli, Carolina, Adri, Gus, Julian, Mia, Gerardo for you support.

I dedicate this to my dog Titi. You accompanied me during my Ph.D.

The palest ink is better

than the best memory

-Chinese proverb

ACKNOWLEDGEMENTS

To all those whom have provided me with guidance during these years...

Hereditary Endocrine Cancer Lab: Cristina Rodríguez, Alberto Cascón, Lucía Inglada Pérez, Alvaro Gómez-Grana, Rocio Leton Luis-Javier Leandro, Iñigo Landa, Veronica Mancikova, Maria Curras, Iñaki Comino, María Valvanera Apellániz, Susanna Leskelä, ect.

Fernando Peláez, Irene Orcera, and Celia María Ramos.

Human Genomic Programmme: Ana Osorio, Maria José García, Alicia Barroso, Victoria Fernández, Carlos Benítez, Nerea Matamala, Beatriz Paumard, Oriol Calvete, Javier Gayarre, Alejandra Tavera, Miljana Tanic, kira Yanowsky, Tereza Vaclova, and Marta Kamieniak.

Molecular Cytogenetics Lab: Juan Cruz Cigudosa, Miguel Angel Grillo, Carmen Carralero, Ana Del Rio, Sandra Rodríguez, Luís Espinosa, Mari Carmen Martín, Rocío Salgado, Alba Maiques Diaz, Juliane Menezes, and Francesco Acquadro.

Familial Cancer Unit: Miguel Urioste, Fátima "Fatimower" Mercadillo, Samuel Domingo, Laura and Saucedo-Cuevas, Bárbara Rivera.

Genomics Unit: Orlando Domínguez, Guadalupe Luengo, Purificación Arribas, Jorge Monsech, and Ángeles Rubio..

Confocal Microscopy Core Unit: Diego Megías, Manuel Pérez, and Joaquim Soriano.

Human Genotyping-CEGEN Unit: Anna González-Neira, Rosario Alonso, Leticia Moreno, Guillermo Pita, Belén Herráez, Nuria Álvarez, Daniela Caronia, and Sara Ruíz.

Genetic & Molecular Epidemiology Group: Núria Malats, Jose Carlos Martínez, Paulina Gómez, María Evangelina López de Maturana, Alexandra Masson-Lecomte, Silvia Pineda, Ana Alfaro, María Encarnación Castillo, Mirari Márquez, and Marta Rava.

Proteomics Core Unit: Javier Muñoz, Maria Pilar Ximénez de Embún, Nuria Ibarz, Fernando García, Mª Isabel Ruppen, Jorge Luís Martínez.

Dr. Mónica Marazuela Azpíroz, Ignacio Pérez de Castro, Marcos Malumbres, Luis Lombardia, Eamonn Maher, Michele Cioffi, Krishna seshu. T., Maria S Soengas, Alejandro Ibáñez-Costa and Paola Martinelli.

Paz Bardaji Vital and David Carbonel.

To those that taught and inspired my formation in Bioinformatics: David Pisano, Gonzalo Gómez, Daniel Rico, Milana Frenkel-Morgenstern, Osvaldo Graña, Jorge Valencia, Juan Ramón González Ruiz, Marcos López Sánchez, Lucas A Salas, and Laia Paré Brunet.

The members of the European Network for the Study of Adrenal Tumors (ENS@T).

Esther Korpershoek, Felix Beuschlein, Heni Timmers, Massimo Manelli, Enzo, Jérôme Bertherat, Wiebke Arlt, Enzo Lalli, Ronald de Krijger, Richard Sinnott, Judith Favier, Lindsey Oudijk, Marco Volante, Anouk van Berkel, Daniel Tennant, Thomas Papathomas, and Anthoney Stell

Carl Steinbeißer.

Karel Pacak and Stephanie Fliedner.

Nan Qin.

La "CAIXA/CNIO" International Ph.D. Fellowship Award, which made all this Possible.

Paula Braconnot for her "Timenaut Male" and "Timenaut Female" works that I modified for my cover.

Patricia Dahia and her team for their contributions in this field, and also a source of inspiration.

The Departament of Biochemistry and Molecular & Cellular Biology at the University of Zaragoza, especially Miguel Pocoví and Isabel De Castro-Orós at the Lipid Biochemistry Lab. Here I initiated my odyssey in this field.

ACKNOWLEDGEMENTS

A special thanks to my Mentors:

- Ramee Indralingam, Harry Price, Alicia Schultheis, Tandy Grubbs, and Pete Hauck at Stetson University for encouraging me to pursue a career in research, rather than medicine.

- Mercedes Robledo her excellent mentorship, kindness, and patience.

- Javier Benítez for his wisdom and valuable guidance. Truely, a source of inspiration.

- Graeme Eisenhofer for the knowledge and inspiration he enparted with me. You thaught me that sometimes you have to think outside the box.

- José Manuel Cuezva, not just my UAM tutor, but also a source encouragement.

SUMMARY IN ENGLISH

Pheochromocytoma and paraganglioma (PPGL) are rare neuroendocrine tumors, with a strong genetic component, that comprises fifteen genes so far. The advent of high-throughput technologies have permitted the simultaneous interrogation of thousands biomolecules. As expected, these technologies have already been applied to study PPGL, as well as virtually every known pathology. However, some molecular events, such as miRNA expression and DNA methylation, have not yet been explored when this thesis project began in autumn 2009.

In the first part of this study, we explored microRNA expression in PPGL, and demonstrated that PPGLs express different miRNA signatures according to genetic background. As a matter of fact, it was possible to identify and validate several miRNAs associated with the primary mutation, as well as miRNAs common among PPGLs, which could potentially be used to guide genetic study. Among the most significant finding was the validation of SDHB-specific miRNA-183/96, which has gained interest lately among the PPGL research community.

The second part of this thesis involved the use of bioinformatics integrative study of miRNA-mRNA interactions, which indicated neuronal differentiation as a common theme deregulated in PPGL pathogenesis. This was validated by functional analyses showing miR-183/-96 impeded NGF-induced neuronal differentiation of immature chromaffin cells (PC12 cells). Proteomic studies, initially included to validate our bioinformatics integration methods, also revealed the antagonistic effect of miR-183/96 on NGF-induced chromaffin cell differentiation might results from disruption of growth factor-induced RAS activation as suggested by proteomic analyses.

In part three, we analyzed chromosomal alterations in PPGL using SNP-arrays, which enabled us to detect copy neutral events, including chromosome 14 disomy in MAX mutant tumors. We observed and verified previously described chromosomal aberrations in PPGL. Finally, we integrated miRNA, mRNA, SNP-array, and methylation data to obtain a more complete prospective of the molecular events at chromosome 14 in MAX mutant tumors, which the author not only believes it provides the means for the second hit of the MAX gene, but also results the loss of other tumor suppressive genes or gain of imprinted oncogenes.

For fourth and final part, we explored DNA methylation patterns in the context of PPGL malignancy, as well as in tumors of diverse genetic backgrounds. Our results demonstrated that DNA methylation patterns differed according to PPGL genotype, and verified previous data showing global hypermethylation in SDHx-related tumors. Most importantly, we identified and validated 52 CpGs associated with malignant behavior in an independent cohort of which forty-eight CpGs showed significant associations with progression free survival. Finally, it was possible to suggest RDBP hypermethylation as a predictor of malignancy, as it was further confirmed in malignant PPGL by pyrosequencing in an independent series of FFPE archival samples.

In summary, we have applied numerous high-throughput genomic technologies to study PPGL. These studies have revealed much about the molecular mechanisms behind these tumors, as well demonstrate how genomic technologies, if applied correctly, can compliment and foment research.

RESUMEN EN ESPAÑOL

Los feocromocitomas y paragangliomas (PPGL) son tumors neuroendocrinos raros, que tienen un fuerte componente genético, en el que intervienen hasta quince genes descritos hasta la fecha. Las tecnologías de alto rendimiento permiten interrogar miles de moléculas de forma simultánea, y ya han sido aplicadas al estudio de PPGLs. Sin embargo, algunos eventos moleculares, como la expresión de microRNAs y eventos de metilación, no habían sido explorados cuando este proyecto de tesis comenzó en otoño de 2009.

En la primera parte de este estudio demostramos que los PPGLs expresan diferentes firmas de microRNAs de acuerdo al fondo genético. De hecho fue posible identificar y validar microRNAs comunes a todos los PPGLs, así como específicamente asociados con la mutación primaria, que por tanto podrían ser potencialmente usados para guiar el estudio genético.

La segunda parte de esta tesis planteó una integración bioinformática de interacciones miRNA-mRNA, que señaló la diferenciación neuronal como proceso central relacionado con la patogénesis de estos tumores. Ensayos funcionales con células PC12 demostraron que los microRNAs -183/-96 afectaban la diferenciación neuronal, posiblemente como consecuencia de la desregulación del factor de crecimiento inducido por la activación de RAS, según se desprendía de análisis proteómico.

En la tercera parte se caracterizaron alteraciones cromosómicas presentes en PPGLs utilizando SNP-arrays, que permitieron además detectar disomías uniparentales, como la que afecta al cromosoma 14 en los tumores asociados a mutaciones en MAX. Integramos los resultados procedentes de arrays de miRNA, mRNA, SNP-array, y datos de metilación para obtener una perspectiva completa de los eventos moleculares que afectan al cromosoma 14 en los tumores MAX.

En la cuarta parte analizamos los patrones de metilación asociados tanto al desarrollo de metástasis, como al fondo genético. Nuestros resultados verificaron la existencia de un patrón hipermetilado asociado a mutaciones en los genes SDH, mostraron que la metilación difería según el genotipo, y permitieron identificar y validar 52 islas CpGs asociadas a metástasis. De ellas, 48 mostraron tener un papel predictivo de progresión libre de enfermedad. Entre ellas, se pudo validar la hipermetilación de RDBP asociada a malignidad en una tercera serie independiente de tumores, observación que permitió proponer este marcador como predictor de metástasis.

En resumen, la aplicación de plataformas genómicas de alto rendimiento al estudio de PPGLs ha permitido descifrar mecanismos moleculares implicados en su patogénesis.

TABLE OF CONTENT

ABBREVIATIONS

2-OG: 2-oxoglutarate, or α-ketoglutarate
5mC: 5-methylcytosine
A-CGH: Array-comparative genomic hybridization
ABAT: 4-aminobtyrate aminotransferase
aCGH: Array-comparative genomic hybridization
ACO1: Aconitase 1
ADSSL1: Adenylosuccinate synthase like 1
AKT: v-akt murine thymoma viral oncogene homolog 1
ANOVA: Analysis of variance
APAF: Tumor protein p53
aPKC: atypical protein kinase C
ARHGAP18: Rho GTPase-activating protein 18
ARHGAP26: Rho GTPase activating protein 26
ARHGEF9: Cdc42 guanine nucleotide exchange factor 9
arrayCGH: Array-comparative genomic hybridization
ASCAT: Allele-specific copy number analysis of tumors
BAK1: BCL2-antagonist/killer 1
BCL2: B-cell CLL/lymphoma 2
BDNF: Brain-derived neurotrophic factor
BMP2: Bone morphogenetic protein 2
BMP7: Bone morphogenic protein 7
BMPR1B : BMP receptor type 1B
BRCA1: Breast cancer 1, early onset
BRCA2: Breast cancer 2, early onset
C-JUN: Jun proto-oncogene
CALM1: Calmodulin 1
CAMK2G: Calcium/calmodulin-dependent protein kinase II gamma
cAMP: Cyclic adenosine monophosphate
cAMP: Cylic AMP
CCND1: Cyclin D1
CDC42: cell division cycle 42
CDH: Cadherin
CDH6: Cadherin 6, type 2, K-cadherin (fetal kidney)
CDK2: Cyclin-dependent kinase 2
CDKN2A: Cyclin-dependent kinase inhibitor 2A
CDKN2B: Cyclin-dependent kinase inhibitor 2B (p15, inhibits CDK4)
CGH: Comparative genomic hybridization
CGI: CpG islands
CHEK1: Checkpoint kinase 1
CIMP: CpG island hypermethylator phenotype
Cluster 2: Contains RET, NF1, MAX, TMEM127, and HRAS mutant tumors
CNIO: Spanish National Cancer Research Centre
CNS: Central nervous system
COBRA1: Cofactor of BRCA1, or NELFB
CpG: Cytosine followed by guanine in 5' to 3' direction
CREB: cAMP responsive element binding protein
CREB5: cAMP responsive element binding protein 5
CREB5: cAMP responsive element binding protein 5
CRK: V-crk sarcoma virus CT10 avian oncogene homolog
CS: Citrate synthase
CSNK1E: Casein kinase 1, epsilon
CTDSP1: CTD small phosphatase 1
CYFIP2: Cytoplasmic FMR1 interacting protein 2
DAPK1: Death-associated protein kinase 1
DAPK2: Death-associated protein kinase 2
DBR: David Bioinformatics Resourses
DICER1: Dicer 1, ribonuclease type III
DLK1: Delta-like kinase 1
DMR: Differentially methylated region
DNA: Deoxyribonucleic acid
DS: Discovery Series
DSIF: DRB-sensitive factor complex
DWI_MRI: diffusion-weighted MRI
ECM: Extracellular matrix
EGF: Epidermal growth factor
EGFR: Epidermal growth factor receptor
EGLN1: Egl-9 family hypoxia-inducible factor 1, or PHD2
EGLN2: Egl-9 family hypoxia-inducible factor 1, or PHD1
EGLN3: Egl-9 family hypoxia-inducible factor 3, or PHD3
ENS@T: European Network for the Study of Adrenal Tumors
EPAS1: Endothelial PAS domain protein 1, or HIF2α
ERK5: Mitogen-activated protein kinase 7, or MAPK7
EtOH: Ethanol
EZR: Ezrin
FAK: Focal adhesion kinase
FARP1: FERM, RhoGEF (ARHGEF) and pleckstrin domain protein 1
FAS: Fas cell surface death receptor
FDA: 6-[18F]fluorodopamine
FDG: 2-[18F]fluoro-2-deoxy-D-glucose
FDR: False discovery rate
FFPE: Formalin fixed paraffin embeded
FH: Fumarate hydratase
FOXO3: Forkhead box O3
FRZB: Frizzled-related protein
FSCN1: Fascin homolog 1
FYN: FYN proto-oncogene, Src family tyrosine

kinase
GAB2: GRB2-associated binding protein 2
GABA: Gamma-aminobutyric acid
GABRB3: GABA A receptor B3
GABRG2: GABA A receptor G2
GDNF: Glial cell line-derived neurotropic factor
GEO: Gene expression omnibus
GEO: Gene expression Omnibus
GPR61: G protein-coupled receptor 61
GSTP1: Glutathione S-transferase pi 1
GWAS: Genome wide association studies
HDAC11: Histone deacetylase 11
HDAC3: Histone deacetylase 3
HIF: Hypoxia inducible factor, 1 or 2
HIF1: HIF1α-HIFβ heterodimer transcription factor
HIF1α: Hypoxia inducible factor 1, alpha subunit
HIF2: HIF2α-HIFβ heterodimer transcription factor
HIF2α: Hypoxia inducible factor 1, alpha subunit, or EPAS1
HRAS: Harvey rat sarcoma viral oncogene homolog) gene
HSPC300: BRICK1, SCAR/WAVE actin-nucleating complex subunit, or BRK1
HTRA2: HtrA serine peptidase 2
IDH1: Isocitrate dehydrogenase 1 (NADP+), soluble
IDH2: Isocitrate dehydrogenase 2 (NADP+), mitochondrial
IGF2: Insulin-like growth factor 2 (somatomedin A)
INPP4A: Inositol polyphosphate-4-phosphatase, type I, 107kDa
IRB: Institution review board
ITGA6: Integrin, alpha 6
JUNB: Jun B proto-oncogene
KDM5B: Histone H3 Lys4 demethylase
KIF1Bβ: Kinesin family member 1B
KRAS: Kirsten rat sarcoma viral oncogene homolog
LGI1: Leucine-rich, glioma inactivated 1
LOH: Loss of heterozygosity
LZTS1: Leucine zipper, putative tumor suppressor 1
MAGIA: miRNAs and genes integrated analysis
MAPK11: Mitogen-activated protein kinase 11
MAPK7: Mitogen-activated protein kinase 7, or Erk5
MAPT: microtubule-associated protein tau
MAX: MYC associated factor X
MCM5: Mini-chromosome maintenence protein 5
MEG3: Maternally expressed gene 3
MEN1: Multiple endocrine neoplasia I
MEN1: Multiple endocrine neoplasia syndrome type 1
MEN2: Multiple endocrine neoplasia syndrome type 2
MEN2A: Multiple endocrine neoplasia, type 2A
MEN2B: Multiple endocrine neoplasia, type 2B
MIBG: [123/131I]-metaiodobenzylguanidine
miR: MicroRNA
miRNA: MicroRNA or micro-ribonucleic acid
MRI: magnetic resonance imaging
mRNA: Messenger ribonucleic acid
MSP: Methylation-specific PCR
MSX1: Msh homeobox 1
MTHFD2: Methylenetetrahydrofolate dehyrogenase 2
mTOR: Mechanistic target of rapamycin (serine/threonine kinase)
MYC: V-myc avian myelocytomatosis viral oncogene homolog
MYCL: V-myc avian myelocytomatosis viral oncogene lung carcinoma derived homolog
NCOR1: Nuclear receptor corepressor 1
NELFB: Negative elongation factor complex member B
NF1: Neurofibromatosis type 1
NGF: Nerve growth factor
nMA: Normal adrenal medulla
NMYC: V-myc avian myelocytomatosis viral oncogene neuroblastoma derived homolog
NOXA: Phorbol-12-myristate-13-acetate-induced protein 1, or PMAIP1
NPFF: Neuropeptide FF-amide peptide precursor
NRAS: Neuroblastoma RAS viral (v-ras) oncogene homolog
NSF: N-ethylmaleimide-sensitive factor
NTRK1: Neurotrophic tyrosine kinase, receptor, type 1
OMIC: High-throughput genomic technology
OXCT1: 3-oxoacid CoA transferase 1
P19: Stem cells
P53: Tumor protein p53
PAI1: Serpin peptidase inhibitor, clade E, member 1, or SERPINE1
PASS: Pheochromocytoma of the adrenal gland scaled score
PC: Pyruvate carboxylase
PC12: Rat pheochromocytoma cell line
PDH: Proline hydroxylase
PDH2: Proline hydroxylase 2, or EGLN1
PDH3: Proline hydroxylase 3, or EGLN3
PET: positron emission tomography
PFS: Progression-free survival
PGBD3: PiggyBac transposable element derived 3
PGL-: Paraganglioma-pheochromocytoma syndromes (PGL)
PGL1: Paraganglioma-pheochromocytoma syndrome 1 caused by SDHD mutations
PGL2: Paraganglioma-pheochromocytoma syndrome 2 caused by SDHAF2 mutations

PGL3: Paraganglioma-pheochromocytoma syndrome 3 caused by SDHC mutations
PGL4: Paraganglioma-pheochromocytoma syndrome 4 caused by SDHB mutations
PGL5: Paraganglioma-pheochromocytoma syndrome 5 caused by SDHAF2 mutations
PI3K: phosphatidylinositol 3 kinase
PIK3R1: Phosphoinositide-3-kinase regulatory subunit 1 alpha
Pitx3: Paired-like homeodomain 3
PLCB4: Phospholipase C beta 4
PMAIP1: Phorbol-12-myristate-13-acetate-induced protein 1, or NOXA
PNMT: Phenylethanolamine N-methyltransferase
PPGL: Pheochromocytoma and paraganglioma
PPP2R5C: Protein phosphatase 2, regulatory subunit B', gamma
PRDX6: Peroxiredoxin 6
PRKCA: Protein kinase C, alpha
PRKCD: Protein kinase C, delta
PSEN1: Presenilin 1
PTEN: Phosphatase and tensin homolog
pVHL: von Hippel-Lindau (VHL) gene product
PYGO1: Pygopus family PHD finger 1
RASSF1: Ras association (RalGDS/AF-6) domain family member 1
RB1: Retinoblastoma 1
RCC: Renal cell carcinoma
RDBP: Negative elongation factor complex member E, or NELFE
RDX: Radixin
REST/NRSF: RE1-silencing transcription factor
RET: Ret proto-oncogene
RISC: RNA induced gene silencing complex
RNA: Ribonucleic acid
RUNX2: Runt-related transcription factor 2
SALL4: Spalt-like transcription factor 4
SDH: Succinate dehydrogenase, part of Complex 2 of electron transport chain
SDHA: Subunit A of succinate dehydrogenase
SDHAF2: Subunit AF2 of succinate dehydrogenase
SDHB: Subunit B of succinate dehydrogenase
SDHC: Subunit C of succinate dehydrogenase
SDHD: Subunit D of succinate dehydrogenase
SDHx: Succinate dehydrogenase, subunit x
SERPINE1: Serpin peptidase inhibitor, clade E, member 1, or PAI1
SGSH: N-sulfoglucosamine sulfohydrolase
SHC1: Src homology 2 domain containing transforming protein 1
SLC6A2: Solute carrier family 6 (neurotransmitter transporter), member 2
SNP-A: SNP-array
SORCS1: sortilin-related VPS10 domain containing receptor 1
SPOCK2: Sparc/osteonectin, cwcv and kazal-like domains proteoglycan (testican) 2
SRC: SRC proto-oncogene, non-receptor tyrosine
STMN1: Stathmin 1
Succ: Succinate
T47D: Breast cancer cell line
TCF7: Transcription factor 7 (T-cell specific, HMG-box)
TET: Tet methylcytosine dioxygenase
TH: Tyrosine hydroxylase
TLN2: Talin
TMEM127: Transmembrane protein 127
TNFRSF1A: Tumor necrosis factor recpetor superfamily member 1A
TP73: Tumor protein p73
TRAK1: Trafficking protein, kinesin binding 1
TUB: Tubby bipartite transcription factor
UPD: Unipaternal dissomy, or copy neurtal duplication
UTR: Untranslated region
VHL: von Hippel-Lindau
VHL/SDH: Cluster 1 containing VHL- and SDHx-related
VLDLR: Very low density lipoprotein receptor
VS1: Validation Series 1 (COMETE cohort)
VS1: Validation Series 1; COMETE Series tumors
VS2: Validation Series 2
VS2: Validation Series 2; FFPE tumors for validation by pyrosequencing
WNT: Wingless-type MMTV integration site family member
WNT10A: Wingless-type MMTV integration site family, member 10A
WNT6: Wingless-type MMTV integration site family, member 6
WT: Wild type (no mutation in known PPGL susceptibility genes)

墨: Chinese symbol for "Ink" (Mandarine)

1. INTRODUCTION

1.1. General aspects of pheochromocytoma & paraganglioma

Pheochromocytoma (PCC) is a rare neuroendocrine tumor of neural crest origin derived from chromaffin cells of the adrenal medulla (Figure 1.1.). Paraganglioma (PGL), a closely related tumor, arise from the paraganglia of the autonomic nervous system, which are distributed throughout the body and play an important role in oxygen homeostasis [1]. PGLs can be subdivided into sympathetic or parasympathetic based on their location. Parasympathetic PGLs develop in the head and neck region and can be located in the carotid body, in the vagal body, in the jugulotympanic region, in the superior and inferior laryngeal paraganglionic tissues, in the nasal cavity, or in the orbit (Figure 1.1.). Sympathetic PGLs are located in the thorax, abdomen, pelvis, and urinary bladder (Figure 1.1.). Head and neck PGLs are associated with the parasympathetic nervous system and usually lack endocrine activity. Collectively, PCC and PGLs are referred to as PPGLs.

On the other hand, sympathetic PGL, as well as PCC, are more closely associated with the sympathetic nervous system, and often secrete higher levels of catecholamine [1]. As a result, many patients with PPGL present continuously or paroxysmal increase in blood pressure due excessive catecholamine secretion [2]. Thus, the majority of our research efforts focused primarily on those tumors related to (or derived from) the sympathetic nervous system.

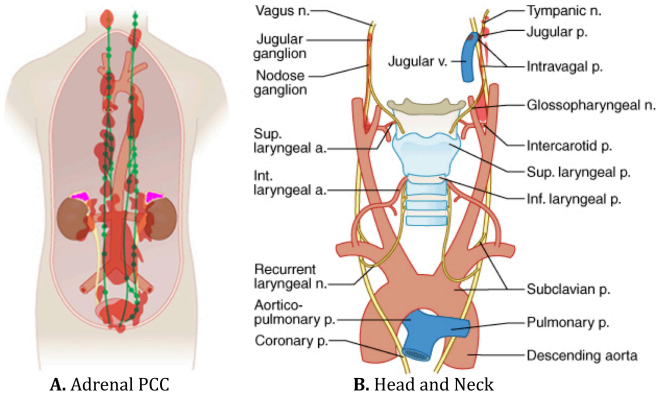

Figure 1.1. The paraganglial system. Topographic sites of PCCare indicated in pink, and PGLs indicated in red. A) Adrenal PCC. Extra-adrenal PCC, now called sympathetic PGL. B) parasympathetic PGL located in the head and neck region.

1.2. Genetics of pheochromocytoma & paraganglioma

PPGL can occur sporadically, or in the context of hereditary syndromes, such as von Hippel-Lindau (VHL) syndrome, multiple endocrine neoplasia type 2 (MEN2), neurofibromatosis type 1 (NF1), and paraganglioma-pheochromocytoma syndromes (PGL) 1, 2, 3, & 4. Since the discovery of *NF1* as the first PPGL susceptibility gene, numerous other genes have been identified in which mutations confer susceptibility to develop these tumors (Figure 1.2.). Table 1.1 gives an overview of the known genes involved in PPGL.

Table 1.1. PPGL susceptibility genes

Affected gene	Chromosome location	Related syndrome	Associated tumors
NF1	17q11.2	NF1	PPGL, cutaneous/dermal neurofibromas and Lisch nodules (pigmented iris hamartomas)
RET	10q11	MEN2	PPGL, MTC
VHL	3p25.3	VHL	PPGL, retinal and CNS HB, RCC, neuroendopancreatic cystoadenoma, renal cysts, endolymphatic sac tumors, and PET
MEN1	11q13	MEN1	PPGL, parathyroid adenomas, nonfunctioning PET, gastrinomas, and insulinomas, bronchial carcinoids
SDHD	11q23	PGL1	PPGL
SDHC	1q21-23	PGL3	PPGL
SDHB	1p36	PGL4	PPGL, GIST, and RCC
KIF1Bβ	1p36	fPPGL	PPGL, NB
EGLN1	14q13.1	fPPGL	PPGL
SDHAF2	11q23	PGL5	PPGL
TMEM127	2q11.2	fPPGL	PPGL, RCC
SDHA	5p15	fPPGL	PPGL
MAX	14q23	fPPGL	PPGL, lung carcinoma
EPAS1	2p21-p16	-[1]	PPGL
FH	1q42.1	fPPGL	PPGL
HRAS	11p15.5	-[1]	PPGL, numerous others

1) Genes somatically mutated in PPGL and are not part of familial disease. fPPGL: familial PPGL, MTC: medullary thyroid carcinoma; CNS: central nervous system; HB: hemangioblastoma; RCC: renal cell carcinoma; PET: pancreatic neuroendocrine tumor; GIST: gastrointestinal stromal tumor; NB: neuroblastoma

Originally, it was thought that 10% of PPGLs were hereditary, but research over the past decade and a half has shown that this proportion is currently close to 40% (Table 1.1). In addition, recent findings have demonstrated that 40% of PPGL will exhibit somatic mutations at these same genes. Thus, recent evidences show that at least 60% of PPGLs will have germline or somatic mutations in the genes in table 1.1. It is expected that this percentage will rise as the contribution of novel susceptibility genes, such as *EPAS1* and *HRAS*, becomes known.

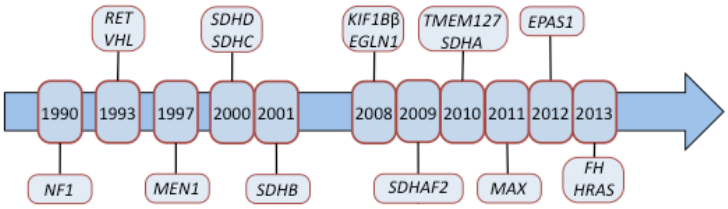

Figure 1.2. Timeline of PPGL susceptibility gene discovery.

1.2.1. Von Hippel-Lindau Syndrome

Von Hippel-Lindau (VHL) disease is an autosomal, dominantly inherited neoplastic disorder that demonstrates marked phenotypic variability [3]. VHL disease is caused by mutations in the *VHL* tumor suppressor gene, located on chromosome 3p25-26 [4]. The prevalence of this disease has been estimated to 2-3 per 100,000 individuals in the general population [3].
The most frequent tumors are retinal and central nervous system (CNS) hemangioblastomas, renal cell carcinomas (RCC), PPGL, pancreatic islet tumors, and endolymphatic sac tumors [5], although other lesions such as pancreatic neuroendocrine tumors (PETs) or broad ligament tumors can also appear. Interestingly, complex genotype-phenotype correlations have been described in VHL disease, and as a result, VHL disease has been divided into types 1 and 2 according to clinical presentation [6-8]. Type 1 VHL disease is characterized by susceptibility to hemangioblastomas and RCC, but rarely PPGL. However, PPGL is more common in patients with Type 2 disease.

With the exception of hemangioblastomas and endolymphatic sac tumors, tumors typically found in VHL disease can occur as sporadic, or non-familial, events. Thus, a clinical diagnosis of VHL disease in a patient without a positive family history requires the presence of at least three tumors. Approximately 20% of VHL disease patients result from a *de novo* mutation and do not have a family history [9]. The characterization of the *VHL* tumor suppressor gene as in the cause of VHL disease has facilitated not only the early diagnosis of VHL disease, but also permits a diagnosis of VHL disease in individuals who do not yet satisfy the clinical diagnostic criteria [9], as is the case with Type 2C VHL patients who only manifest PCC.

1.2.1.1. VHL - genotype-phenotype associations

The *VHL* gene has three exons and encodes two VHL proteins. VHL has multiple functions and influences many cellular pathways [10]. Firstly, VHL has a critical role in regulating the proteolytic degradation of the α subunits of HIF transcription factor complexes. Here, VHL functions as an important part of the ubiquitin ligase protein to recognize and bind two hydroxylated proline residues of the HIF1/2α subunits and targets them for proteosomal degradation by ubiquitination. Under normoxic conditions where oxygen is abundant, the HIF1/2α subunits are rapidly degraded. Oxygen is a co-factor for the proline hydroxylases (PHDs; EGLNs) that modify the proline residues on the HIF1/2α subunits by hydroxylation. During hypoxia, oxygen is limiting and PHD proteins are unable to hydroxylate the HIF1/2α subunits. As a result, VHL cannot recognize and tag the α-subunits for degradation. Thus, the HIF1 and HIF2 complexes are stabilized and activate the hypoxic gene response, implicated in diverse processes, such as angiogenesis, proliferation, apoptosis, and metabolism [10].

As mentioned above, complex genotype-phenotype correlations have been observed in VHL (Table 1.2.). Kindred with retinal and CNS hemangioblastoma and CCRC, but not PPGL characterize type 1 VHL families. These families (Type 1) usually harbor truncating mutations, *VHL* gene

deletions, or missense mutations that disrupt the structural integrity of the VHL protein [6,8]. Recently, it has been proposed that Type 1 should be sub-classified. Type 1A disease is characterized by low risk to develop PPGLs and high risk of RCC and hemangioblastomas [11]. On the other hand, large VHL gene deletions with contiguous loss of C3orf10 (HSPC300) are associated with a significantly lower risk to develop RCC, in addition to low risk of PPGL, and has been called Type 1B [11,12]. The risk of hemangioblastoma is similar between Type 1A and 1B.

Families with PPGL are designated as Type 2 VHL disease and usually have germline surface missense mutations. Most of these families are further characterized as Type 2B, which manifest hemangioblastomas and RCC, in addition to pheochromocytoma [11]. Type 2A families manifest pheochromocytoma and hemangioblastoma, but have a lower risk of RCC [11]. Finally, families where pheochromocytoma is the only feature are designated as Type 2C [13,14]. Type 2C families are usually affected by specific *VHL* missense mutations [15]. This classification has proven helpful in research correlating VHL function with specific mutations, but has been less helpful in the clinical management.

Table 1.2. Sub-types of VHL disease

Subtype	Clinical manifestations	Mutation type	Mutation effect
Type 1 A	- Low risk of PPGL - Retinal and CNS HB - High risk of RCC	- Gross deletions - Truncating mutations - Missense mutations affecting hydrophobic core	- Complete loss of pVHL function - Disrupt the tertiary structure of pVHL
Type 1 B	- Low risk of PPGL - Retinal and CNS HB - Lower risk of RCC	- Large contiguous deletions of VHL and HSPC300 genes	- Complete loss of pVHL function - Loss of HSPC300 modifies RCC risk
Type 2 A	- High risk of PPGL - Retinal and CNS HB - Lower risk of RCC	- Missense mutations affecting surface residues	- Mutations associated with HIF deregulation
Type 2 B	- High risk of PPGL - Retinal and CNS HB - High risk of RCC		
Type 2 C	- Only PPGL	- Specific missense mutations	- Mutations result in some ability to regulate HIF

CNS: central nervous system; HB: hemangioblastoma; RCC: renal cell carcinoma; pVHL: VHL protein

Interestingly, missense mutations associated with Type 2 VHL disease occur at surface residues and presumably allow for some retention of function, whereas mutations associated with Type 1 disease, such as gross deletions, truncating mutations, and missense mutations affecting codons within the hydrophobic core, disrupt the tertiary structure of pVHL [16]. Although mutations associated with Type 2A and 2B are associated with HIF deregulation, Type 2C mutations did not show impaired ability to regulate HIF, implicating HIF-independent mechanisms in the pathogenesis of pheochromocytoma in VHL disease [15,17]. Lee et al. reported that Type 2 VHL

disease associated mutations tested impaired the apoptotic pathway leading to the hypothesis that specific *VHL* mutations promoted pheochromocytoma development by allowing sympathetic neuronal progenitors to escape from developmental apoptosis [18].

1.2.2. Multiple endocrine neoplasia type 2

Multiple endocrine neoplasia type 2 (MEN2) syndrome is caused by activating mutations in the *RET* (rearranged during transfection) proto-oncogene [19] and has an incidence of 2.3 per 100,000 people per year. Located on 10q11.2, the *RET* gene encodes for a transmembrane tyrosine kinase receptor for members of the glial cell line-derived neurotropic factor (GDNF) family [20]. Mutations in *RET* usually affect in the extracellular cysteine-rich region or the intracellular tyrosine kinase domain coded by exons 10-11 or exons 13-16, respectively [21]. Oncogenic activation of RET activates various signaling pathways, including PI3K/AKT, MAPK, JNK, and RAS/ERK pathways [22].

MEN2 is divided into MEN2A and MEN2B. MEN2A accounts for approximately 90% cases of MEN2 syndrome, and is characterized by a combination of medullary thyroid carcinoma in all patients, hyperparathyroidism resulting from parathyroid hyperplasia or adenoma in 10-20% of patients, and pheochromocytoma in 50% of patients. Patients with MEN2B present about the same frequencies of medullary thyroid carcinoma and pheochromocytoma as in MEN2A, but also include additional clinical manifestations, such as ganglioneuromatosis of the gastrointestinal tract, mucosal neuromas, and a marfanoid habitus. However, MEN2B patients have little to no risk to develop parathyroid adenoma. Although most often associated with mutations in codon 634, pheochromocytomas are found in patients with *RET* mutations in almost all MEN2-associated codons [23]. Interestingly, about 6-9% of patients with MEN2A are thought to have a *de novo* germline mutation in the *RET* gene, while 50% of MEN2B patients harbor a *de novo* germline mutation.

1.2.3. Neurofibromatosis Type 1

Neurofibromatosis type 1 is a relatively common autosomal dominant disorder associated with mutations in the NF1 gene (neurofibromin 1) and has a prevalence of approximately 1 in 3,500 [24]. NF1 is caused by inactivating mutations in the *NF1* gene, located on chromosome 17q11.2. The *NF1* gene encodes a protein, called neurofibromin, which belongs to the family of GTPase-activating proteins. Neurofibromin is mainly expressed in the in the nervous system, where it attenuates the activity of the RAS/RAF/MAPK signaling pathway by inactivating RAS [25]. Also as a result, neurofibromin inhibits the PI3K/AKT/mTOR pathway [26].

Neurofibromatosis type 1 patients usually present multiple café-au-lait maculae, neurofibromatosis, iris hamartomas, and axillary or inguinal freckling [24]. Because the *NF1* gene is one of the largest known genes, with 60 exons, genetic testing is not usually offered and diagnosis of NF1 is often made on the basis of clinical criteria. The incidence of PCC in patients with NF1 syndrome is between 1 and 5% [27]. Until recently it was thought that *NF1*-related PCC were associated with germline mutations in the gene, however new data indicates that 21% to 23% of patients with sporadic PCC harbor inactivating mutations in the NF1 gene [28-30].

1.2.4. Paraganglioma-Pheochromocytoma syndromes

The paraganglioma-pheochromocytoma syndromes (PGL1-PGL5) are autosomal dominant syndromes with frequently incomplete penetrance that is caused by germline mutations in genes coding the subunits (*SDHB*, *SDHC*, *SDHD*, and *SDHAF2*) of succinate dehydrogenase (SDH) complex, also known as the mitochondrial complex II. Complex II, tethered to the mitochondrial inner membrane, is a Krebs cycle enzyme that couples the oxidation of succinate to fumarate with the reduction of ubiquinone to ubiquinol to generate electrons for oxidative phosphorylation through the electron transport chain (Figure 1.3.).

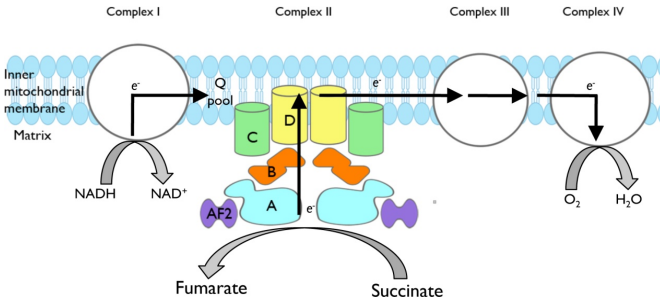

Figure 1.3. The electron transport chain. Succinate dehydrogenase enzymatic complex (Complex II) channels electrons from the catalytic dehydrogenation of succinate to fumarate. (A) SDH subunit A (SDHA). (B) SDH subunit B (SDHB). (C) SDH subunit C (SDHC). (D) SDH subunit D. (AF2) SDH subunit AF2 (SDHAF2).

The subunit A (SDHA) is the enzymatically active part of SDH complex, where oxidation of succinate to fumarate occurs, generating and liberating electrons. These electrons are passed along to subunit B (SDHB), which receives and transfers these electrons to the remaining components of the SDH complex. Anchoring SDHB and SDHA subunits to the inner mitochondrial membrane, SDH subunits C (SDHC) and D (SDHD) accept electrons liberated by succinate oxidation and passes them further along the electron transport chain. Initially, only mutations in subunits B (*SDHB*), C

(*SDHC*), and D (*SDHD*) were thought to be associated with PPGL [31]. However, recently mutations in subunit A (SDHA) of Complex II and succinate dehydrogenase complex assembly factor 2 (SDHAF2) genes were described in PPGLs. A database containing all mutation in the *SDH*-related genes (*SDHx*) mentioned above is publically available at http://chromium.liacs.nl/lovd_sdh/home.php. Deficiency of the SDH complex by mutations in the *SDHx* genes result in accumulation of succinate that profoundly deregulates metabolic homeostasis through, in addition to other mechanisms, inhibition of 2-oxoglutarate (2-OG)-dependent enzymes (approximately 65 enzymes) (more detail provided below: results and discussion sections).

1.2.4.1. PGL1 - Succinate dehydrogenase, subunit D

In 2000, Baysal and colleges identified the succinate dehydrogenase, subunit D (*SDHD*) gene, located on chromosome 11q23.1, as the gene responsible for PGL1 syndrome [32]. The *SDHD* gene is maternally imprinted. Thus the disease is predominantly paternally transmitted, meaning only children that inherit an SDHD mutation from the father have high risk for developing tumors. However, this is not always true, as several cases have described maternal transmission of an SDHD mutation [33-35]. *SDHD* mutation carriers generally develop parasympathetic paragangliomas, accounting for 89% of cases [36]. Although less frequent, approximately 29% of *SDHD* patients develop pheochromocytoma and sympathetic paraganglioma [36,37]. *SDHD*-related tumors are generally benign with approximately 8% of cases presenting metastasis [38].

1.2.4.2. PGL2 - Succinate dehydrogenase complex assembly factor 2

The causative gene in PGL2 syndrome was identified as *SDHAF2* (succinate dehydrogenase complex assembly factor 2), which encodes for a protein (167 amino acids) necessary for flavanation of the SDHA protein in complex II and is essential for the enzyme activity. Like the *SDHD*, the *SDHAF2* gene is imprinted and evidence indicates that it follows a paternal mode of transmission. In 2009, SDHAF2 is located on chromosome 11q12.2 [39]. The first *SDHAF2* mutation (c.232G>A; p.Gly78Arg) was identified in a Dutch family presenting parasympathetic paragangliomas. Later, the same mutation was also identified in a Spanish family with a similar clinical presentation (e.g. early onset with multiple parasympathetic paragangliomas) [40]. Although there have been few additional reports of SDHFA2 mutations in these tumors and its prevalence appears rather low, it has been widely accepted that SDHAF2 screening should be performed in young patients with multiple head and neck paragangliomas [40-42].

1.2.4.3. PGL3 - Succinate dehydrogenase, subunit C

Not long after the discovery of *SDHD* gene, succinate dehydrogenase, subunit C (*SDHC*) was identified as the causative gene in PGL3 syndrome [43]. Located on chromosome 1q13, the *SDHC* gene codes for a 15 kDa integral membrane protein. *SDHC* mutation carriers almost always present parasympathetic PGL, although PCC and sympathetic PGL have also been reported. Most

SDHC-related tumors reported to date have a benign behavior with some exceptions, and *SDHC* mutations show a low penetrance [44,45].

1.2.4.4. PGL4 - Succinate dehydrogenase, subunit B

In 2001, mutations in the succinate dehydrogenase, subunit B gene (*SDHB)* were identified the gene responsible for PGL4 syndrome [46]. *SDHB* mutation carriers mainly present sympathetic PGL and PCC, although parasympathetic PGL have also been described. *SDHB*-related tumors have a high risk of malignancy, with up to 43% of patients presenting metastasis [36,38,47]. *SDHB* mutations are almost exclusively occur in the germline, although some cases presenting somatic *SDHB* mutations have been described [48]. Although SDHB has a low penetrance of above 30% at 80 years of age, paradoxically it is highly prevalent in pediatric patients, makes its study mandatory in patients under the age of eighteen [49,50]

1.2.4.5. PGL5 - Succinate dehydrogenase, subunit A

Located on chromosome 5p15, the *SDHA* (succinate dehydrogenase, subunit A) gene codes for the catalytic subunit of mitochondrial complex II. *SDHA*, a tumor suppressor gene, was initially thought to only be associated with Leigh syndrome, a progressive neurodegenerative disorder [51], caused by homozygous *SDHA* germline mutations. Interestingly, PCC or PGL have not been reported in the parents of patients with Leigh syndrome, who are expected to have a heterozygous *SDHA* mutation. In 2010, Burnichon at al. described one patient with an *SDHA* mutation presenting a sympathetic PGL [52]. Since, several other *SDHA* mutations have been identified in PPGLs. As these variants are also present in control populations, it is sometimes difficult to assess their pathogenicity. However, in these cases, SDHA IHC often useful to resolve these cases [53,54].

1.2.5. Transmembrane protein 127

The first reported involvement of the *TMEM127* (transmembrane protein 127) gene in PCC was in 2010 [55]. Located on chromosome 2q11.2, *TMEM127* appears to act as a tumor suppressor gene, and is thought to regulate MTORC1, which is downstream of RET and the PI3K/AKT signaling pathways [55,56]. The incidence of *TMEM127* mutations in PCC is approximately 2% [57], but this percentage rises to 23% when only cases with familial history and to 31% for multiple tumors. The age of onset for TMEM127 patients is about 42.8 years, which is higher than that of other PPGL genes. As a result, many *TMEM127* mutations go undetected and thus, classified as sporadic incidents. Although rare, *TMEM127* mutations have been described in PGL [58]

1.2.6. MYC associated factor X

The association between PPGL and mutations in the *MAX* (MYC associated factor X) gene was reported by our group in 2011 [59]. Using transcriptomic profiling, we indentified three tumors with very similar expression signatures from unrelated patients presenting a familial history of disease.

Exome sequencing of germline DNA from these three patients identified mutations in *MAX*. Absence of MAX protein in tumors, as well as loss of heterozygosity caused by paternal [60,61] uniparental disomy of chromosome 14 was observed in these patients. Soon after, the multi-institution study by Burnichon et al. it was established that germline *MAX* mutations account for about 1% of pheochromocytomas [62]. Similarly to *TMEM127*, the contribution of the *MAX* gene becomes more relevant when considering those patients with family history of the disease bilateral or multiple pheochromocytomas (11% and 63%, respectively) [62].

1.2.7. Endothelial PAS domain protein 1

EPAS1 (Endothelial PAS domain protein 1), also known as HIF2α, is one of the two main hypoxia inducible factors (HIF) that not only senses cellular oxygen levels, but also mediates many cellular responses to hypoxia. Recently, mutations in the *EPAS1* gene were described in two patients with sporadic congenital polycythemia who subsequently developed multiple paragangliomas [63]. Later somatic *EPAS1* mutations were identified in sporadic pheochromocytomas and paragangliomas in the absence of erythrocytosis [64]. Mutations in the *EPAS1* gene affect the proline, which is hydroxylated by PHD enzymes, or nearby residues that impairs interaction with E3 ligase resulting in gain-of-function to delay proteosomal degradation [63-65].

1.2.8. Fumarate Hydratase

Inactivating mutations in another gene involved in the Krebs cycle, fumarate hydratase (*FH*), were recently been described in PPGL. After performing DNA methylation profiling in a large series of PPGLs, Letouzé et al. found a single hypermethylated tumor, clustered with *SDHx* specimens. This non-*SDHx* tumor was deep sequenced revealing mutations in the *FH* gene [66]. Although rare, more PPGLs harboring *FH* mutations have been identified in French and Spanish populations through a collaborative effort in which this Lab participated, where I (Aguirre A. de Cubas) was among the first authors [67]. Unlike the SDH complex that participates in both the Krebs cycle and oxidative phosphorylation (electron transport chain), fumarate hydratase is only involved in the Krebs cycle. Fumarate hydratase catalyzes the hydration of fumarate to generate malate, which usually continues along the Krebs cycle, where malate dehydrogenase couples its oxidation to oxaloacetate with the reduction of NAD+ to NADH. Similar to SDH deficiency, Inactivation of FH results in accumulation of fumarate, which like succinate competitively inhibit 2-OG-dependent enzymes. Thus, mutations in *FH* presumably cause PPGL through a mechanism synonymous to that of PGL1-5 syndromes.

1.2.9. Harvey rat sarcoma viral oncogene homolog

Activating mutations in the RAS (*rat sarcoma*) oncogenes, *KRAS*, *HRAS* and *NRAS*, have been reported in 20-25% of tumors in general [68]. In 2013, Crona et al. identified somatic mutations in the *HRAS* (Harvey rat sarcoma viral oncogene homolog) gene in PPGL by exome sequencing. As RAS proteins are upstream of the MAPK/ERK signaling pathway, it was not surprising to observe that these tumors cluster together with cluster 2 tumors (*RET*, *NF1*, *MAX*, and *TMEM127*)

(unpublished data). After this finding, an international collaboration allowed us to establish that the prevalence of *HRAS* mutations is 10% among adrenal PCC and was associated with benign disease [69].

1.2.10. Rare PPGL susceptibility genes

Also, mutations in other genes, such as *EGLN1* (egl nine homolog 1, also known as *PDH2*), *EGLN2* (egl nine homolog 2, also known as *PDH1*), *KIF1B* (kinesin family member 1B), and *MEN1* (multiple endocrine neoplasia 1, or menin 1), have been linked to the development of PPGL. It has long been known that mutations in the *MEN1* gene, located on chromosome 11q13, cause multiple endocrine neoplasia syndrome type 1 (MEN1). This syndrome is characterized by tumors of the pancreatic islets, anterior pituitary, and the parathyroid gland [70]. In 1997, the involvement of MEN1 mutations in PPGL development was first documented. Currently, it is believed that PCC is observed in less than 1% of *MEN1* germline mutation carriers [71]. A germline mutation in *EGLN1* was described in a patient with a PGL and congenital erythrocytosis [72]. Later, germline mutations in were also found in *EGLN2* [73]. Germ-line mutations in *KIF1B* were initially found in three members of a large family presenting PCC, and like EGLN1/2 were considered almost isolated events in PPGL development restricted to specific families. Mutations in *KIF1B* were also described in neuroblastoma and medulloblastoma, other closely related neural crest tumors [74]. In addition, *KIF1B* is located on chromosome 1p36.2, which is a chromosomal region frequently deleted in these tumors and suspected to harbor a tumor suppressor gene. Both EGLN enzymes and KIF1B are involved in NGF-dependent neuronal apoptosis with KIF1B functioning downstream of EGLN3 (see below).

Although initially their contribution to PPGL development was considered almost trivial, additional germ-line *EGLN1*, *EGLN2*, and *KIF1B* mutations have been recently reported and their importance will probably continue to increase as additional deep-sequencing studies are carried out [73,75,76] [77]. In fact, recent evidences indicate that the contribution of *KIF1B* mutations in PPGL may be equally as important as those in *MAX* and *TMEM127* [77].

1.3. Common mechanism of tumorigenesis in PPGLs

It has long been proposed that mutations in the known susceptibility genes converge on a common mechanism that impairs EGLN(PHD)/C-JUN/JUNB developmental apoptosis [18]. During embryogenesis, most sympathetic precursor cells undergo C-JUN-dependent apoptosis as they compete for growth factors, such as nerve growth factor (NGF) [78,79]. According to this model proposed by Lee et al., all of the known PPGL susceptibility genes affect this common pathway that regulates NGF withdraw-induced apoptosis of sympathetic neuronal precursors during development (Figure 1.4).

Briefly, loss of NGF stimulation leads to attenuation of JUNB and activation of C-JUN, and induction of EGLN3 and subsequently KIF1B, and the induction of apoptosis [18,74]. As mentioned earlier, mutations in the *VHL* gene result in HIF deregulation. However, Type 2C *VHL* mutations

appear to be normal with respect to HIF regulation [15,17], suggesting HIF-independent mechanisms are at work in *VHL*-related PPGLs. All *VHL* mutants linked to PPGL, including Type 2C mutations, fail to down-regulate JUNB, the C-JUN antagonist, which promotes survival after NGF withdraw. Transcription of *JUNB* is regulated by atypical protein kinase C (aPKC) family members, and as it turns out, VHL regulates aPKC, as well as HIF [18,80,81].

Thus, *VHL* mutations appear to contribute to PPGL pathogenesis by interfering with *JUNB* regulation, which permits escape from NGF-dependent apoptosis. Similarly, PPLG-linked mutations in *RET* and *NF1* are known to enhance NGF signaling and to promote sympathoadrenal precursor cell survival after NGF withdrawal [82,83]. Inactivating *SDHx* and *FH* mutations have been shown to promote the accumulation of succinate and fumarate, respectively, which competitively inhibits the activity of members of the 2-oxoglutarate (2-OG)-dependent dioxygenases, such as EglN3, and promote survival when NGF becomes limiting [18,66]. Figure 1.4. shows where these genes intervene along the EGLN3/C-JUN/JUNB apoptotic pathway.

1.4. Diagnosis

Because a large part of PPGLs produce and secrete excessive amounts of catecholamines, biochemical studies have become a powerful tool for more precise PPGL diagnosis. Over the years, different substances measured in urine and blood have been used to diagnose PPGLs, such as dopamine, 3-methoxytyramine, norepinephrine, and epinephrine, and their metabolites, normetanephrine and metanephrine [84]. Tumors that predominantly or exclusively produce dopamine are rare. Recent findings have shown that different levels of biochemical entities according to the various hereditary mutations which are known to cause PPGLs. PPGL patients with *RET*, *NF1*, and *TMEM127* mutations have been found to have an adrenergic phenotype, meaning that tumors mainly produce epinephrine. *VHL*-, *SDHB*-, *SDHD*-, and *EPAS1*-related PPGLs, on the other hand, have a noradrenergic phenotype, which is associated predominantly with norepinephrine production, rarely showing increased epinephrine levels. In addition to frequently exhibiting a noradrenergic phenotype, *SDHB*-related PPGLs, as well as *SDHD* mutants, are also often dopaminergic [85,86]. In 173 patients with proven familial disease, Eisenhofer and colleges reported that the combined measurement of epinephrine, norepinephrine, and dopamine in urine and plasma has a high predictive value to distinguish those with *RET* mutations from those with *VHL* and *SDHx* [86]. During this thesis project, a collaborative effort leaded by our group allowed identified an intermediate biochemical profile associated with *MAX* mutant tumors, characterized by high levels of norepinephrine with normal or mild elevation of epinephrine's [62]. Subsequently, another initiative undertaken by Dr. Graeme Eisenhofer, Nan Qin, and the author (AA de Cubas) elucidated the mechanism behind the unexpected neurochemical phenotype in MAX tumors where there was intermediate PNMT expression, but no PNMT enzymatic activity [87]. EPAS1 was identified and validated as the guilty culprit, as EPAS1 expression in itself completely blocked steroid-induced expression of the catalytically active isoform of *PNMT* [87]. This subject is revisited in the Discussion section 5.4.3, where our DNA methylation study contributes further insight into these processes in PPGLs.

Usually, imaging studies follow biochemical diagnosis, as the precise location of the PPGLs is important to determine the most suitable therapeutic approach. Although anatomical location can be determined using commonly used imaging modalities, such as CT and MRI, PPGLs can be visualized quite well using newer techniques such as [$^{123/131}$I]-metaiodobenzylguanidine (MIBG) scintigraphy, 6-[^{18}F]fluoro-L-3,4-dihydroxyphenyl-alanine (DOPA) positron emission tomography (PET), 6-[18F]fluorodopamine (FDA) PET, 2-[18F]fluoro-2-deoxy-D-glucose (FDG) PET, somatostatin analogs, diffusion-weighted MRI (DWI-MRI), and the combination of PET/CT. The established functional imaging modality to detect PPGLs is [$^{123/131}$I]-MIBG scintigraphy. This type of scan shows reasonable sensitivity, especially for benign tumors, and also has the advantage of automatically indicating whether [$^{123/131}$I]-MIBG treatment is possible [88]. However, poor uptake in extra-adrenal tumors and suboptimal or false-negative results in metastatic PPGLs remains problematic [88-90].

1.5. Challenges in disease management

The prevalence of malignancy in PPGLs has been reported to be between 2% and 24% [91,92]. Metastases of chromaffin cell tumors are commonly found in the lymph nodes, bone, liver, and lung. Whereas the patients without metastasis exhibit 5-year overall survival of about 89.3%, the 5-year overall survival of patients with metastasis is approximately 50% [93,94]. Furthermore, it has been reported that in patients initially diagnosed with benign disease, the main decrease in survival was due to diagnosis of metastatic disease [95]. Therefore, it is of paramount importance to identify molecular predictors of malignant potential for these tumors so that physicians can take appropriate measures, such as increased surveillance of the patient (biochemical analyses, imaging, ect.), before the development of metastatic disease.

Some studies have focused on parameters such as age, post-operative symptoms and tumor location, and pathological features, such as tumor type, size, weight, and microscopic features to predict malignancy in PPGL. It has been generally accepted that extra-adrenal PPGLs exhibit a higher risk of malignancy, but there is no correlation with right, left, or bilateral presentations [96,97]. Tumor size has often been shown to predict malignancy when comparing average size of benign and malignant tumors [96-98]. Persistent post-operative hypertension has also been associated with risk of malignancy, as it may represent occult metastasis [97]. At present, the presence of extra-adrenal disease, the tumor size, and the presence of post-operative hypertension seem to be the only clinical factors, which help predict the risk of malignancy in PPGL. However, while the presence of multiple clinical factors is a good indication for a more close surveillance, by themselves these factors are insufficient to actually diagnose or predict malignancy.

Although many types of cancer exhibit discriminative histological features, this is not the case for PPGLs. In determining malignancy, a wide variety of microscopic, histological, and immunohistochemical features have been assessed and incorporated into three multi-factorial scoring scales: 1) Linnoila et al. for PPGLs [99], 2) the pheochromocytoma of the adrenal gland

scaled score (PASS) for sympathetic paragangliomas [100], and 3) a scaling score by Kimura et al. for PPGLs [101]. These scaling scores provide a reasonable indication of malignancy, but do not possess enough certainty to provide confirmation.

1.6. PPGL in the age of molecular genomics

A better understanding of the genetic complexity and high molecular diversity of PPGL, as well as virtually any pathology, may lead to more efficient diagnosis and management of the disease. In this regard, the molecular mechanisms through which mutations in the above genes contribute to the pathogenesis and clinical behavior of PPGL are not completely clear. Fortunately, high throughput genomic technologies (OMICs) have provided new tools to study the molecular mechanisms behind PPGL, as well as an efficient means for biomarker discovery. In these regards, several high throughput mRNA expression profiling studies have been conducted in PPGL, including one study publish by our group [102-105].

Although it has been proposed that mutations in the known PPGL susceptibility genes all converge on a common mechanism, which deregulates the EGLN(PHD)/C-JUN/JUNB developmental apoptotic pathway to promote tumorigenesis, transcriptomic studies revealed the existence of two distinct transcriptional programs underlying PPGL development [18,106]. In one group, called cluster 1, were clustered PPGLs with mutations in *VHL*, *SDHB*, *SDHC*, and *SDHD* genes. The gene expression signature of cluster 1 tumors displayed enrichment in functions related to pseudohypoxia and angiogenesis. This profile is consistent with the biological role of the respective PPGL susceptibility genes in the HIF pathway. Over-expression of both HIF1 and HIF2 target genes has been reported in the VHL/SDHx cluster (cluster 1). Further analysis demonstrated a preferential expression of HIF1 target genes, such as glycolytic genes, in *VHL*-related tumors, while *SDHx*-related PPGLs displayed enhanced expression of HIF2 target genes, which has been proposed among one of the many hypotheses explaining the increased malignant potential of SDHB tumors relative to their cluster 1 counterparts [102].

The second group of tumors (cluster 2) contained the most of the remaining genetically undefined tumors, as well as *RET*-, *NF1*- *TMEM127*-, and *MAX*-related tumors. Pathway analysis showed activation of the kinase receptor signaling, protein synthesis, and genes involved in neural/neuroendocrine identity [104,107]. *RET* mutations have been associated with increased activation of phosphatidylinositol 3 kinase (PI3K)/v-akt murine thymoma viral oncogene homolog 1 (AKT) signaling, while loss of NF1 function resulted in unregulated RAS activation. *TMEM127*-related PPGLs displayed enrichment in lysosomal and endocytic functions and mTOR MTORC signaling [55]. Mutations in the *MAX* gene deregulate the MYC transcriptional network to contribute to PPGL development [59,87].

Although mRNA expression profiling has furthered our knowledge of PPGL molecular biology, there still remains unanswered questions regarding other levels of transcriptional regulation, such as microRNAs and DNA methylation patterns. In addition, chromosomal alterations have not yet been studied in detail in PPGL. Therefore, the application of microRNA and DNA methylation

profiling and SNP-arrays to study PPGL is necessary to answer these questions, as well as to identify novel molecular markers.

1.6.1. MicroRNA expression profiling

MicroRNAs (miRNAs) are small non-coding RNAs, which negatively regulate gene expression at the post-transcriptional level. The first miRNAs to be discovered were the lin-4 and let-7 RNAs, which were identified on the basis of their roles in controlling developmental transitions in Caenorhabditis elegans (C. elegans) [108,109]. Over the past decades, the list of reported miRNA functions has grown rapidly to include the control of cellular proliferation, apoptosis, and migration. Many miRNAs are differentially expressed differentially during development and differentiation, suggesting that each cell type might have a unique miRNA signature. Currently, it is thought that miRNAs are capable of post-transcriptional regulating the expression of an estimated one-third of all metazoan protein-coding genes [110].

MiRNAs are transcribed by polymerase II in the nucleus as long transcripts or a cluster of miRNAs, (called pri-miRNAs), which are capped and poly-adenylated like other protein coding genes [111,112]. After which an enzyme, called Drosha, individually cleaves the pri-miRNA to yield a stem loop containing pre-miRNAs, which have a length of 60-70 nucleotides. Cytoplasmic transport of pre-miRNAs is mediated by exportin 5 [113]. Then the cytoplasmic ribonuclease type III enzyme (DICER1) cleaves the pre-miRNA to form double stranded miRNA molecules with a length of 21 to 25 nucleotides [114]. The resulting double stranded miRNA loaded into the RNA induced gene silencing complex (RISC), where one strand will remain associated with the enzyme to serve as a template to direct target recognition, while the other strand is cleaved and discarded [115].

MicroRNAs have been compared to a molecular rheostat that fine tunes gene expression. To specify repression, miRNAs bind to semi-complementary sites at the 3'-UTR of targeted mRNA, which can result in mRNA degradation, translational truncation, or both [60,61]. It is believed that miRNA complementarily to target mRNA is directed by a short sequence of 6 nucleotides usually in positions 2 to 7 of the miRNA (called the seed region) [116]. Although rare, interactions with regions other than the 3' UTR of the mRNA have been reported [117]. Currently several prediction algorithms are available to predict miRNA targets, some of which include TargetScan [118], MiRanda [119], and miRWalk [120]. Similarly to many other bioinformatics or *in silico* predictors, there is a high rate of false positives associated with miRNA target prediction algorithms and the results should be analyzed with caution and usually require in vitro validation. Several studies have shown that gene expression responds to the presence of a miRNA by decreasing gene expression [110]. Therefore, miRNAs can affect gene expression [116].

At the beginning of this thesis project, there was no data about miRNA expression in PPGL. During the course of this thesis, some miRNA expression profiling studies have been published in PPGL [121-123]. However, miRNAs have not been fully characterized by these studies.

1.6.2. Chromosomal alterations

Chromosomal alterations, such as insertions and deletions of chromosome fragments, are key events in tumor cells [124,125]. Chromosomal alterations in cancer can be characterized by array-comparative genomic hybridization (arrayCGH), SNP-arrays, and more recently by whole-genome sequencing. Several arrayCGH studies have been performed in PPGL to examine chromosomal alterations [126-133]. Loss of chromosome 1p is the most common chromosomal aberration in sporadic and familial PPGL [126,127]. Interestingly, loss of chromosome 1p, which contains the *SDHB* and *KIF1B* genes, has also been frequently reported in other tumors, including neuroblastoma, and has long been suspected of housing one or more tumor suppressor genes (TSG) [74]. Generally, *RET*-related PPGLs show loss of chromosome 1p and 3q [128]. *VHL* mutated PPGLs also often show loss of chromosome 3p. In *SDHD*-related PPGLs, generally present loss of chromosome 11p [34], while frequently losses of 1p and 17q are found in *NF1*-related PPGL [29,134]. Loss of chromosome 3q, 11p, and 17q described in *VHL*-, *SDHD*-, and *NF1*-related PPGLs, respectively, is not surprising given that loss of this chromosomal region results in loss of the respective wild-type allele.

Solid tumors, like PPGLs, are composed of multiple populations of both normal and tumoral cells, and in addition, tumor cells often deviate from a diploid state, which makes assembly and interpretation of arrayCGH data difficult [129,130,135-140]. As a result, most studies have been limited to reporting gains and losses, and are unable to correctly assess allele-specific copy numbers to all loci in the reference genome. Fortunately, use of SNP array technology and application of bioinformatics algorithms, such as ASCAT (allele-specific copy number analysis), to analyze data permits us to take into account both aneuploidy of the tumor cells and non-aberrant cell infiltration when reporting chromosomal alterations. The ASCAT algorithm reports aberrant cell fraction in the tumor, ploidy, chromosomal gains and losses, loss of heterozygosity (LOH), and copy-neutral events (chromosomal disomies).

1.6.3. DNA methylation profiling

Epigenetics is the study of mechanisms other than direct changes in the DNA sequence that regulate and influence gene expression, whose involvement has been firmly established in somatic reprogramming. Epigenetic information can be dynamic and transitory, or relatively stable, capable of being passed on through cellular divisions. The most thoroughly understood and studies epigenetic mechanism is DNA methylation, which has been proven to be associated with a number of key physiological processes, such as genomic imprinting, X-chromosome inactivation, the regulation of gene expression and the maintenance of chromosome integrity through chromatic structural modulation, DNA stabilization and conformational control [141]. DNA methylation refers to the chemical modification of cytosine residues by addition of a methyl group at the 5 position of the pyrimidine ring, forming a 5-methylcytosine (5mC). Methylation of cytosine residues typically occurs in the context of CpG dinucleotides (a cytosine followed by a guanosine in the 5'→3' direction).

The global distribution of CpG methylation is known as the DNA "methylome", and in mammals, the bulk of CpGs in the methylome are in the methylated state (5mC) [142,143]. This high level of genomic methylation is interrupted by short stretches of unmethylated DNA, many of which correspond to regions of high CpG content known as CpG islands (CGIs). Although the majority of CGIs are in the unmethylated state, research shows that a subset of CGIs are found methylated in a tissue specific manner [142,143]. DNA methylation patterns are variable between different tissue types and are dynamic during cell differentiation. This property together with heritability of CpG methylation patterns and the ability to modify transcription, implicates DNA methylation as a process influencing maintenance of cell identity.

With respect to DNA methylation-mediated gene regulation, the most studied regions are those directly proximal to transcription start site. It is generally accepted that if a promoter element contains sufficient density of CpG dinucleotides, the presence of high levels of DNA methylation is strongly associated with repression of gene transcription, whereas the unmethylated state is associated with either transcriptionally actively genes, or in other cases, inactive genes subject to other forms of repression. Examples of this type of repression of gene expression by DNA methylation include X-chromosome inactivation and imprinting, and appear to contribute to mainly long-term repression. In vertebrates, DNA methylation can also occur within a gene body and has been suggested to represent a crucial function in the gene regulation of co-transcriptional RNA processing, such as alternative splicing. This raises the possibility that tissue-specific differences in DNA methylation within gene bodies could contribute directly to differential RNA processing. A second potential function of intragenic DNA methylation is to prevent erroneous transcription with in gene bodies.

Surprisingly, approximately 50% of CGIs are not associated with the 5' end or gene body of annotated genes, but are instead found in intergenic regions, referred to as "orphan" CGIs. Interestingly, orphan CGIs are more often found in the methylated state than promoter-associated CGIs and they also show a greater degree of tissue specific methylation, which suggests that these orphan CGIs may have more diagnostic specificity and sensitivity than conventional CGIs [144,145]. Although the function of orphan CGIs and their methylation state is currently unclear, it has been suggested that many orphan CGIs represent promoters for unannotated transcripts or functional non-coding RNAs [146]. DNA methylation has also been reported in the regions flanking CGIs and gene promoters, called CpG shores [147]. It has been reported that the greatest variation in DNA methylation between cell types occurs at CGI shores [148]. CpG shores are defined as regions immediately flanking a CGI, within 2 kb on either side, and thus, may have a lower CpG content relative to the neighboring CGI [147]. The exact functional consequence of CpG shore methylation is unclear, but it seems to correlate with reduced transcription of the neighboring gene [147,149]. Thus, the rules for DNA methylation are not exactly black or white, and therefore extreme caution should be exercised when interpreting DNA methylation data.

2. OBJECTIVES

OBJECTIVES

- To fully characterize miRNA expression in PPGL according to genetic background. Integrate miRNA expression with matched mRNA expression data to identify potential miRNA-mRNA interactions and estimate functional consequence of deregulated miRNA expression in PPGL.

- Evaluate whether miRNA-mediated regulation of gene expression occurs through transcript degradation or through translational truncation. Also, assess the correlation between miRNA, mRNA, and protein expression.

- To characterize chromosomal alterations in PPGL with different genetic background to evaluate potential association between the two.

- To explore DNA methylation patterns in the various genetic entities of these tumors, and to identify CpGs associated with PPGL malignancy.

- Assess potential associations between DNA methylation and progression-free survival in these tumors.

3. MATERIAL & METHODS

3.1. Samples

All samples were collected in collaboration with several Spanish and international Hospitals, and with the help of the Spanish National Tumor Bank Network (CNIO, Madrid, Spain), as well as with the help of the European Network for the Study of Adrenal Tumors (ENS@T). Written informed consent to collect phenotypic and genotypic data was obtained from all participants in accordance with institution review board (IRB) - approved protocols for each center.

Hematoxylin and eosin staining from all samples were evaluated by two pathologists and selected only those contained at least 80% tumor cells. The material derived from normal adrenal gland available was obtained from multi-organ donations and selected by pathologists. All frozen and FFPE tissues were previously genetically characterized and classified accordingly [59,64,102].

Initially, the presence or absence of PPGL was determined by physical examination and biochemical diagnosis, and usually confirmed by appropriate anatomical and functional imaging necessary for confirmation and localization of the tumor, as well as metastases. Patients with metastatic disease were those who presented metastasis in sites normally devoid of chromaffin tissue (e.g. lung, liver, bone, lymphnodes), maybe present at first diagnosis (synchronous) or occur a number of years, in some cases up to 20 years, after primary surgery. If no metastasis were detected at last follow-up, the tumor was considered benign.

3.1.2. Samples for microRNA expression

For the miRNA expression profiling study, we hybridized a total of 75 fresh frozen samples, 69 PPGLs and 6 normal adrenal medullas (nAM). These 69 PPGLs contained germline mutations in the following genes: *VHL* (n=13), *SDHB* (n=9), *SDHD* (n=4), RET (n=14), *NF1* (n=4), *TMEM127* (n=3), and *MAX* (n=3). The series also included 14 WT PPGLs, defined as tumors with no mutations in the known susceptibility genes. Of 63 tumors, only five were malignant (SDHB_4, SDHB_5, MAX_1, MAX_2, and Sporadic_14).

Table 3.1.1. Clinical summary of samples in miRNA expression study

	miRNA Expression			miRNA Validation		
	***N*[1]**	**Ben[2]**	**Mal[3]**	***N*[1]**	**Ben[2]**	**Mal[3]**
VHL	12	12	-	6	6	-
RET	14	14	-	8	8	-
NF1	4	4	-	-	-	-
SDHA	-	-	-	-	-	-
SDHB	9	7	2	6	1	5
SDHC	-	-	-	-	-	-
SDHD	4	4	-	7	6	1
FH	-	-	-	-	-	-
EPAS1	-	-	-	-	-	-
MAX	3	1	2	-	-	-
HRAS	-	-	-	-	-	-
TMEM127	3	3	-	-	-	-
WT	14	13	1	-	-	-
N1 PPGL	63	58	5	27	21	6
nAM[4]	6			2		

1) *N* Total samples. 2) Benign tumors. 3) Malignant tumors.
4) nAM; Normal adrenal medulla.

The six nAMs used here were obtained as described above. Owing to limited availability of material, an independent collection of 27 PPGL FFPE samples was used for validation, with germline mutations in the following genes: *VHL* (n=6), *SDHB* (n=6), *SDHD* (n=7), *RET* (n=8), and two nAM tissues. All *SDHD*-associated PPGLs used for this study were parasympathetic tumors with head and neck locations. The clinical features and the genetic characteristics of frozen and FFPE samples are summarized in Table 3.1.1., more details provided in Supplementary Table 3.1.1.

3.1.3. Samples for SNP-array genotyping

In total, 90 fresh frozen PPGLs were submitted for high-density SNP-array genotyping to analyzed chromosomal alterations. Summarized in Table 3.1.2., this series of tumors contained 15 VHL-, 9 *SDHB*-, 3 *SDHD*-, 16 *RET*-, 8 *NF1*-, 1 *TMEM127*-, 3 *MAX*-, 4 *EPAS1*-, and 1 *HRAS*-associated tumors, as well as 30 WT PPGLs. Of these 85 tumors, nine were malignant PPGLs.

Table 3.1.1. Clinical summary SNP-array samples

	Chromosomal		
	N[1]	Ben[2]	Mal[3]
VHL	15	16	-
RET	16	16	-
NF1	8	8	-
SDHA	-	-	-
SDHB	9	7	2
SDHC	-	-	-
SDHD	3	3	-
FH	-	-	-
EPAS1	4	4	-
MAX	3	1	2
HRAS	1	1	-
TMEM12	1	1	-
WT	30	25	5
N1 PPGL	90	81	9
nAM[4]	6		

1) *N* Total samples. 2) Benign tumors. 3) Malignant tumors. 4) nAM; Normal adrenal medulla.

3.1.4. DNA methylation samples

The Discovery Series (DS) of tumors was composed of 123 fresh frozen PPGL specimens collected through the European Network for the Study of Adrenal Tumors (ENS@T). This series included 99 benign and 24 malignant tumors. DS did not contain any head and neck (parasympathetic) PGLs, only PCC and sympathetic PGLs were included. These 99 benign tumors contained 22 *VHL*-, 26 *RET*-, 8 *NF1*-, 4 *SDHB*-, 2 *SDHD*-, 4 *EPAS1*-, 2 *MAX*-, 2 *HRAS*-, and 1 *TMEM127*-related PPGLs. The remaining 28 benign PPGLs had no mutations in the known susceptibility genes and were denoted as "wild-type" (WT). The 24 malignant tumors were mostly WT (n=17) with the rest being 4 *SDHB*-, 2 *MAX*-, and 1 *VHL*-related PPGLs.

DNA methylation data for another large validation series, denominated Validation Series 1 or VS1, of PPGLs was obtained from a publicly available database, Gene Expression Omnibus (GEO, www.ncbi.nlm.nih.gov/gds), from the study of Letouzé et al., under the accession number GSE39198 [66]. This previously described series originally contained 14 malignant PPGL and 130 benign tumors. VS1 was extended with ten additional malignant specimens, provided by Letouzé et al. that had not been previously published. Like the DS, VS1 contained only pheochromocytomas and sympathetic PGLs. The 24 malignant tumors in VS1 included 10 *SDHB*-, 5 *VHL*-, 2 *NF1*-, and 1 *FH*-related PPGLs, as well as 6 WT tumors. As previously described, all VS1

samples were obtained through the COMETE network, had ethical approval from the institutional review board, and patients provided written informed consent [66].

Table 3.1.3. Clinical summary for methylation study tumors

	Discovery Series			Validation Series 1 VS1)			Validation Series 2		
	N[1]	Ben[2]	Mal[3]	*N*[1]	Ben[2]	Mal[3]	*N*[1]	Ben[2]	Mal[3]
VHL	23	22	1	24	19	5	3	2	1
RET	26	26	-	13	13	-	-	-	-
NF1	8	8	-	30	28	2	-	-	-
SDHA	-	-	-	1	1	-	1	-	1
SDHB	8	4	4	16	6	10	3	3	-
SDHC	-	-	-	1	1	-	-	-	-
SDHD	2	2	-	3	3	-	-	-	-
FH	-	-	-	1	-	1	-	-	-
EPAS1	4	4	-	-	-	-	-	-	-
MAX	3	2	2	4	4	-	-	-	-
HRAS	2	2	-	-	-	-	2	1	1
TMEM127	1	1	-	1	1	-	-	-	-
WT	45	28	17	60	54	6	24	8	16
N[1] PPGL	123	99	24	154	130	24	33	14	19
nAM[4]	-			3			-		

1) *N* Total samples. 2) Benign tumors. 3) Malignant tumors. 4) nAM; Normal adrenal medulla.

For further validation, we compiled an additional independent series of FFPE PPGLs (n=33), called Validation series 2 or VS2. Of these thirty-three FFPE PPGLs, more than half were malignant (n=19). The malignant tumors included 16 WT, 1 *SDHA*-, 1 *HRAS*, and 1 *VHL*-related PPGL. The benign tumors were composed of 3 *SDHB*-, 2 *VHL*-, 1 *HRAS*-associated PPGLs, and 8 WT cases. Tumors were obtained through ENS@T, from the Spanish National Cancer Research Centre (CNIO) and Erasmus Medical Center in Rotterdam, NL. VS2 was composed of only pheochromocytomas and sympathetic PGLs, and contained no head and neck (parasympathetic) PGLs. Table 3.1.3. provides a summary of clinical features for DS, VS1, and VS2 PPGLs, while more detailed information about these series can be found in Supplementary Table 3.2.

3.2. Biomolecules

Various types of biomolecules, including DNA, mRNA, miRNA, and protein, were necessary for the experiments performed in this thesis project. DNA was used for sequencing, SNP-array genotyping, and DNA methylation assays. Both miRNA and mRNA were used for RT-qPCRs and hybridization experiments, while protein was required for proteomic studies.

3.2.1. DNA extraction & purification

Total DNA was extracted and purified using the DNeasy Blood and Tissue Kit (Qiagen, Chatsworth, CA, USA) according to the manufacture's protocol. For DNA methylation profiling, as well as pyrosequencing reactions, the concentration of DNA was measured using PicoGreen reagent (Invitrogen). For other uses, DNA concentration was measured using a NanoDrop

spectrophotometer (NanoDrop Technologies, Wilmington, DE, USA). The procedure employed is provided below.

3.2.1.1. DNA from frozen tissue

Briefly, approximately 20 mg of frozen tissue was digested with Proteinase K at 55°C for 2-4 hours. Then digested DNA was bound to DNeasy Mini spin column, washed, and dried. The purified DNA was eluted 75-150 µL of Elution Buffer. The eluted DNA can be stored at 4°C, or at -20°C for long-term storage.

3.2.1.2. DNA from FFPE tissue

Four to six sections (10um) were obtained from each paraffin block and placed in a 1.5 mL microcentrifuge tube. The tissue was deparaffinized by three additions of 1 ml Xylol. The xylol was removed from tissue pellet by three 100% EtOH washes, and the tissue pellet was dried at room temperature for 10 minutes with the tube un-capped. The pellet was digested with Proteinase K at 55°C for 2-4 hours or until completely digested. The digested sample was incubated at 80°C for 15 minutes to de-crosslink DNA. Once the pellet has been deparaffinized, digested, and DNA de-cross-linked, the remaining protocol for DNA extraction and purification was performed as described in section 3.2.1.1.

3.2.1.3. DNA quantification by PicoGreen

Standard solution preparation was prepared by dilution to 200 ng/µL. DNA standard and DNA samples were dispensed in a black fluorometric 96-well plate. Then 2 µL of DNA sample was dispensed alongside the standard. In the first well (A1) of a black 96-well plate for fluorometric detection, stock Lambda DNA standard was diluted to 200 ng/µl in a final volume of 233.3 µl 1 X TE buffer. Then 66.7 µL of 1X TE buffer was dispensed in the second well (B1), and 100 µL 1X TE buffer was added to the next six wells (C1, D1, E1, F1, G1, and H1). A serial dilution of the DNA standard was obtained by transferring 133.3 µL of diluted Lambda DNA from the first well (A1) to the second well (B1). Then 100 µL of diluted standard was transferred from the second well (B1) to the third well (C1). This was repeated for the next four wells (D1, E1, F1, and G1). No DNA was transferred to the last well (H1), which served as a blank. Finally, 2 µL of DNA sample (to be measured) was added in the subsequent wells.

A dilution containing 0.5 µL PicoGreen reagent in 100 µL of 1X TE buffer was prepared for each PicoGreen reaction. In each well, 100 µL PicoGreen dilution was added. The 96-well plate was covered with an aluminum adhesive cover, mixed thoroughly by vortex, and centrifuged. Fluorescence was measured with a Beckman Coulter® DTX800 Multimode Detector and intensities exported as a text document. A Standard curve was constructed using standard solutions, and used to calculate the concentration of DNA in the samples.

3.2.2. RNA Extraction

Total RNA from fresh-frozen specimens was extracted and purified using TRI Reagent® (Molecular Research Center, Cincinnati, OH, USA) and the mRNeasy Kit (Qiagen, Chatsworth, CA, USA). Extraction and purification of total RNA from FFPE tissue was performed using the RNeasy FFPE kit (Qiagen). Prior to use, the extracted and purified total RNA was treated with DNase to remove any DNA contamination. Finally, for hybridization experiments, RNA quality was measured with an Agilent 2100 Bioanalyzer (Agilent Technologies, Palo Alto, CA, USA). The procedures followed are provided below.

3.2.2.1. RNA from Frozen Tissue

Approximately 15 mg of frozen tissue was homogenized with a mechanical mortar and pestle. Once tissue has been fully homogenated, 1200 µL of TRI Reagent was added, the tube mixed by vortex, and incubated at room temperature for 5 minutes. Organic extraction of nucleic acids was accomplished by addition of 0.3-0.4 volumes of chloroform, the tube was shaken vigorously for 15 seconds (do not vortex!! Vortexing increases DNA contamination), and incubated at room temperature for 5 minutes. The tube was then centrifuged to separate organic and aqueous phases.

The aqueous phase, containing the RNA, was removed, and one volume of 70% ethanol was slowly added to the aqueous phase while gently mixing. The sample was passed through an RNeasy column. The flow-through was passed back through the column again. The flow-through was discarded and was in accordance to the manufacture's recommendations. The column centrifuged to dry the membrane before elution of RNA.

Then the purified total RNA was eluted in 40 µL of RNase-free dH2O. The eluted RNA was passed back through the column and eluted the RNA was then stored at -80°C.

3.2.2.2. RNA from FFPE tissue

Using a 2 mm biopsy needle, 2-4 cores were taken from each tumor (area of FFPE block was previously indicated by a pathologist). The cores mashed using a mechanical mortar and pestle. Once the cores have been mashed, the tissue was deparaffinized by three additions of Xylol. The xylol was removed from tissue pellet by three 100% EtOH washes, and the tissue pellet dried at room temperature. The dried deparaffinized tissue pellet was resuspended in Buffer PKD, Proteinase K was added, and the tissue was digested at 55°C for 15 minutes. The sample was incubated at 80°C for 15 minutes to de-crosslink the RNA. Then Buffer RBC and 100% ethanol was added to the sample, and the sample was passed through an RNeasy MiniElute spin column. The flow-through was passed back through the column. The column was washed in accordance to the manufacturer's instructions. The column was placed in a fresh collection tube and centrifuged at 13000 rpm for 5 minutes to dry the membrane. The purified total RNA was eluted in 20 µL of

RNase-free dH2O. To increase RNA yield, eluted RNA can be passed back through the column. RNA was then stored at -80°C.

3.2.2.3. DNase treatment of RNA sample

The concentration of the RNA was measured using a NanoDrop spectrophotometer. Then 10 µg of RNA sample was diluted in 50 µL to obtain a final concentration of nucleic acids at 200 ng/µL. To the diluted RNA sample, add 0.1 volumes of 10X DNase I Buffer (5 µL) and 1 µL of DNase I enzyme. The digestion was incubated at 37°C for 25 minutes. Then another 1 µL of DNase I enzyme was added to the RNA sample, briefly mixed, and incubated for 25 minutes at 37°C. The DNase I enzyme was inactivated by addition of 0.2 volumes of resuspended DNase inactivation Reagent, followed by 2 minutes of incubation at room temperature with occasional mixing. The inactivation reagent was pelleted by centrifugation at 10000 rpm for 1.5 minutes. Finally the supernatant containing purified RNA was transferred to a fresh 1.5 ml microcentrifuge tube. RNA was stored at -80°C until ready to use.

3.2.2.4. RNA concentration & quality

For uses other than hybridization, RNA concentration and purity were assessed by A260/A280 and A260/A230 ratios measured using a NanoDrop ND-1000 spectrophotometer (Thermo Scientific). RNA quality was considered acceptable when A260/A280≥1.8 and A260/A230≥1.5. For hybridization experiments, RNA quality was assessed using an Agilent 2100 Bioanalyzer (Agilent Technologies). Only samples with an RNA integrity number (RIN) greater than 7.5 were considered apt for hybridization experiments.

3.2.3. Protein extraction & purification

Four tumors (SDHB_3, SDHB_9, MAX_1, and MAX_3) were subjected to label free proteome analysis. Tissue specimen weights ranged from 10 mg to 22 mg. Samples were washed three times with cold PBS and homogenized with a Precellys 24 Bead Mill Homogenizer (Bertin Technologies, Villeurbanne, France) (20 x 2 s, power set to 5500 w), using three zirconium beads per tube. Then 15 µL of lysis buffer (50 mM HEPES, pH 7.5, 7M urea, 2M thiourea, 2% CHAPS, 100 mM DTT) with protease inhibitors and 0.1% benzonase were added per mg of tissue. Samples were then clarified by centrifugation (16000 g) at 4ºC for 15 min. Protein concentration was determined using the Protein Assay Kit (Bio-Rad, Hercules, CA) using BSA as standard (660nm Protein Assay, Pierce). Using the standard FASP protocol [150], 140 µg of protein was digested, and samples washed three to four times with UA (8M urea in 50 Mm ammonium bicarbonate). Subsequently, proteins were alkylated using iodoacetamide (50 mM) for 20 min in the dark and the excess of alkylation reagents was washed out with UA twice. Proteins were digested with endoproteinase Lys-C (Wako) during 6 hours at 37ºC (1:50 enzyme to substrate ratio). Finally, samples were diluted in 50 mM ammonium bicarbonate to adjust the urea concentration to 1M, and digested with Trypsin Gold (Promega) overnight at 37 °C. Resulting peptides were further desalted and concentrated

using homemade reversed phase micro-columns filled with Poros Oligo R3 beads (Life Technologies). The samples were dried in a Speed-Vac and dissolved in 80 µL formic acid (0.1%). The concentration of the peptides was measured by fluorescence at 348 nm after excitation at 284 nm.

3.3. MicroRNA expression

In this study, miRNAs were analyzed first by microarray hybridization. MicroRNA hybridizations were performed using the Agilent Human miRNA Microarray Kit version 2.0 (Agilent Technologies, Santa Clara, CA). For validation, expression of individual miRNAs was quantified by Quantitative real-time PCR (qRT-PCR) using miRCURY LNA Universal RT miR PCR system (Exiqon, Vedbaek, Denmark). Details about these experiments can be found below.

3.3.1. MicroRNA hybridization & processing

MicroRNA expression profiling was performed using the Agilent Human miRNA Microarray Kit version 2.0 (G4470B, one color technique, Agilent Technologies). For each tissue sample, 100 ng of total RNA were hybridized and processed in accordance with the manufacturer's instructions. The arrays were scanned with a G2565C DNA microarray scanner (Agilent Technologies), images were processed using the Agilent Feature Extraction (AFE) Software package version 10.1.1 (Agilent Technologies), and data were exported as text files.

3.3.4. Real-time quantitative PCR (RT-qPCR) for miRNAs

First-strand cDNA synthesis by RT of total RNA was performed using the miRCURY LNA Universal RT miR PCR system (Exiqon, Vedbaek, Denmark) according to the manufacturer's recommendations. All qRT-PCR assays were performed on an ABI PRISM 7900HT analyzer (Applied Biosystems) using the LNA miR-PCR primer/SYBR Green mix (Exiqon) in accordance with the manufacturer's recommendations. Reactions were per- formed in triplicate, and negative controls were included in all series of qRT-PCRs. The qRT-PCR data were imported into qBase[151], and after assessing the stability of five endogenous reference RNAs, we selected the most stable ones, 5S-rRNA, SNORD48, and SNORD66, for normalization. Relative miRNA expression was calculated using the $2^{-\Delta\Delta Ct}$ method. Statistical analyses were performed using StatPlus version 2009 (AnalystSoft, http://www.analystsoft.com/en/). Statistical differences between the four genetic classes of PPGLs (*SDHB*, *SDHD*, *VHL*, and *RET* mutants), as well as nAM, were assessed using Kruskal–Wallis one-way ANOVA (P>0.05).

3.4. Additional microarray expression data

Although no new mRNA hybridization experiments were performed in this study, we did utilize various publically available microarray expression data accessed through the Gene Expression Omnibus (http://www.ncbi.nlm.nih.gov/geo/). Details about additional microarray expression data utilized in this study are provided in sections 3.4.1, 3.4.2 and 3.4.3.

3.4.1. PPGL gene expression profiles

Gene expression profiling data for 99 PPGLs, containing 8 with and 91 without metastasis, was obtained through gene expression omnibus (GEO) under GSE19422 and GSE51087. As previously described, downloaded gene expression profiles were quantile normalized and antigenomic probes were used as background probes [87,102].

3.4.2. PC12 cell miRNA profiling data set

A miRNA microarray data set for PC12 cells was obtained from a publicly available database, Gene Expression Omnibus (GEO, www.ncbi.nlm.nih.gov/gds), from the study of Hamada et al. (2012), which included expression of 350 miRNAs after NGF stimulation at four time points (0, 12, 24, and 48 h) [152]. This dataset is available under the GEO accession number GSE32122.

3.4.3. *RDBP* knock-down in T47D breast cancer cells

Gene expression profiling data for T47D breast cancer cells with and without *RDBP* knockout was obtained through the gene expression omnibus (GEO accession number GSE19940). As previously described, downloaded gene expression profiles were quantile normalized and antigenomic probes were used as background probes [153].

3.5. Proteomic analyses

Four PPGL tumors (SDHB_3, SDHB_9, MAX_1, and MAX_3) were subjected to label-free proteome analysis. Samples were extracted and proteins were digested using a standard FASP protocol [154]. The resulting peptides were separated by online nano-LC and analyzed by electrospray MS/MS using a LTQ Orbitrap Velos mass spectrometer (Thermo Scientific, San Jose, CA, USA). The same protein amount was injected in triplicates. Raw files were searched against UniProtKB/Swiss-Prot human database (release date: April 18, 2012; 73579 sequences) using MaxQuant Software (v1.3.0.3; Martinsried, Germany) [155]. For protein assessment, at least two unique peptides with a FDR>0.01 were required. Label-free analysis was performed using the label-free quantitation (LFQ) values determined by MaxQuant [156]. Further analysis was done with Perseus Software (v1.3.0.3; Martinsried, Germany). A more detailed description of methodology is provided below.

3.5.1. LC-MS/MS analysis

Desalted peptides were diluted 1:10 and 0.5 µg of total protein was injected in the system. The peptides were separated by reversed-phase chromatography using a nanoLC Ultra system (Eksigent), directly coupled to an LTQ-Orbitrap Velos instrument (Thermo Fisher Scientific) via nanoelectrospray source (ProxeonBiosystem). Peptides were loaded onto the column (Dr. Maisch, Reprosil-Pur C18 GmbH 3 mm, 200x0.075 mm), with a previous trapping column step (IntegraFrit 100 µm x 25 mm containing ProteoPep II C18, 300 Å, 5 µm (New Objective)), during 10 min with a flow rate of 2.5 ml/min of buffer A (0.1% formic acid). Elution from the column was made with a 120 min linear gradient of 5-40% buffer B (acetonitrile, 0.1% formic acid). The peptides were directly electrosprayed into the mass spectrometer using a PicoTip emitter (360/20 OD/ID µm tip ID 10 µm New Objective) at 1.4 kV spray voltage with a heated capillary temperature of 275°C and S-Lens of 60%. Mass spectra were acquired in a data-dependent manner, with an automatic switch between MS and MS/MS scans using a top 20 method with a threshold signal of 1000 counts. MS spectra were acquired with a resolution of 60000 (FWHM) at 400 m/z in the Orbitrap, scanning a mass range between 350 and 1750 m/z. Peptide fragmentation was performed using collision induced dissociation (CID/CAD) and fragment ions were detected in the linear ion trap. The normalized collision energy was set to 35%, the Q value to 0.25 and the activation time to 10 ms. The maximum ion injection times for the survey scan and MS/MS scans were 500 ms and 150 ms, respectively, and the ion target values were set to 1E6 and 5000, respectively, for each scan mode.

3.6. High-density SNP-array genotyping

To investigate the presence of chromosomal rearrangements in the tumors, we performed high-density SNP-array analysis in 87 PPGLs. In accordance with the manufacturer's specifications, a genome-wide scan of over 700,000 markers was conducted on 250 ng of tumor DNA, using the Illumina HumanOmniExpress BeadChip (Illumina, San Diego, CA) at the Spanish, "Centro Nacional de Genotipado (CEGEN-ISCIII)" (www.cegen.org). Image data were analyzed using the Chromosome Viewer tool contained in GenomeStudio 2010.2 (Illumina) to obtain LOG R and BAF (B allele frequency) values. The metric used was the log-R ratio that is the binary logarithm of the ratio of the observed to the expected normalized log-R values for a given SNP [157]. The allele frequency was also estimated for all SNPs.

3.7. DNA Methylation

For the DNA methylation assay, bisulfite-conversion of DNA was performed using the EZ DNA Methylation Kit (Zymo Research, Orange, CA) following the manufacturer's recommendations. Genome-wide promoter DNA methylation profiling was performed using the Illumina Infinium

HumanMethylation 27K Platform (Illumina, San Diego, CA) at the Spanish, "Centro Nacional de Genotipado" (CEGEN-ISCIII; www.cegen.org) as previously described [158].

3.7.1. Bisulfite conversion of DNA

For each DNA sample, 5 µl of M-Dilution Buffer was added to the DNA and the total volume adjusted to 50 µl with water. The sample was gently mixed by flicking or pipetting up and down. For Illumina Infinium® Methylation Assay, 1000 ng of sample DNA was used, while 20 ug of sample DNA was necessary for pyrosequencing. The reaction was incubated at 37°C for 15 minutes. After the above incubation, 100 µl of the prepared CT Conversion Reagent was added to each sample.

For pyrosequencing, the reaction was incubated in the dark at 50°C for 16 hours. After, the sample was cooled on ice for 10 minutes. For the Illumina Infinium® Methylation Assay, the sample was incubated in a thermocycler at 95°C for 30 seconds, (50°C for 60 minutes) X16 cycles, and Held at 4ºC for at least 10 minutes.

Then 400 µl of M-Binding Buffer were added to a Zymo-Spin™ IC Column placed in a collection tube. The sample was then dispensed into the Zymo-Spin™ IC Column containing the M-Binding Buffer. The contents were mixed by inverting the column several times, centrifuged at full speed (>10,000 x g) for 30 seconds, and the flow-through discarded. After, 100 µL of M-Wash Buffer was added to the column. The column was centrifuged at full speed for 30 seconds before adding 200 µl of M-Desulphonation Buffer to the column. The reaction was incubated at room temperature (20-30°C) for 15-20 minutes, and after the incubation, the column was centrifuged at full speed for 30 seconds. The column was washed with 200 µl of M-Wash Buffer to the column, centrifuged at full speed for 30 seconds, an another 200 µL of M-Wash Buffer was added, and finally centrifuged for an additional 30 seconds. The column was placed into a 1.5 mL microcentrifuge tube, and converted DNA eluted in 10 µL of M-Elution Buffer. Converted DNA was stored at -20°C until used.

3.7.2. Methylation-specific PCR

Epigenetic detection of chromosome 14 uniparental disomy (copy neutral event) was performed with a methylation-specific PCR (MSP) for the *MEG3* promoter, as previously described [159]. Bisulfite treated genomic DNA was subjected to an MSP protocol in 25 µl reactions using approximately 5 ng of template, 3 mM $MgCl_2$, 0.2 mM dNTPs, 0.4 µM of each M primer (M.F: GTTAGTAATCGGGTTTGTCGGC; and M.R: AATCATAACTCCGAACACCCGCG) and/or 0.8 µM of each U primer (U.F: GAG GAT GGTTAGTTATTGGGGT; and U.R: CCACCATAACCAACACCCTATAATCACA) [160,161]. The following program was used for MSP: 94°C for 3 minutes followed by five cycles of 94°C for 30 seconds, 70°C for 30 seconds, 72°C for 30 seconds; 30 cycles of 94°C for 30 seconds, 60°C for 30 seconds, 72°C for 30 seconds; final 5 minute extension at 72°C. The products were separated and visualized on 3% high resolution agarose gel with ethidium bromide staining.

3.7.3. Illumina Infinium® Methylation Assay

After bi-sulfite conversion of genomic DNA, genome-wide DNA methylation profiling was performed at the Spanish "Centro Nacional de Genotipado (CEGEN-ISCIII)" (www.cegen.org) using the Illumina Infinium HumanMethylation 27K platform (Illumina, San Diego, CA) as previously described [158]. Briefly, after bi-sulfite conversion, first DNA samples were denatured, neutralized, and amplified overnight. The following day, the amplified DNA was enzymatically fragmented and precipitated using isopropyl alcohol. The DNA was resuspended, and DNA was hybridized on a BeadChip for 24 hours. After, the BeadChips were washed to remove unhybridized and non-specifically hybridized DNA before proceeding with single-base extension, where labeled nucleotides are incorporated in primers hybridized to the DNA. Finally, BeadChips were stained, coated for protection, and BeadChip Images obtained on an iScan™ Reader. The 27K platform generates DNA methylation data for 27,578 CpG dinucleotides corresponding to 14,473 unique genes.

Table 3.7. Bisulfite pyrosequencing primer sequences

Oligo Name	Sequence (5'->3')	Syn[a] Scale	Purification
Pyro-CYFIP2_cg00986320-F1	GGGTTGGAGAGTTTTATTTAAATTAGA	0.025	desalt
BIO-Pyro-CYFIP2_cg00986320-R1	[Btn]AACCCCTAAAACCAACAATAAT	0.5	HPLC
Pyro-CYFIP2_cg00986320-seq	AGTTGAATGAGATGATGA	0.025	desalt
BIO-Pyro-HDAC11_cg05446471-F1	[Btn]GTTAGTGGTGTTGGGTAATGGT	0.5	HPLC
Pyro-HDAC11_cg05446471-R1	AATTAATCACTTTACCCCATTTTCC	0.025	desalt
Pyro-HDAC11_cg05446471-R1	AATTAATCACTTTACCCCATTTTCC	0.025	desalt
Pyro-HDAC11_cg05446471-seq	CATACTAATACAACTAAATTATATA	0.5	HPLC
Pyro-RDBP_Cg06351503-F1	GGGTGTTTTTGGGTTTGTAG	0.025	desalt
BIO-Pyro-RDBP_Cg06351503-R1	[Btn]ATCCCCAACCTAACTACCT	0.5	HPLC
Pyro-RDBP_Cg06351503-seq	TTTTGGGTTTGTAGGT	0.025	desalt

a) Synthesis

3.7.4. Bisulfite pyrosequencing

Bisulfite modification of DNA was performed with the EZ DNA Methylation-Gold kit (Zymo Research) following the manufacturer's instructions. The set of primers for PCR amplification and sequencing were designed using the specific software PyroMark assay design (version 2.0.01.15). Primer sequences were designed to hybridize with CpG free sites to ensure methylation-independent amplification (Table 3.7). PCRs were performed with primers biotinylated to convert the PCR product to single-stranded DNA templates using the Vacuum Prep Tool. After PCR amplification, pyrosequencing reactions and methylation quantification were performed using PyroMark Q24 reagents, equipment and software according to manufacturer's instructions (Qiagen).

3.8. Cell culture

PC12 cells (provided by Marcos Malumbres, CNIO, Madrid, Spain) were cultured in a humidified 5% CO2 atmosphere at 378C in a complete medium, DMEM supplemented with 5% horse serum

(Sigma) and 10% bovine calf serum (Sigma). To assess differentiation, cells were grown in a differentiating medium, DMEM supplemented with 0.5% horse serum and 1% bovine calf serum.

For stimulation, PC12 cells were plated on poly-L-lysine coated 96-well plates (0.5x104 cells/well) in the complete medium for 24 h prior cotransfection and, after 12h, treated with the differentiating medium in the presence of low-dose NGF (10 ng/ml; Sigma). For negative (undifferentiated) and positive (differentiating) controls, we used PC12 cells transfected with miR-cel-67 in the absence and presence of NGF respectively.

3.8.1. miRNA mimics & transfections

Twenty-four hours after plating, cells were cotransfected with miRNA mimics (Exiqon) and p3GFP-1 using Lipofectamine 2000 transfection reagent according to the manufacturer's instructions (Life Technologies). The p3GFP-1 green fluorescent protein reporter was used to indicate positively transfected cells. Caenorhabditis elegans cel-miR-67 mimic does not target any gene in human and rat and was used for control transfections. The final concentration of miRNA mimic and p3GFP-1 used for cotransfections was 30 nM and 0.2 ng/ml respectively. Three independent experiments were performed and experimental conditions carried out in triplicate.

3.8.2. Quantitative analysis of cellular morphology & differentiation

PC12 cells (0.5!104 cells/well) were fixed with 4% formalin solution (Merck KLaA) for 10 min. Cells were washed with PBS and incubated with 0.2 mg/ml DAPI (Life Technologies) and CellMask:PBS (1:3; Life Technologies) for 40 min at room temperature and then washed with PBS. Images were captured in a laser scanning confocal TCS-SP2 (Leica Microsystems, Wetzlar, Germany) using LCS acquisition software (v2.61, Leica Microsystems) and magnification was 63X oil immersion objective with 1.4 NA.

Using the CellMask signal as the cell image, the DAPI signal as the nuclear image, and GFP signal as the neuronal cell image to discriminate transfected cells, cellular morphology was assessed by the Defeniens Developer XD Software (v2.0; Munich, Germany). Only GFP-positive PC12 cells were considered for subsequent analysis. Cellular morphology was quantified using three parameters: length (mm), border length (mm), and roundness (unitless values 0–N; more round (0)/less round (N)).

NGF-negative and -positive controls were used to define neuron-like differentiation using the above Defeniens parameters. The NGF-negative group represented cells with a less differentiated phenotype, more round with few projections, and lower values for cellular length, boarder length, and roundness. On the other hand, cells in the NGF-positive group displayed a neuronal-like differentiated phenotype, with neurite elongation and higher values for these parameters. This way we were able to assess the level of differentiation of cells in the miR-183- and/or miR-96-transfected groups.

3.9. Bioinformatics analyses

Numerous bioinformatics analyses were performed throughout this thesis. Earlier studies were performed basic tools with a user-friendly interface, but as my abilities increased during the execution of this thesis, I employ more complex bioinformatics techniques. In general, mRNA and miRNA expression data were handled in a similar fashion. First, expression data were normalized to produce an expression matrix, called an "Eset." DNA methylation data was also compiled and processed to obtain a similar matrix containing DNA methylation levels represented as "Beta (β)-values."

A general question faced by biologist and statisticians is how to organize the observed genomic data into meaningful structures. Unsupervised analyses have been widely explored for this purpose; that is to cluster biological objects sharing common characteristics into discrete groups. Such analyses allow us develop an integrated understanding of underlying biology. In general cluster methods can be divided in to two categories. The hierarchical methods produce nested clusters, while non-hierarchical methods, such as K-means clustering, divide a dataset of N objects into M clusters. For example, unsupervised hierarchical analysis of mRNA expression was previously shown capable of separating tumors according to genetic background [102], while K-means clustering can be used to verify cluster membership specified by hierarchical cluster analysis.

Supervised analysis generally follows unsupervised analyses to identify expression signatures or methylation patterns associated with some experimental group. For high-throughput data (miRNA, mRNA, and DNA methylation), supervised analyses were performed using linear models for microarray data, or *limma*. Due to the large number of comparisons being performed, the calculated p-values must be corrected for multiple testing. For example, we accept a p-value <0.05 as significant, which means that for any given observation, the result will occur by random chance in 5% of cases. Thus, if we perform a supervised analysis with 10,000 probes, then approximately 500 probes will be identified as significant when no real association exists. Thus, for these comparisons we use a calculated "false discover rate" (FDR) to assess significance (Benjamini & Hochberg method to correct for multiple testing).

In bioinformatics analyses, we frequently want to known the biological consequence corresponding to a given signature or experimental condition. Pathway analysis can be performed with a variety ways with numerous algorithms to infer biological meaning. These are extremely useful when we want to formulate a hypothesis for functional assays.

Other bioinformatics techniques were also employed during this thesis. These techniques range from integration to analysis of SNP-array data with the ASCAT algorithm, and are detailed below. Explanations of data interpretation are provided in their corresponding sections in Results and Discussion.

3.9.1. Analysis of mRNA and miRNA microarray data

The exported data files, obtained from feature extract software, were read into R using the Limma package, and the processed miRNA signal was obtained with the AgiMicroRNA package applying the RMA algorithm to obtain the normalized dataset [162,163]. MicroRNAs not expressed in more than 75% of the samples in each class were filtered. Data were further processed by filtering out flat patterns, and all subsequent analyses were performed using only miRNAs that passed both filters.

For data obtained from gene expression omnibus (GEO), the provided expression profiles were already normalized as submitted by the author. Although normalized data was provided, raw data files were also available to perform customized analyses.

3.9.1.1. Unsupervised analysis

For miRNA expression profiling studies, unsupervised hierarchical cluster analysis was performed with only miRNAs with significant expression (one-way ANOVA, false discovery rate (FDR) <0.002) in order to increase specificity. Unsupervised hierarchical cluster analysis was performed using GeneCluster 3.0 and viewed in a visualizer that displays cluster profiles and relevant cluster member information [164]. GeneCluster 3.0 permitted us to perform Bi-clustering, which simultaneously clusters both probes and arrays to group samples into clusters.

3.9.1.2. Supervised analysis and miRNA marker selection

Differential expression of miRNAs was computed vs. nAM samples independently for each experimental groups by non-permutation t-test analysis with limma Pomelo II web tool [165]. This way, we were able to identify the miRNA signature associated with PPGL experimental groups. As nAM was included as a calibrator, its effect cancels out when comparing between experimental groups. To facilitate the identification of specific miRNAs related to the genetic background, sporadic tumors were initially considered to identify miRNAs common among all PPGLs, but not taken into account thereafter, as they are genetically undefined. For each comparison (genetic group vs. nAM), only miRNAs with an FDR<0.05 and a fold change (log2) ≥±1.3 were considered significantly differentially expressed. By submitting these lists of miRNAs to Venn diagram analysis (VENNY, http://bioinfogp.cnb.csic.es/ tools/venny/index.html), we identified miRNAs specific to, as well as those common among all, genetic groups of PPGLs. In addition to the above criteria, we considered reported biological functions, when available, in the final selection of candidate miRNAs for validation.

3.9.1.3. Integration of mRNA and miRNA expression profiles

Using matched transcriptomic (mRNA) data available from the same tumors [102], integration with miRNA profiles was performed using the MiRNA And Genes Integrative Analysis (MAGIA) web tool, for each sample in a given experimental group [166]. First, this integration analysis was applied

to all PPGLs regardless of genetic background and nAMs and then to each genetic group, filtering those miRNAs common among all PPGLs (FDR <0.05). The log2-transformed mRNA data contained 19,620 genes. The miRNA target prediction algorithm TargetScan 5.0 (www. targetscan.com) was employed for all analyses.

MAGIA integration identified miRNA–mRNA gene pairs with a significant positive and negative correlation (FDR <0.25), and Ingenuity Pathway Analysis (IPA, Ingenuity Systems, Redwood City, CA, USA) was employed to assign biological functions to the putative target mRNAs. IPA output was ranked by statistical significance and focused on canonical pathway gene sets.

3.9.2. Proteomic data analysis

Proteomic analyses were performed on four tumors (SDHB_3, SDHB_9, MAX_1, and MAX_3), which were also included in the miRNA profiling study. First proteomic data were normalized, then a series of unsupervised and supervised analyses were performed. Finally, proteomic profiles were integrated with corresponding with mRNA and miRNA expression data.

After performing the corresponding proteomic assay described above, raw files were analyzed either by MaxQuant (version 1.3.0.3) (NCBI Human database, 73579 entries, 08/16/2011 release), oxidation of methionines was set as variable modification whereas carbamidomethylation of cysteines as fixed modification in the Andromeda search engine [155,167]. Minimal peptide length was set to 6 amino acids and a maximum of two missed-cleavages were allowed. For protein identification, at least two unique peptides with a FDR = 0.01 were required. When identified peptides could originate from two or more proteins (homologs or isoforms), MaxQuant reported these peptides as a protein group.

Each sample was run in triplicate. Label-free analysis was performed with MaxQuant using the LFQ values determined by the software [156]. Further analysis was done with Perseus software (version 1.3.0.3). The changes in protein abundance between the different samples were measured via a direct comparison of the LFQ intensities.

An unsupervised hierarchical clustering was used to assess the similarity of the different analyses. Moreover, significantly regulated proteins between the two tumor classes (i.e. *MAX* and *SDHB*) were assessed by ANOVA (significance threshold was set at p-value<0.05). Proteomic profiles were integrated with matched mRNA and miRNA expression data, and correlation was assessed by calculating the Pearson correlation coefficient, "r" for each interaction. Ranging from -1 to 1, positive Pearson correlation coefficient (zero to 1) indicates a positively correlated interaction with a value of 1 meaning perfect correlation. On the other hand, a negative coefficient value (-1 to zero) indicates a negatively correlated interaction, a coefficient value of -1 corresponds to a perfect negative correlation.

Protein classification (molecular function, biological process and protein class) was performed by PANTHER software, using the entire list of identified proteins as the reference data set.

3.9.3. SNP-Array Data

High-density SNP-array genotyping data can be used to analyze chromosomal alterations. Among the several methods available, we chose to use the ASCAT (allele-specific copy-number analysis of tumors) algorithm for several reasons. For instance, the ASCAT algorithm was an "R" based package (that I am familiar with), while other methods were executable in other informatic environments.

Illumina SNP arrays deliver two output tracks. 1) LOG R values provide a measure of total signal intensity, while 2) the BAF (B allele frequency) provides a measure of allelic contrast [168]. The LOG R track is similar to the output commonly given by array-CGH platforms and quantifies the total copy number of each genomic locus. The BAF track shows the relative presence of each of the two alternative nucleotides ("A" and "B") at each SNP locus profiled. The analysis of genotype profiles were complicated by two phenomena: infiltration of nonaberrant cells and aneuploidy of tumor cells. From LOG R and BAF tracks, ASCAT estimates the average ploidy and aberrant cell fraction for each sample. BAF and LOG R data were preprocessed by a specifically designed segmentation and filtering algorithm, called Allele-Specific Piecewise Constant Fitting (ASPCF), to reduce the effect of noise in input data. These ASPCF-smoothed data are subsequently used as input for the ASCAT algorithm to estimate the tumor ploidy and aberrant cell fraction, as well as the absolute allele-specific copy number.

Once ASCAT profiles had been generated for all samples, we searched for chromosomal alterations common to each genetic group of PPGL, and then these alterations were compared between groups to identify common, as well as group-specific chromosomal events.

3.9.4. Illumina Infinium® Methylation Assay data processing

The Genome Studio Methylation Module was used to assign methylation beta-values to each CpG site. The Beta-value is defined as the ratio between the methylated probe intensity and the overall intensity (sum of methylated and unmethylated probe intensities) [169]. Beta-values were quantile normalized using the "lumi" package [170].

For statistical purposes, Beta-values were converted to M-values using the Lumi package [170]. M-values are defined as log2 (methylated probe intensity/unmethylated probe intensity). Negative M-values indicate less than 50% methylation and positive M-values indicate more than 50% methylation [171]. M-value conversion corrects for the heteroskedasticity observed for beta-values, producing a homoskedastic distribution that is more appropriate for statistical analysis. Thus, M-values were used for statistical analysis, while beta-values were used for biological interpretation.

3.9.4.1. Unsupervised analyses

All unsupervised analyses were performed using "R". The top 500 probes with the highest variance across all samples we used for unsupervised analysis. Unsupervised analysis was carried

out using the "amap" package to calculate the Pearson's distance, and the "cluster" package for hierarchical clustering. The "ConsensusClusterPlus" package was used for consensus cluster analysis [172]. Dendrographs were represented as circular phylogenetic trees with a heatmap showing the top 10 CpGs using the "circlize" package [173].

3.9.4.2. Supervised analyses

All supervised analyses were performed using the "limma" package, and p-values were adjusted for multiple testing using the Benjamini & Hochberg method, or false discovery rate (FDR) [162]. We considered only those CpGs with FDR<0.10 and $\Delta\beta > |0.2|$ as significantly methylated, and were used in subsequent analysis. Supervised analyses were limited to experimental groups with at least three samples.

To identify DNA methylation patterns associated with the different PPGL genotypes, we performed a series of supervised analyses with *SDHB*, *VHL*, *EPAS1*, *RET*, *NF1*, and *MAX* mutant tumors. Comparisons between the different PPGL genetic groups were performed always relative to the *SDHB*-related experimental group so that inter experimental group comparisons could be readily performed.

3.9.4.3. Malignancy-associated CpGs

The following procedure was used to identify and validate malignancy-associated CpGs. First, candidate malignancy-associated CpGs were identified with DS. To distill our selection of malignancy associated CpGs, we assessed DNA methylation patterns of the above CpGs in VS1 tumors for replication. Using those successfully replicated CpGs, we further refined our selection by applying one final criteria: the epigenetic alteration must be present in at least 50% of the malignant PPGLs. *SDHB*-related PPGLs have a high risk of malignancy and have been previously shown to have a hypermethylator phenotype, previously defined by a signature of 298 hypermethylated CpGs [66]. Thus, we further filtered the data for these probes. Those CpGs meeting all the above criteria were considered as PPGL malignancy-associated CpGs.

3.9.4.4. Survival Analyses

To determine the potential impact of DNA methylation on progression-free survival (PFS), we performed a Cox regression at individual CpG data as continuous variables. PSF was defined as the time between initial diagnosis and appearance of metastasis or death by disease. As both DS and VS1 data was generated using the same platform, we pooled the two series to form a large series of 218 tumors with 36 malignant events to obtain a global perspective of these candidate prognostic markers, as well as increase our statistical potency. The final Cox Proportional-Hazards model was adjusted for *SDHB* mutation and series origin of tumors. In addition, p-values were corrected for multiple testing with the Benjamini & Hochberg method using all probes included in this study (n=26457). Kaplan-Meier curves and Cox regression analyses were generated using the "survival" package.

3.9.4.5. Other Bioinformatics methods for DNA methylation

Venn diagram analyses were performed with the "Vennerable" package (http://vennerable.sourceforge.net/), and circos plots were generated using the "circlize" package [173]. Pathway analysis was performed using the PantherDB classification system (http://www.pantherdb.org/) and DAVID Bioinformatics Resources 6.7 (http://david.abcc.ncifcrf.gov/home.jsp).

4. RESULTS

RESULTS

In continuation, results obtained during the course of this thesis, from November 2009 until August 2014. In total, four different studies have been performed, implementing various techniques, including miRNA, mRNA, SNP, and methylation profiling, among others, as described in Materials and Methods. In summary:

The first study focused on the microRNA expression profiling in PPGLs. The PPGL miRnome was extensively characterized to identify genotype specific miRNA signatures. Finally, miRNA expression profiles were validated by RT-qPCR in an independent series of PPGL.

In the second study biological consequences of deregulated miRNA expression in PPGL were explored through integration with matched mRNA expression data [102]. These analyses suggested potential implications in neuroendocrine-like differentiation. Functional studies performed in rat pheochromocytoma (PC12) cells showed miR-183 and/or miR-96 impeded NGF-induced differentiation. Proteomic studies suggested that miRNA-mediated regulation occurs at the transcriptional level.

The third study investigated chromosomal alterations in PPGL using high-density SNP genotyping to calculate the "ASCAT (allele-specific copy number analysis of tumors) profiles". Here, chromosomal alterations are described for recently described PPGL genetic groups, *EPAS1*, *MAX*, *TMEM127*, and *HRAS* mutants, as well as for *VHL*, *SDHD*, *SDHB*, *RET*, and *NF1* tumors.

The fourth and final study explored DNA methylation in a large discovery series (DS) of PPGLs, which was enriched with malignant tumors. We were able to identify DNA methylation patterns associated with PPGL malignancy. Using DNA methylation profiling data from an independent validation series (VS1) of PPGLs, we validated 52 malignancy associated CpGs. In another independent validation series (VS2) of FFPE samples, we validated hypermethylation of *RDBP* in malignant PPGLs by pyrosequencing. Finally, bioinformatics analyses were employed to explore possible biological consequences of confirmed malignancy-associated CpGs, as well as those produced by *RDBP* knockdown.

4.1. Part 1. MicroRNA expression profiling in PPGL

Although nearly three decades of comprehensive study of the clinical features associated with the known PPGLs genes has improved patient care and genetic counseling, we still don't completely understand the molecular mechanisms behind the development of these tumors. Thus, the application of high-throughput genomic technologies, such as transcriptomic profiling, is essential to further understand the underlying biology of these tumors. In fact, several mRNA expression profiling studies have established two main PPGL molecular subtypes: one is associated with a pseudohypoxic gene signature and the other with activated kinase signaling pathways. Although some clues about PPGL biology have been elucidated by these studies, a more complete picture of the gene expression regulation is required to better understand the mechanisms involved in PPGL development.

In 2009, small non-coding microRNAs (miRNAs) had not been fully characterized in PPGL. Therefore, the first objective of this thesis project was to characterize miRNA expression in these tumors, as well as identify genotype-specific miRNAs. Finally, we selected and validated eight miRNAs common among, as well as specific to PPGL genetic groups.

4.1.1. PPGL microRNA profiles

MicroRNA profiles were obtained for 63 PPGLs and 6 normal adrenal medullas (nAMs). After normalizing and preprocessing the profiling data, we obtained expression levels for 723 and 76 mature human and viral miRNAs, respectively. Viral miRNAs were omitted from subsequent analysis. A full listing of the miRNA microarray data has been deposited in the National Center for Biotechnology Information GEO database under the accession number GSE29742.

4.1.2. Unsupervised analysis

Unsupervised hierarchical cluster analysis revealed great homogeneity among cases sharing an alteration in the same gene (Figure 4.1.1). Two main clusters were identified, mainly defined by *VHL*/*SDHx*/nAM and *RET*/*NF1*/*TMEM127*/*MAX* specimen profiles, respectively. This cluster behavior resembles those previously described with mRNA expression profiles showing two main clusters: a "pseudohypoxic" branch containing *VHL*, *SDHB*, *SDHC*, and *SDHD* mutants and "cluster 2" characterized by *RET*-, *NF1*-, *TMEM127*-, and *MAX*-associated PPGLs. Of the 63 samples with known mutation, only two from the *RET*/*NF1*/*TMEM127*/*MAX*-related cluster were allocated to the *VHL*/*SDHx*/nAM branch.

Both adrenal and extra-adrenal tumors were represented in both clusters, whereas the head and neck tumors were grouped within the VHL/SDHx/nAM branch. With the exception of two tumors (SP_1 and SP_10: abdominal and carotid PGLs respectively), the remaining sporadic PPGLs (two abdominal and ten adrenal tumors) clustered within the *RET*/*NF1*/*TMEM127*/*MAX* branch.

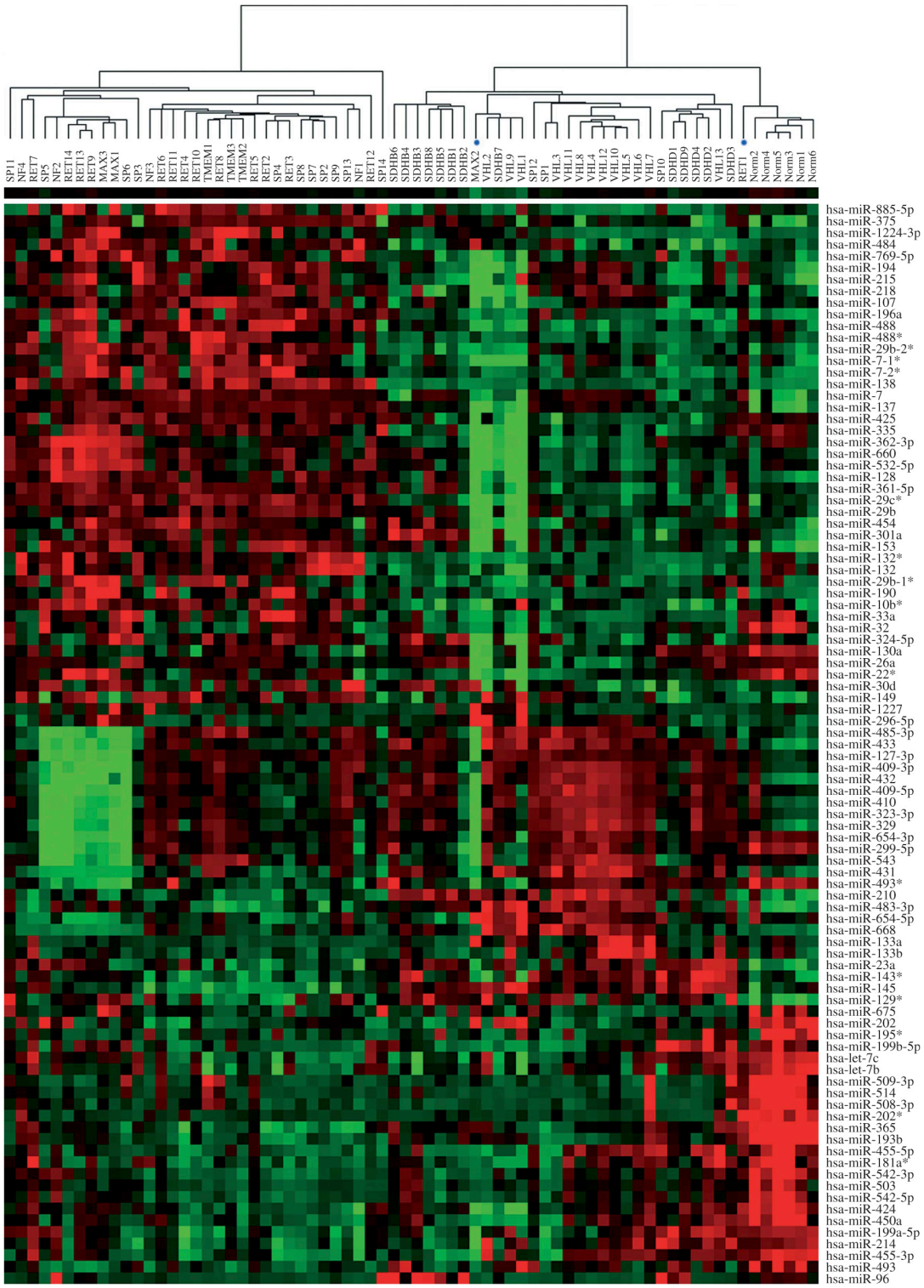

Figure 4.1.1. Unsupervised analysis of PPGL miRNA profiles. Hierarchical clustering of PPGL samples based on their miRNA expression profiles. Those 93 miRNAs with significant differences in expression (ANOVA; FDR<0.002) were subjected to unsupervised hierarchical cluster analysis. Both genes and samples were clustered by average linkage clustering method. Overexpression is shown in red, whereas under-expression is indicated in green. Blue dots indicate mis-clustered samples (MAX2 and RET1).

The nAMs, also included in the unsupervised hierarchical cluster analysis, clustered together and formed a separate subcluster, indicating that these samples have very similar miRNA signatures and that this signature was different from those of tumor samples. It is known that obtaining nAM without cortical contamination is extremely difficult. However, we used these nAMs available solely as a calibrator because they resemble normal adrenal tissue more than commercial RNA reference, and any effects related to possible cortical contamination would cancel out during comparisons between experimental groups.

4.1.3. Supervised analyses

Owing to the limited number of malignant tumors (n=5) in our series, we could not identify any differentially expressed miRNAs for the comparison between malignant and benign tumors (data not shown).

MiRNA expression was independently compared between PPGL experimental groups and nAM (FDR<0.05, n-fold>|1.3|). Supervised analysis results of the miRNA expression data comparing individual tumor classes to nAM are listed in Supplementary Table 4.1.1. (see attached CD). We found 51 miRNAs were significantly differentially expressed in *VHL*-related tumors, 54 in *SDHB*, 32 in *SDHD*, 50 in *RET*, 35 in *NF1*, 60 in *TMEM127*, 64 in *MAX*, and 49 in WT tumors compared with nAM. Five miRNAs (miR-193b, miR-424, miR-365, miR-493*, and miR-99a) were identified as commonly deregulated among all PPGLs (Figure 4.1.2, Supplementary Table 4.1.1.). Interestingly, miR-193b and miR-365 map the same chromosomal region at 16p13.12, which suggest that they are transcribed as a long polycistronic transcript.

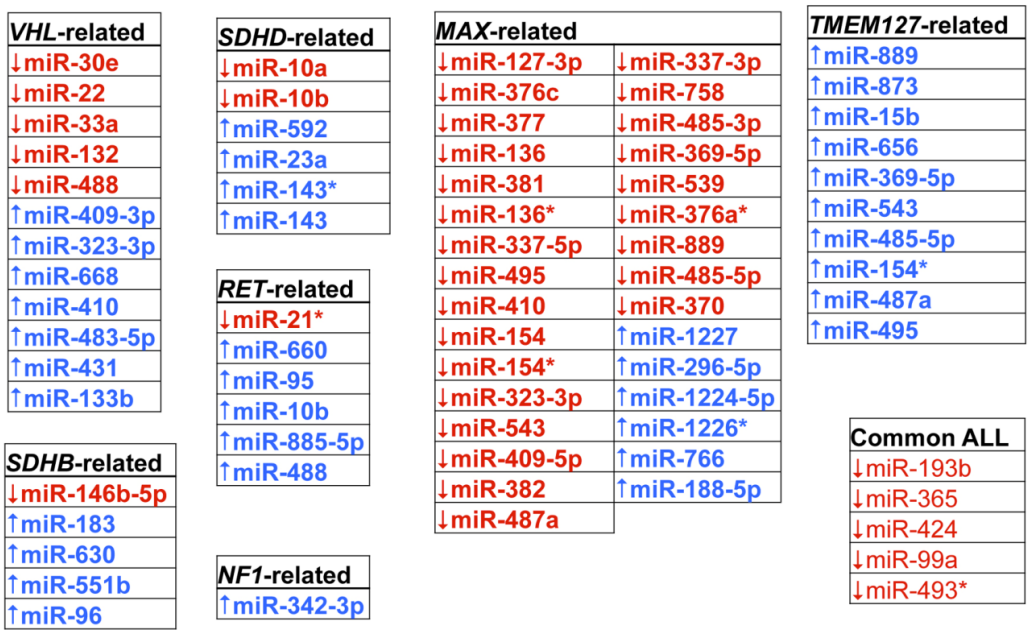

Figure 4.1.2. MicroRNAs specific to and common among PPGL genetic groups. Red arrows pointing downward indicate down-regulated miRNAs relative to nAM. Blue arrows pointing up indicate over-expressed miRNAs relative to nAM. All miRNAs shown had FDR<0.05

Besides identifying miRNAs commonly deregulated, we determined group-specific miRNA markers: 12 for *VHL*, 5 for *SDHB*, 6 for *SDHD*, 6 for *RET*, 1 for *NF1*, 10 for *TMEM127*, and 31 for *MAX* (Figure 4.1.2.). Some miRNAs were deregulated in certain genetic groups of PPGLs. *RET*-, *NF1*-, and *TMEM127*-associated, as well as sporadic, tumors over-expressed miR-138 and miR-7, while miR-137 and miR-382 were generally up-regulated in almost all PPGLs with variable expression between experimental groups. *VHL*- and *SDHB*-related tumors had specific up-regulation of miR-210 and miR-483-3p and down-regulation of miR-335.

Among these genotype-specific miRNAs, we found two clusters of miRNAs deregulated as a whole. For instance, a large number of significantly down-regulated *MAX*-specific miRNAs belong to the large miRNA cluster at chromosome 14q32.2 (DLK-MEG3 locus), while *SDHB*-specific miR-183 and miR-96 mapped to 7q32.2.

4.1.4. Validation of miRNA expression

Three miRNAs (miR-137, miR-382, and miR-210) common among some PPGL experimental groups and five group-specific miRNAs (miR-133b, miR-183, miR-488, miR-885-5p, and miR-96) were selected for validation. Upregulation of miR-137 was a common feature among experimental groups with the exception of *MAX*-related PPGLs. While significantly downregulated in *MAX*-related PPGLs, miR-382 was upregulated in nearly all tumors, but especially in *VHL*, *SDHB*, *SDHD*, and *RET* mutant tumors, and therefore selected for validation. Upregulation of miRNA-210 was unique to both *SDHB*- and *VHL*-related tumors and selected for validation to discriminate *SDHB* and *VHL* mutants from the other experimental groups. Upregulation of miR-133b was specific to the *VHL* mutant group, while upregulation of miR-488 and miR-885-5p was specific to *RET*-related tumors. miR-183 and miR-96 were selected for validation, as their robust upregulation was associated exclusively with *SDHB*-related tumors. All the above miRNAs were confirmed in an independent series (ANOVA, $P>0.05$; Figure 4.1.3, which allowed for further analysis and interpretation of miRNA profiling.

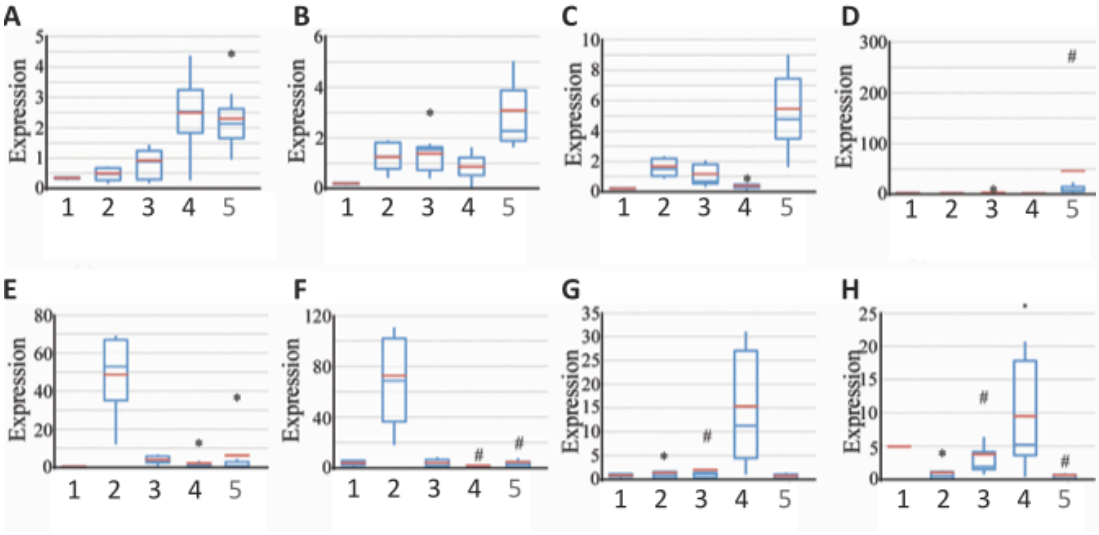

Figure 4.1.3. RT-qPCR validation of miRNA markers. RT-qPCR results for candidate miRNA markers. Samples arranged in following order: (1) normal adrenal medulla; (2) SDHB, (3) SDHD, (4) RET, and (5) VHL mutant tumors. A) hsa-miR-137 and B) hsa-miR-382 were generally overexpressed in PPGLs, except for in MAX tumors (not shown). C) hsa-miR-210 was up-regulated in VHL- and SDHB-associated tumors. D) hsa-miR-133b was specific to VHL mutants. E) hsa-miR-183 and F) hsa.miR-96 were uniquely up-regulated in SDHB-related PPGLs. G) hsa-miR-488 and H) hsa-miR-885-5p were overexpressed in RET tumors. All miRNA shown had $P<0.05$ (ANOVA). * indicates mild outlier. # indicates extreme outlier.

4.2. Part 2. Integration of miRNA-mRNA expression profiles

Once we characterized miRNA expression in PPGL and validated in general, as well as group-specific miRNAs, we sought to elucidate possible miRNA-regulated processes and pathways. To accomplish this, first, miRNA expression profiles were integrated with matched mRNA expression data, which were available from a previous study [102]. After identifying potential miRNA-mRNA interactions, we performed pathway analysis to determine biological consequences of deregulated miRNA expression in these tumors (Figure 4.2.1.). These bioinformatics analyses, suggesting deregulated miRNAs in PPGL were implicated in neuronal/neuroendocrine-like differentiation, proved extremely useful to formulate novel hypotheses. As it is widely accepted that PPGLs develop from immature sympathoadrenal precursors incapable of terminally differentiating into mature chromaffin cells, we turned our focused on miR-183 and miR-96, which we previously validated as specific to SDHB tumors [174]. We cultivated PC12 pheochromocytoma cells with and without miR-183 and/or miR-96 transfection, and using confocal microscopy, measured cellular morphology, specifically cell length, border length (perimeter), and roundness, to assess the extent of differentiation in the presence of NGF. Finally, we used label-free proteomic analysis to obtain protein expression data for a set of 4 tumors. Proteomic analyses permitted us to evaluate the validity of miRNA-mRNA integrative analyses. Proteomic analyses allowed us to explore the mode by which miRNAs exert their regulator effect, through translational truncation or mRNA transcript cleavage.

4.2.1. Integration of miRNA and mRNA expression profiles

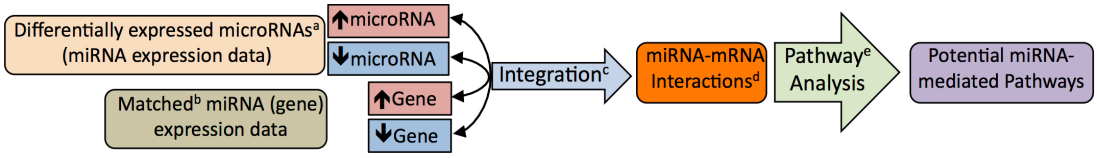

Figure 4.2.1. Integrative analysis workflow.

a) Differentially expressed miRNAs between two experimental conditions (FDR<0.05); Indentified upregulated and downregulated miRNAs. b) Matched mRNA (gene) expression profilies; Gene expression data for same samples as those used for miRNA study. c) Integration using MAGIA (miRNA and genes integrative analysis). d) Identified positively and negatively correlated miRNA-mRNA interactions with an associated coefficient and p-value (p<0.25 considered significant). e) Ingenuity Pathway Analysis identified potential miRNA-regulated pathways.

Potential negatively and positively correlated miRNA–mRNA interactions were predicted using the MAGIA (miRNAs and genes integrated analysis) bioinformatics tool [166]. The actual number of unique target genes was lower than the predicted miRNA–mRNA interactions as several genes can be targeted by multiple miRNAs, as shown in Table 4.2.1. The percentage of miRNA-regulated genes in these tumors ranged from 2.55% to 10.64% with a median of 7.2%.

Table 4.1.1. miRNA-mRNA interactions

Group	Total interactions[a]	Unique genes[b]	Total[c] (%)
VHL	2583	1710	8.72
SDHB	2193	1410	7.19
SDHD	749	638	3.25
RET	2942	1981	10.10
NF1	1749	1244	6.34
TMEM127	3412	2084	10.64
MAX	1160	682	3.48
14q32.2 miRs[d]	800	500	2.55
WT	2630	1607	8.19

a) Numbers of potential targets for the miRNAs with significant differences in expression for each experimental group of PCC/PGL relative to nAM. b) Unique annotated genes; each gene counted only once; Analyzed using Entrez Gene ID. c) Percent of genes potentially regulated by the microRNAs. Calculated using the total number of unique genes present on the Agilent Human 4x44k array (n=19,620). b) Clustered miRNA at chromosome 14q32.2 downregulated in MAX tumors.

4.2.2. Commonly deregulated miRNA in PPGLs

First, to address the functional significance of the commonly deregulated miRNAs (miR-193b, miR-365, miR-424, miR-99a, and miR-493*) in all PPGLs versus nAM (FDR<0.05), IPA enrichment analysis was performed with predicted gene targets. The significantly enriched potential miRNA-regulated pathways in all PPGL relative to nAM are listed in Supplementary Table 4.2.1. Several of these pathways were of particular interest, including "CREB signaling in neurons" and "breast cancer regulation by stathmin 1 (STMN1)". In both pathways, miR-365 was predicted to target phospholipase C beta 4 (*PLCB4*) and calcium/calmodulin-dependent protein kinase II gamma (*CAMK2G*), while miR-193b was predicted to target calmodulin 1 (*CALM1*) and phosphoinositide-3-kinase regulatory subunit 1 alpha (*PIK3R1*) was a predicted miR-424 target. Integration also predicted that miR-365 targets cAMP responsive element binding protein 5 (*CREB5*) in the "CREB signaling in neurons" pathway. In the "breast cancer regulation by stathmin 1" pathway, *STMN1* itself was a predicted target of miR-193, and miR-424 was predicted to target Cdc42 guanine nucleotide exchange factor 9 (*ARHGEF9*).

4.2.3. Potential miRNA-regulated pathways in PPGL genetic groups

To identify pathways potentially regulated by miRNAs in each genetic group of PPGL, the five commonly deregulated miRNAs between PPGLs and nAM were filtered out of the total set of 230 miRNAs. For each genetic group of PPGL, the remaining differentially expressed miRNAs were integrated with the corresponding mRNA expression data and IPA enrichment analysis was performed. Significantly enriched pathways for each PPGL experimental group relative to nAM are summarized in Supplementary Table 4.2.2. Since a large portion of the miRNA clustered at 14q32 were significantly down regulated in *MAX*-relate tumors with respect to not only nAM but also relative to the other PPGL genetic groups, integration and IPA enrichment analysis was performed to evaluate to possible contribution of these miRNAs (Supplementary Table 4.2.2.).

4.2.4. miRNAs in Pseudohypoxic (*VHL* and *SDHD*) tumors

Significant enrichment of the "reelin signaling in neurons" and "Gα12/13 signaling" pathways was among those identified unique to *VHL*-related PPGL. In the "Gα12/13 signaling" pathway, several cadherin (CDH) genes were predicted to be regulated by miRNAs, including *CDH2* by miR-124, *CDH6* by miR-26a, *CDH7* by miR-148a, and *CDH13* by miR-30e. The predicted miRNA-regulated genes in the "reelin signaling in neurons" pathway included *FYN*, *SRC*, *ITGA6*, *VLDLR*, and *MAPT*. Integration results indicate that miR-96 (down-regulated in *VHL*) targets *FYN* and *VLDLR*, while *SRC*, *MAPT*, and *ITGA6* are targets of miR-149, miR-132, and miR-32 and miR-30e, respectively.

In *SDHD*-related tumors, "citrate cycle" and "glyoxylate and dicarboxylate metabolism" pathways were found significantly enriched. This was particularly interesting, as *SDHx* mutations, including *SDHD*, result in complex II deficiency that severely perturbs cellular metabolism. In both pathways, citrate synthase (*CS*) and aconitase 1 (*ACO1*) were predicted targets of miR-23a. In the "citrate cycle" pathway, pyruvate carboxylase (*PC*) could be targeted of miR-143, while in the "glyoxylate and dicarboxylate metabolism" pathway, miR-32 and miR-542-3 were predicted to target methylenetetrahydrofolate dehydrogenase 2 (*MTHFD2*).

4.2.5. miRNAs in "Cluster 2" PPGLs

Unique to *RET*-related PPGL was the "apoptosis signaling" and "focal adhesion kinase (FAK) signaling" pathways, among others. In the "FAK signaling" pathway, miR-139a and miR-542-3p were predicted to target talin 2 (*TLN2*), while miR-148a targeted Rho GTPase activating protein 26 (*ARHGAP26*), and miR-7 targeted both v-crk sarcoma virus CT10 avian oncogene homolog (*CRK*) and epidermal growth factor receptor (*EGFR*). Integration results predict that miR-29a targets both tumor necrosis factor receptor superfamily member 1A (*TNFRSF1A*) and BCL2-antagonist/killer 1 (*BAK1*) in the "apoptosis signaling" pathway.

The "role of MAPK signaling in the pathogenesis of influenza pathway" was the only *NF1*-specific pathway identified where integration predicted peroxiredoxin 6 (*PRDX6*) was regulated by miR-138, miR-124 and miR-149, mitogen-activated protein kinase 11 (*MAPK11*) by let-7c, and protein kinase C, alpha (*PRKCA*) by miR-128.

Enrichment of "actin cytoskeleton signaling" and "PI3K/AKT signaling" pathways was unique to *TMEM127*-related tumors. In the actin cytoskeleton signaling pathway, integration results predicted that let-7b and let-7c targeted adenomatosis polyposis coli 2 (*APC2*), miR-29b and miR-137 targeted cell division cycle 42 (*CDC42*), miR-196a targeted radixin (*RDX*), miR-495 targeted ezrin (*EZR*), and miR-96 targeted Src homology 2 domain containing transforming protein 1 (*SHC1*). For the "PI3K/AKT signaling" pathway, genes predicted as miRNA targets included cyclin D1 (*CCND1*) by miR-202, both forkhead box O3 (*FOXO3*) and PIK3R1 by miR-96, and GRB2-associated binding protein 2 (*GAB2*) by let-7b, let-7c and miR-96.

"Gamma-aminobutyric acid (GABA) receptor signaling" and "cardiomyocyte differentiation via bone morphogenetic protein (BMP) receptor signaling" pathways were uniquely enriched in *MAX*-

related PPGL. In the "GABA receptor signaling" pathway, predicted miRNA regulated genes included N-ethylmaleimide-sensitive factor (*NSF*) by miR-199a-5p, GABA A receptor B3 (*GABRB3*) by miR-381, miR-485-5p and miR-539, *GABRG2* by miR-376a, and 4-aminobtyrate aminotransferase (*ABAT*) by miR-96. Mir-542-3p and miR-758 were predicted to target *BMP7*, while the BMP receptor type 1B (*BMPR1B*) was a predicted target of miR-96, miR-381, miR-130a, and miR-495 in the former.

4.2.6. Similar miRNA-regulated pathways in "Cluster 2" tumors

There was some overlap between significantly enriched pathways identified among the PPGL experimental groups. In fact, predicted miRNA-regulated pathways were the same or similar among experimental groups belonging to the same cluster (pseudohypoxic or cluster 2). For instance, "cluster 2" tumors (*RET*, *NF1*, *MAX*, and *TMEM127*) showed enrichment in pathways associated with PI3K/AKT, RAS, and mTOR signaling. In this regard, "mTOR signaling", "PTEN signaling", "phospholipase C signaling", and "LPS-stimulated MAPK signaling" pathways were found enriched in RET-, NF1-, and TMEM127-related PPGLs, while the "protein kinase A signaling" pathway was enriched in *RET*-, *TMEM127*-, and *MAX*-related PPGL. Similarly, *RET*- and *TMEM127*-associated tumors were enriched in the "NGF signaling" pathway, and the "SAPK/JNK signaling" pathway was enriched in *RET* and *NF1* mutant PPGLs. Finally, the "ERK/MAPK signaling" and "p70S6K signaling" pathways were significantly enriched in *RET*-, *NF1*-, *TMEM127*-, and *VHL*-related PPGL.

4.2.7. MiRNAs deregulated in PPGLs may have roles in neuronal/ neuroendocrine-like differentiation

Interestingly, we observed that neuronal and neuroendocrine-like differentiation was a common feature among the potential miRNA-regulated pathways. For instance, those *SDHB*-related pathways included "axonal guidance signaling," "synaptic long term potentiation," and "dopamine-DARPP32 feedback in cAMP signaling." Predicted miRNA target gene interactions with reported functions in neuronal or neuroendocrine-like differentiation were not only unique to *SDHB*-related, but a common feature in all PPGL experimental groups, including those belonging to cluster 2, such as *MAX*-mutant tumors. Significant enrichment in "CREB signaling in neurons," "neurotrophin/TRK signaling," and "P2Y purigenic receptor signaling" pathways were among the potential miRNA regulated pathways in *MAX*-associated tumors. Specific examples potential miRNA-mRNA interactions in *MAX* mutant involved in these pathways, include brain-derived neurotropic factor (*BDNF*) targeted by miRs-370/381/382/495, *CREB5* by miRs-539/543/495, *PIK3R1* by miRs-376a/376b/495, and sortilin-related VPS10 domain containing receptor 1 (*SORCS1*) by miR-382/495.

Furthermore, predicted miRNA–mRNA interactions for individual miRNAs were further explored to obtain a more comprehensive view into their possible biological functions biological function.

Because of the poor prognosis associated with *SDHB*- related PPGLs, we were interested in examining those genes predicted as miR-183 and miR-96 targets, which we previously validated as uniquely overexpressed in these tumors [174]. Among the 101 potential miR-183 and miR-96 targets, there were genes involved with neuronal or neuroendocrine-like differentiation, such as *EZR*; Rho GTPase-activating protein 18 (*ARHGAP18*); CTD small phosphatase 1 (*CTDSP1*); FERM, RhoGEF (*ARHGEF*) and pleckstrin domain protein 1 (*FARP1*); and leucine-rich, glioma inactivated 1 (*LGI1*).

4.2.8. MiRNA-183/-96 inhibit NGF-induced differentiation

As our integration analysis suggested that miR-183 and mir-96 could be implicated in neuronal/neuroendocrine-like differentiation, we wanted to further examine the role of these miRNAs in PPGL differentiation. Using PC12 miRNA expression data from the Hamada et al. (2012) study, we determined that miR-183 and miR-96 were not overexpressed and that expression levels remained constant throughout NGF-induced differentiation (data not shown) [152]. After determining that the PC12 cell line was suitable, we measured the effect of miR-183 and/or miR-96 on neuronal differentiation in PC12 cells in the presence of low-dose NGF.

Using the cellular length, border length, and roundness of PC12 cells as parameters to quantify neuronal differentiation, we determined that miR-183 and/or miR-96 transfected cells were significantly different from NGF-positive control PC12 cells (Figure 4.2.2). In fact, miR-183 and/or miR-96-transfected cells in the presence of low-dose NGF closely resembled NGF-negative control PC12 cells. These results indicate that miR-183 and/or miR-96 hinder neuronal differentiation of PC12 in the presence of low-dose NGF.

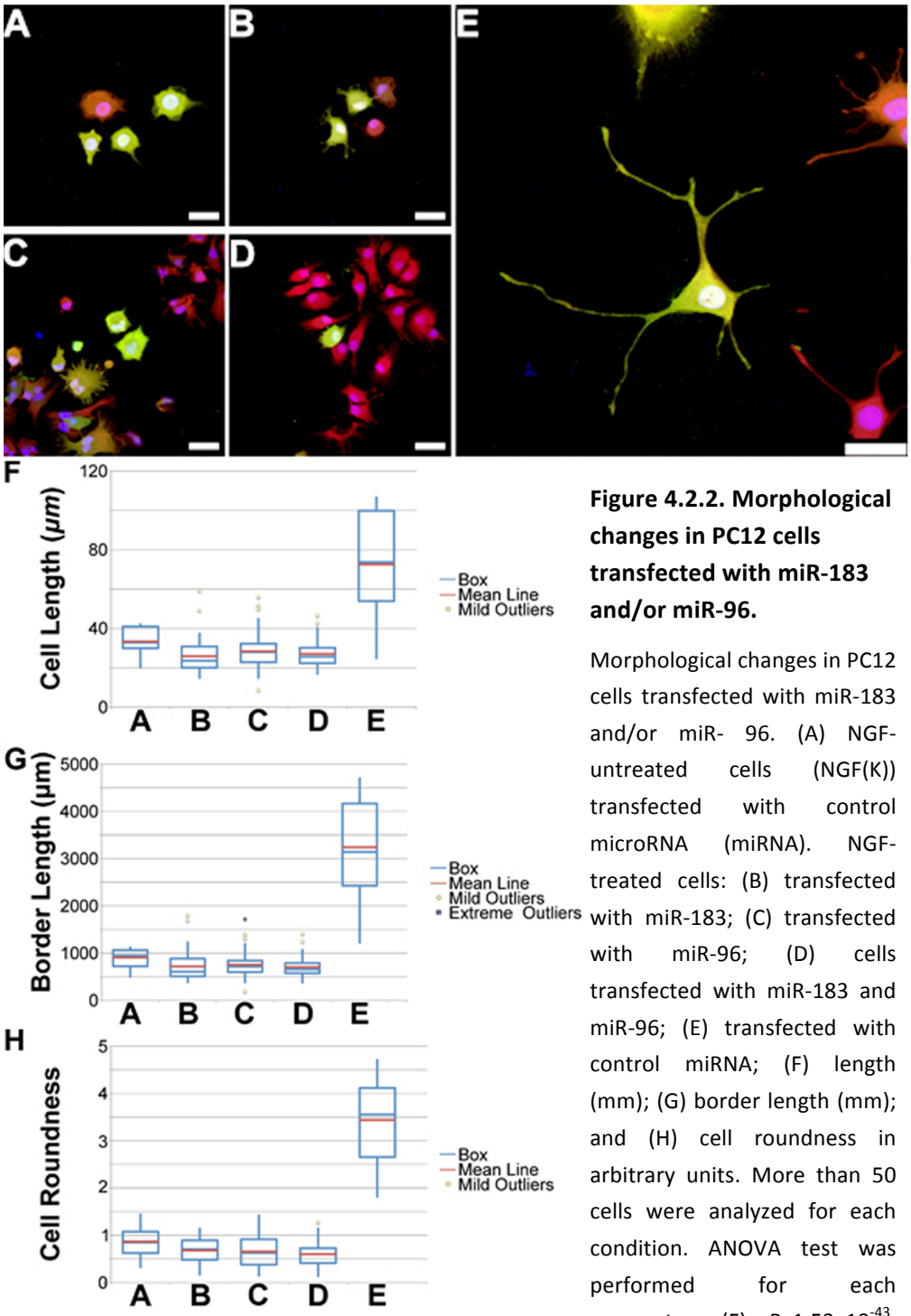

Figure 4.2.2. Morphological changes in PC12 cells transfected with miR-183 and/or miR-96.

Morphological changes in PC12 cells transfected with miR-183 and/or miR- 96. (A) NGF-untreated cells (NGF(K)) transfected with control microRNA (miRNA). NGF-treated cells: (B) transfected with miR-183; (C) transfected with miR-96; (D) cells transfected with miR-183 and miR-96; (E) transfected with control miRNA; (F) length (mm); (G) border length (mm); and (H) cell roundness in arbitrary units. More than 50 cells were analyzed for each condition. ANOVA test was performed for each parameter: (F) $P=1.53\text{x}10^{-43}$, (G) $P=4.95\text{x}10^{-68}$, and (H) $P=6.00\text{x}10^{-79}$. Scale bar: 25 mm.

4.2.9. Proteomic analysis validates miRNA-mRNA integration & offers insight into miRNA mode of regulation

To validate our miRNA–mRNA integration results and assess possible posttranscriptional miRNA regulation, we utilized mass spectrometry to analyze protein levels in two *SDHB*- and two *MAX*-related PPGLs. *MAX*-related PPGLs were selected for proteomic analysis because the PC12 cell line has been firmly established as a model system for *MAX*-mutant tumors. We identified a total of 1808 proteins in one or both PPGL experimental groups (data not shown).

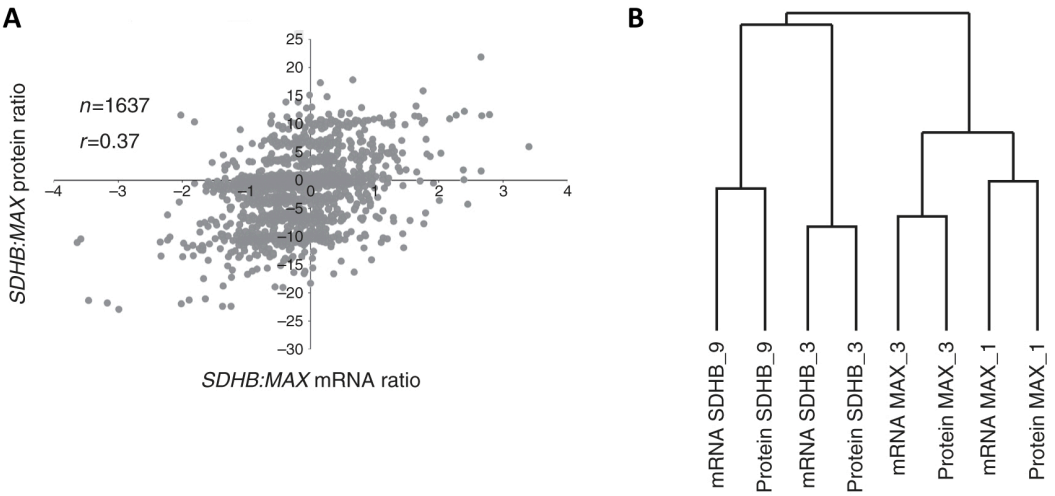

Figure 4.2.3. Proteomic and transcriptomic profiles for SDHB- and MAX-associated PPGLs. A) Scatter plot shows LOG2 transformed mRNA ratios (SDHB::MAX) vs. protein ratios (SDHB::MAX) for those genes (n=1,637) found in common in both platforms (Pearson's coefficient=0.38; $P=1.20x10^{-54}$). B) Unsupervised hierarchical cluster analysis performed with matched mRNA transcript and protein levels (n=1,637) for *SDHB*- and *MAX*-related tumors by average linkage clustering method.

Having identified miRNA, mRNA, and protein signatures for these four tumors, we ascertained the relationship between the transcript expression and protein abundance. For the 1637 genes for which both transcript and protein levels were measured between *SDHB* and *MAX*, the correlation was moderate but significant (Figure 4.2.3. A.). Thus, to evaluate the global structure of the data, the expression of the genes measured at both transcript and protein levels were subjected to unsupervised hierarchical clustering (Fig. 4.2.3. B). This analysis showed a clear division of the profiles into branches according to genetic background as mRNA and protein samples from the same tumor were consistently clustered together. This demonstrated that mRNA and proteomic profiles were compatible.

As miRNAs have been reported to regulate gene expression by inducing target mRNA degradation, translational truncation, or both, we separately compared positively and negatively correlated miRNA–mRNA interactions with the corresponding proteomic data. Comparison of negatively correlated miRNA-mRNA interactions with proteomic data allowed us to assess miRNA

regulation of gene expression induced by target degradation. While miRNA regulation occurring by translational truncation (post-transcriptional) was evaluated comparing positively correlated miRNA–mRNA interactions with proteomic data.

In total, protein data were available for 36 negatively and 25 positively correlated miRNA–mRNA interactions between *SDHB*- and *MAX*-related tumors. None of the 25 positively correlated interactions were confirmed at the protein level. Interestingly, among the 36 negatively correlated interactions, four were confirmed at the protein level. These included the following miRNA–mRNA pairs: miR183/96-*EZR*, miR183-*PPP2R5C*, miR410-*HTRA2*, and miR433-*OXCT1*. These results suggest that the mode of miRNA-mediated regulation of gene expression in PPGL occurs at the transcriptional level through target degradation.

4.3. Part 3. Chromosomal alterations in PPGL

Genomic alterations, such as chromosomal aberrations, are key causative events of tumorigenesis and disease progression. Genomic alterations in tumor cells range in size from single base changes to insertions and deletions of large chromosomal fragments and even whole genome duplications. Previously, the genomes of PPGLs have been extensively characterized by array-comparative genomic hybridization (CGH). However, tumors often deviate from the diploid state and many contain multiple populations of both tumor and nontumoral cells, which complicates correct assembly and interpretation of these data. For these reasons, most studies have been limited to reporting gains and losses.

Thus, in this regards, the objective of this thesis project was to characterize chromosomal alterations in PPGL. This is the first study where high-density SNP genotyping in these tumors has been applied to investigate chromosomal alterations in PPGLs. Besides identifying chromosomal alterations, we also estimated tumor cell ploidy and aberrant cell fraction in PPGLs with different genetic backgrounds. Finally, we assess molecular events at chromosome 14 in *MAX* mutant tumors.

4.3.1. High-density SNP genotyping in PPGL

We performed genotyping of 90 PPGL samples using Illumina Human OnmiExpress 700K SNP chips. Using the ASCAT (allele-specific copy number analysis of tumors) algorithm to analyze SNP chip data, we were able to estimate the fraction of aberrant cells and the tumor ploidy, as well as produce whole-genome allele-specific copy number profiles. The ASCAT algorithm is able to calculate the allele-specific copy numbers of all assayed SNPs, taking into account tumor aneuploidy and the fraction of aberrant tumor cells.

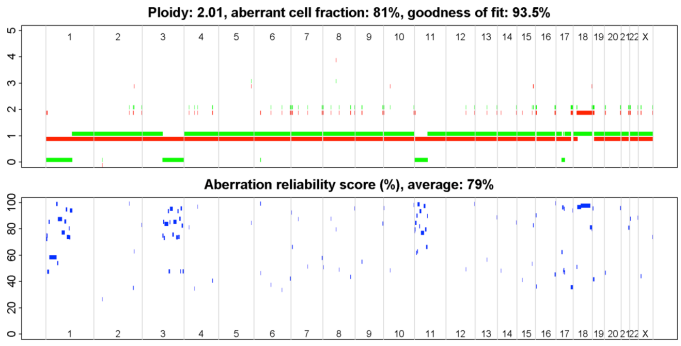

Figure 4.3.1. Example of ASCAT profile for NF1 tumor (NF1_4). ASCAT profile for tumor shown in upper panel. The estimated ploidy, aberrant cell fraction, and goodness of fit value provided above ASCAT profile. The ASCAT profile displays allele-specific copy number of all assayed loci. The copy number is displayed on the y axis., while the genomic location is shown on the x axis. The green bars corresponds to allele with lowest copy number. The red bars corresponds to allele with highest copy number. For all aberrations found, an aberration reliability score is calculated (lower panel).

Figure 4.3.1. shows an ASCAT profile for an *NF1* mutant PPGL. Each ASCAT profile reports the estimated ploidy and aberrant cell fraction for a tumor, which in this example was 2.01 and 81%, respectively. The ASCAT profile is represented with the copy number on the y axis and

the genomic location on the x axis. The green and red lines represent the alleles. For illustrative purposes, the lines are slightly shifted such that they do not overlap. The allele with the lowest copy number is shown in green, while the red line corresponds to the allele with the highest copy number. Finally, an aberration reliability score is calculated for all aberrations identified.

4.3.2. Ploidy and aberrant cell fraction in PPGLs

To investigate the relevance of aneuploidy and involvement of non-aberrant cells in PPGL, we examined the ploidy and aberrant cell fraction for our PPGL collection. Since the specimens had been previously evaluated by two pathologists to include only samples with at least 80% tumor cells, the aberrant cell fraction should reflect intratumoral non-aberrant cells and not normal cells surrounding the tumor. We found that our PPGL specimens are on average infiltrated with 32% (median 27%) non-aberrant cells.

The mean ploidy of these tumors was 2.16 (median 1.91) with 69% of samples having a ploidy less than 2.00. The remaining 41% of tumors with a ploidy greater than 2.00 included 13 WT specimens, 3 *RET*-, 2 *SDHB*-, 2 *EPAS1*-, 1 *NF1*-, and 1 *MAX*-related PPGLs. Six out of ten malignant PPGLs had a ploidy greater than 2.00. Then we explored the ploidies and aberrant cell fractions for each of the genetic groups of PPGLs (Figure 4.3.2.). In general, PPGL genetic groups had similar ploidy and aberrant cell fractions. However, *SDHD*-related PPGLs showed substantially lower aberrant cell fractions (mean 36%) compared to the other genetic groups (Figure 4.3.2. A). *VHL* mutant tumors had the second lowest aberrant cell fractions with an average of 53 percent. The remaining genetic groups had approximately 70-80% aberrant cells.

With the exception of *MAX*- and *EPAS1*-related, as well as tumors, the ploidies found for PPGL genetic groups were centered around 2.0n (Figure 4.3.2. B). However, the high ploidy found in *MAX* mutant and WT tumors was caused by an outlier samples and may not represent the ploidy of these tumors as a whole. The median ploidies of MAX and WT tumors (1.94 and 2.00 respectively) may be more accurately represent tumors these groups as a whole. On the other hand, *EPAS1* mutant PPGLs showed a higher ploidy of on average 2.64.

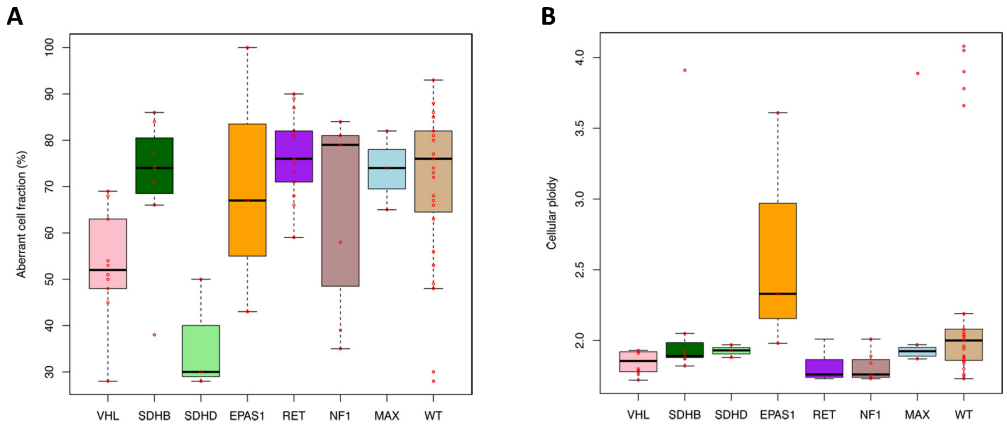

Figure 4.3.2. Aberrant cell fraction and cell ploidy for PPGL genetic groups. A) Aberrant cell fraction (%) and B) cellular ploidy for PPGL genetic groups as calculated by ASCAT

4.3.3. Chromosomal alterations in PPGLs

Table 4.3.1. provides a summary of chromosomal alterations found in our series of PPGLs. Loss of the short arm of chromosome 1 (1p) was the most common chromosomal alteration, present in 64.4% of PPGL samples. Although widely observed in our tumors, loss of 1p was not so prevalent in *SDHD*- and *VHL*-related PPGLs (20% and 0%, respectively).

Loss of the long arm of chromosome 3 (3q) was the next most frequently observed alteration (present in 50% of PPGLs). Interestingly, thirty-one out of the forty-four tumors with loss of 3q concurrently showed loss of chromosome 1p. Concurrent loss of 1p and 3q was associated with *RET*- and *NF1*-related cases (87.5% and 62.5% respectively). Nine out of 30 WT tumors (30%) also had loss of 1p and 3q.

Present in 42%, loss of the short arm of chromosome 11 (11p), was a relatively common event in our collection of PPGLs. Loss of 3p was another frequently observed alteration, which was found in 35% of tumors. Interestingly, concurrent loss of 3p and 11p was another prominent feature in our series of tumors (n=20; 22.2%). Among these 20 samples with loss of both 3p and 11p, fourteen harbored mutations in the *VHL* gene.

Table 4.3.1. Summary of chromosomal alterations in PPGL

Alteration(%)[a]	**Tot**	**VHL**	**SDHB**	**SDHD**	**EPAS1**	**RET**	**NF1**	**MAX**	**TMEM127**	**HRAS**	**WT**
loss all chr1	4.4	6.7	-	-	25	-	12.5	-	-	-	3.3
loss 1p	64.4	20	77.8	-	25	100	100	33.3	100	100	56.
loss 2p	-	-	-	-	75	-	-	-	-	-	10
loss 2q	4.4	-	22.2	-	-	-	-	-	100	-	10
loss all chr3	28.9	66.7	44.4	-	25	43.8	12.5	-	-	-	6.7
loss 3p	33.3	86.7	44.4	33.3	25	43.8	12.5	-	-	-	6.7
loss 3q	50	46.7	44.4	-	25	87.5	62.5	-	100	100	33.
loss all chr11	16.7	46.7	22.2	100	-	6.3	-	-	-	-	3.3
loss 11p	42.2	93.3	66.7	100	75	25	12.5	-	-	-	16.
loss 1p & 3q	34.4	-	22.2	-	-	87.5	62.5	-	-	100	30
loss 3p & 11p	22.2	93.3	22.2	33.3	25	12.5	-	-	-	-	-
loss 14q	15.6	-	11.1	33.3	25	25	12.5	100	-	-	10
UPD[b] chr14q	3.3	-	-	-	-	-	-	100	-	-	-
loss 17p	27.8	6.7	11.1	-	-	62.5	-	33.3	-	-	36.
loss 17q	8.8	-	-	-	-	-	100	-	-	-	-
loss chr21	24.4	13.3	-	-	25	68.8	-	33.3	-	-	16.
loss chr22	30	6.7	22.2	-	50	43.8	37.5	66.7	100	100	23.
Total *N*[c]	90	15	9	3	4	16	8	3	1	1	30

a) Percentage of tumors with a given chromosomal alteration. 2) UPD or Uniparental disomy.
c) Total number of samples provided in last row.

Chromosome 17p was lost in 28.7% of tumors. Loss of 17p was particularly prevalent in *RET*-related PPGLs with ten out of fifteen *RET*-related PPGLs presenting loss of 17p. WT PPGLs also frequently showed loss of 17p (36.7%). On the other hand, besides two tumors with complete loss of chromosome 17, loss of 17p was not observed in any of the *NF1* tumors. Rather all NF1 mutant tumors showed loss of the first half of chromosome 17q.

Chromosomes 21 and 22 were also frequently lost in PPGLs. Twenty-three percent of samples presented loss of chromosome 21, while chromosome 22 was deleted in 30% of tumors. Loss of chromosome 21 was associated with *RET* mutant PPGLs (60%). All ten *RET*-related tumors with loss of chromosome 21 also presented loss of 1p and 3q. Seven out of 10 *RET*-related tumors with loss of chromosome 21 also showed loss of 17p. Interestingly, no NF1-related tumors had lost chromosome 21.

Loss of chromosome 14 (14q) was observed in 15.6% of tumors. For the most part, 14q was lost through conventional deletion of one allele with the exception in *MAX*-related PPGLs. In *MAX*-related tumors, one copy of chromosome 14q is lost and the other copy duplicated resulting in LOH, commonly referred to as a "uniparental chromosomal disomy" or a copy neutral event. Disomy of chromosome 14 was a hallmark of *MAX*-related PPGLs.

As we previously had reported, we observed an exclusive gain of chromosome 2p in three out of four (3/4) *EPAS1* tumors, which was extremely relevant given that the *EPAS1* gene is located on chromosome 2p21-p16 [64]. We were unable to detect any alterations of chromosome 2p in the ASCAT profile for the fourth *EPAS1* tumor.

The only *TMEM127*-related tumor in this study showed loss of 1p and chromosome 22. Interestingly, this *TMEM127* mutant tumor had loss of chromosome 2q, where the *TMEM127* gene is located.

4.3.4. Imprinted genes affected by chr14 UPD in MAX tumors

Since chromosome 14 UPD was unique to *MAX* mutant tumors, we thought that it might be important for tumorigenesis in these tumors (Figure 4.4.3. A-C). Thus, we performed a more in-depth analysis of the molecular events at chromosome 14 in *MAX* mutant tumors. Previously, we reported down-regulation of the large maternally expressed miRNA cluster also located at chromosome 14q32.2 [174]. In the Figure 4.3.3 B, the circos plot representation of heatmaps for the 14q32.2 miRNA cluster clearly shows down-regulation of these miRNAs in *MAX* mutant tumors relative to the other genetic groups. These results provided further evidence supporting loss of chromosome 14 in *MAX*-related tumors observed by ASCAT analysis.

The DLK1/MEG3 differentially methylated region (DMR) is also located at chromosome 14q.32.2. These two genes are reciprocally imprinted: only the paternal allele of the *DLK1* gene is expressed, while the maternal allele of *MEG3* (maternally expressed gene 3) is expressed. Thus, a normal human genome should contain one methylated (paternal) *MEG3* allele and another unmethylated (maternal) *MEG3* allele. Using gene expression data we had available from a previous study, we assessed the expression of *MEG3* and *DLK1* in a large series of PPGLs, including *MAX*-associated tumors [59,102].

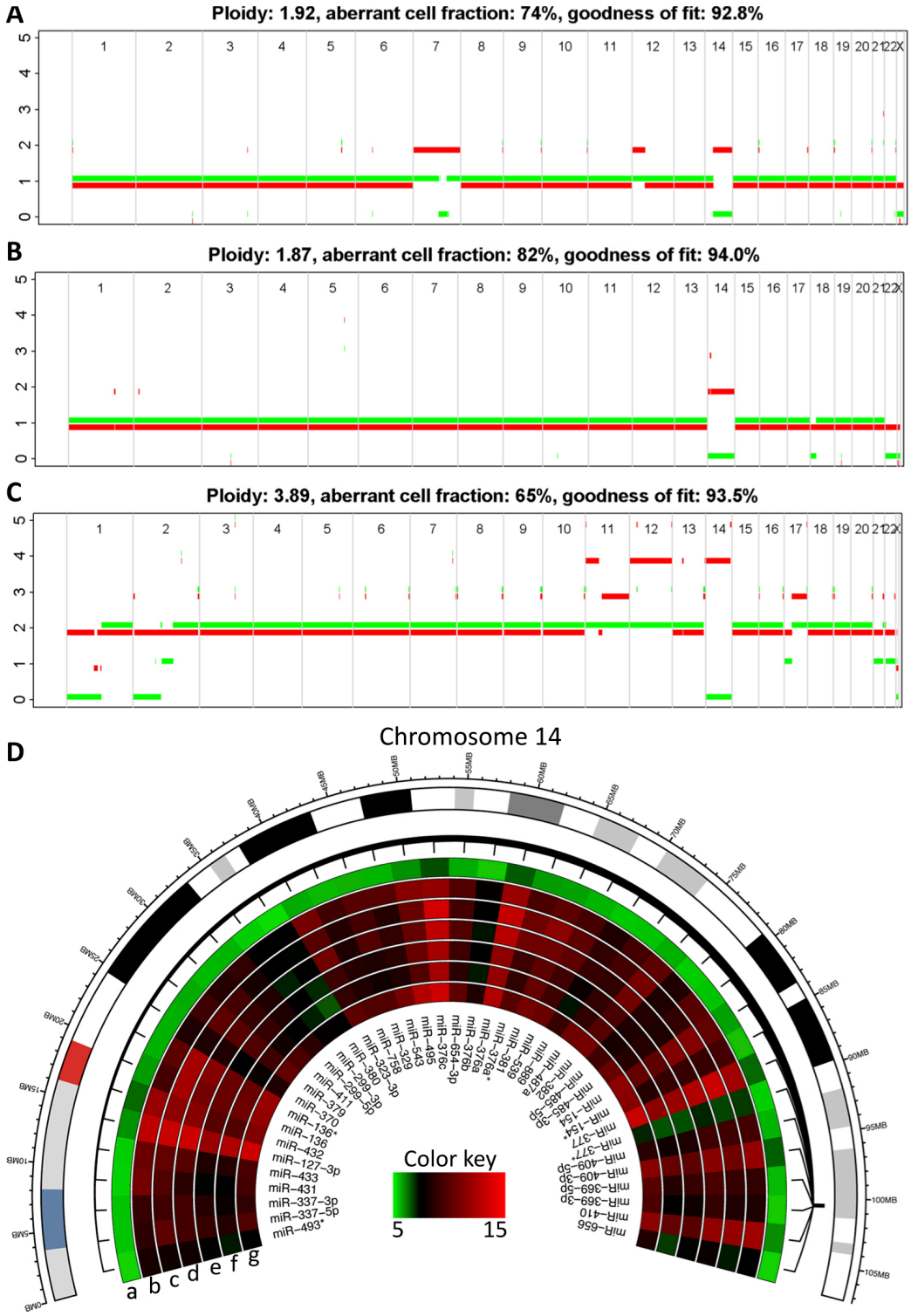

Figure 4.3.3. Molecular events at chromosome 14.

A-C) ASCAT profiles for *MAX*-associated tumors clearly shows chromosome 14 UPD with duplication of one allele and deletion of the other. A) ASCAT profile for *MAX*_1 tumor. B) ASCAT profile for *MAX*_2 tumor. C) ASCAT profile for *MAX*_3 tumor. D) Circos plot showing heatmaps for the 14q32.2 miRNA cluster located at chromosome 14. Circos plot with heatmaps showing expression of large 14q32.2 miRNA cluster for PPGL genetic groups. First track shows an ideogram representation of chromosome 14. PPGL genetic groups arranged (starting with outermost track) in following order: a) *MAX*, b) *VHL*, c) *SDHB*, d) *SDHD*, e) *RET*, f) *NF1*, and g) *TMEM127*. Black arrow indicating miR-382, which was up-regulated in all PPGL genetic groups except for in *MAX* tumors (*de Cubas et al., 2013*).

We did not observe any significant differences in *DLK1* expression for *MAX*-associated tumors (data not shown). However, we did find a highly significant down-regulation of *MEG3* among *MAX* mutant tumors relative to all other PPGLs (Figure 4.3.4. A). Then we performed a MSP of the *MEG3* promoter to assess the methylation status of this locus. As shown in Figure 4.3.4 B, MSP analysis revealed loss of the unmethylated (maternal) *MEG3* allele in all three *MAX*-associated tumors.

Two alleles are clearly visible in control PPGL DNAs from other cluster 2 samples. During the discovery of the *MAX* gene, Burnichon et al. elegantly provided evidence indicating that there were actually two copies of chromosome 14 through retrospective analysis of CGH data previously obtained for these three tumors to show that there were no gains or losses on chromosome 14 [62]. Taken altogether, these evidences show that *MAX*-associated tumors do indeed have a chromosome 14 UPD. This also demonstrates the accuracy and the utility of high density SNP-array genotyping, as well as the ASCAT algorithm in these solid tumors to detect chromosomal alterations, especially those involving copy neutral events.

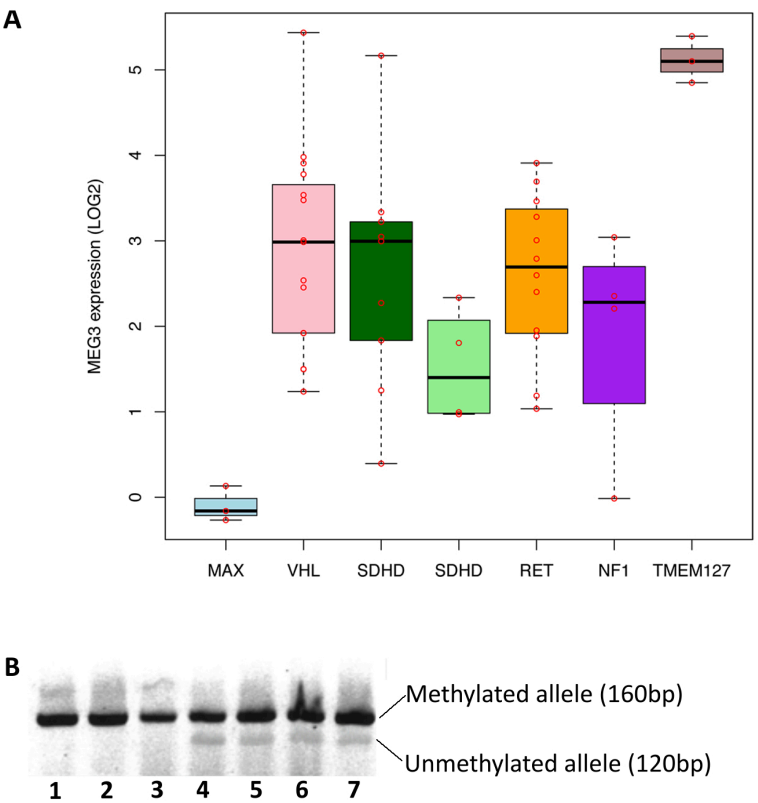

Figure 4.3.4. *MEG3* gene expression and promoter methylation.
MEG3 is a noncoding RNA located at chromosome 14q32.2. A) Average *MEG3* expression in PPGL genetic groups; B) Methylation specific PCR of *MEG3* promoter. Band at 160bp corresponds to the methylated allele. The band at 120bp corresponds to the unmethylated allele. Lanes 1 to 3 contains *MAX* samples: (1) MAX_1; (2) MAX_2; (3) MAX_3. Lanes 4 to 6 contains other "cluster 2" samples: (4) RET_5; (5) RET_7; (6) NF1_3. Lane 7 contains (7) lymphocyte control DNA.z

4.4. Part 4. DNA methylation profiling in PPGL

Extensive clinical and genetic characterization over the last 25 years has greatly improved our knowledge about the genetic basis underlying these tumors, but the lack of reliable markers of malignancy continues to complicate disease management. Previous studies have described molecular markers of varying nature, but their predictive values seem limited due to difficulties in replicating in different populations [175]. Fortunately, recent improvements in high-throughput technologies have fueled advances in our understanding of biology. In this regard, DNA methylation has become one of the most widely studied epigenetic modifications in human pathogenesis, as well as in normal development. It is now recognized as an important epigenetic mechanism that can influence gene expression independently from the genetic code and can be inherited through cell divisions.

To date, only one genome wide study has been published evaluating DNA methylation patterns in a large series of PPGLs [66]. Although the reasons behind the global hypermethylation observed in *SDHx*-related PPGLs have been amply investigated, the prognostic potential of DNA methylation in PPGLs has yet to be explored in depth [66].

In this study, we disposed of two independent methylomes from large and well-characterized series of PPGLs, used as a discovery series (DS) and as a validation series (VS1). This allowed us to obtain a comprehensive insight into the DNA methylation landscape in this rare tumor. These outstanding collections were enriched with malignant PPGLs that permitted us to identify prognostic markers independent of genotype. We identified and validated 52 CpGs differentially methylated between malignant and benign PPGLs. Moreover, 48 of these CpGs showed highly significant associations with progression-free survival (PFS) independently of tumor genetic status, which suggest their potential use in the risk stratification of patients. Finally, we validated hypermethylation of *RDBP* in another independent validation series (VS2) by pyrosequencing.

4.4.1. DNA methylation profiling in DS and VS1

DNA methylation data for DS tumors was deposited on gene expression omnibus under the GEO accession number GSE62231, and the ten additional metastatic PPGLs of the VS1 tumors from the COMETE collection under the accession number GSE43298. Probes mapping to the X or Y chromosomes (n=1085 or n=7, respectively), as well as unreliable probes not detected with p>0.01 in more than 5% of samples (n=1029), were removed. The remaining 25,457 probes were used for subsequent analyses, and after preprocessing data, we obtained β- and M-values of these CpGs for DS PPGLs.

M-values are defined as log2 (methylated probe intensity/unmethylated probe intensity). Negative M-values indicate less than 50% methylation and positive M-values indicate more than 50% methylation [171]. M-value conversion corrects for the heteroskedasticity observed for beta-values, producing a homoskedastic distribution that is more appropriate for statistical analysis.

Thus, M-values were used for statistical analysis, while beta-values were used for biological interpretation. The Beta-value is defined as the ratio between the methylated probe intensity and the overall intensity (sum of methylated and unmethylated probe intensities) [169]. VS1 DNA methylation data was processed the same way as DS.

4.4.2. DNA methylation in PPGL strongly influenced by genetic background

Unsupervised analysis was performed using 500 probes with the highest variance across all samples. Unsupervised hierarchical cluster analysis of DS tumors split samples into two main clusters, cluster 1 and 2 (Figure 4.4.1. A). Cluster 1, enriched with VHL- and SDHx-related tumors, can be subdivided into 2 subclusters (1A and 1B). Subcluster 1A contained seven out of eight SDHB- and all SDHD-related tumors, as well as 5 WT PPGLs.

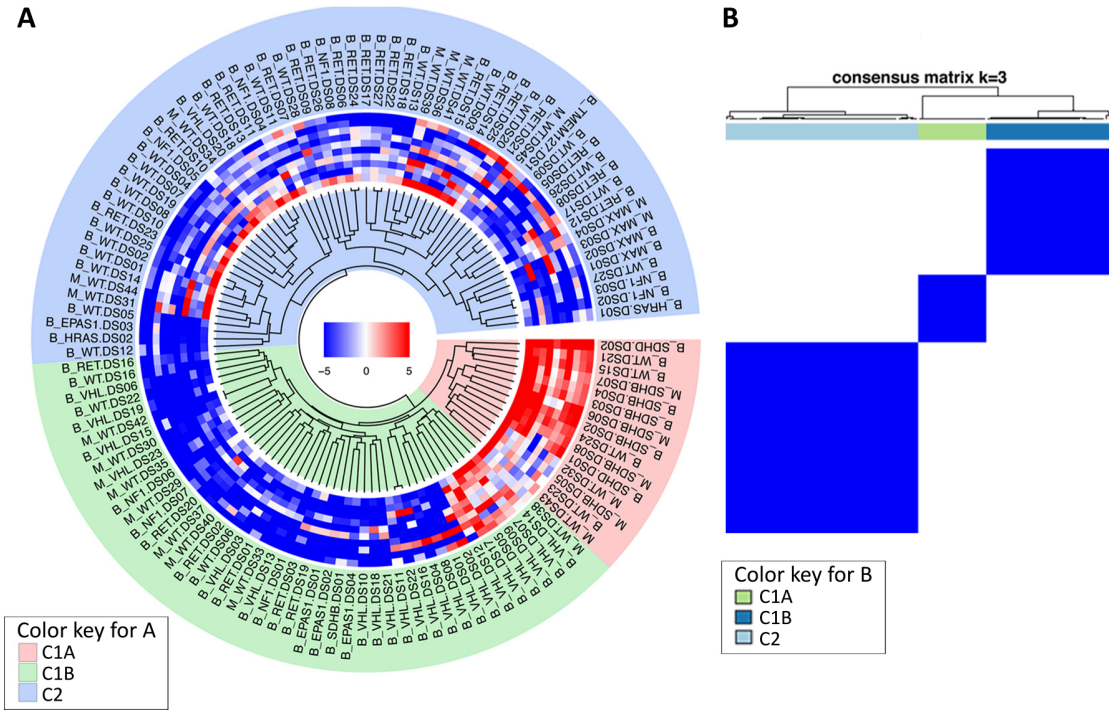

Figure 4.4.1. Unsupervised analyses of PPGL DNA methylation profiles
Unsupervised cluster analyses of PPGL samples based on their DNA methylation patterns. The top 500 probes with the highest variance across all samples we used for unsupervised analyses. A) Hierarchical cluster analysis: Distance was calculated by Pearson's correlation method and CpGs were clustered by complete linkage clustering method. Heatmap shown for top 10 CpGs. Hypermethylated CpGs are shown in red, whereas hypomethylated CpGs are indicated in blue. "M" or "B" prefix in from of sample names indicates "malignant" or "benign," respectively. Cluster C1A (indicated by pale red highlight) represented hypermethylator group, containing SDHx tumors. Cluster C1B (indicated by green highlight) contained VHL and EPAS1 tumors, with intermediate methylation. Cluster C2 (indicated by light blue highlight) had samples with lowest levels of global methylation and contained RET, NF1, TMEM127, MAX, and HRAS tumors. B) K-means clustering of DNA methylation profiles. Optimal classification defined three (3).

In total, subcluster 1A was composed of 15 tumors of which 6 were malignant. Subcluster 1B contained 22 VHL-, 1 SDHB-, 6 RET-, 3 NF1-, and 3 EPAS1-related PPGLs, as well as 11 WT tumors. Subcluster 1B contained 9 cases with metastases and 37 without. In addition to the remaining 20

RET-related tumors, cluster 2 contained 5 NF1-, 2 HRAS-, 1 TMEM127-, 1 VHL-, and 1 EPAS1-related PPGLs and 28 WT specimens. Nine of the 62 tumors in cluster C2 were malignant.

To verify the result of the unsupervised hierarchical cluster analysis showing three distinct clusters, we performed k-means consensus clustering. According to this analysis, the optimal classification defined 3 tumor subgroups as shown in Figure 4.4.1. B. Cluster memberships for unsupervised hierarchical cluster and consensus cluster analyses results were highly similar with a 93% (114/123) agreement for tumor classification between the two methods. Cluster memberships for DS samples are provided in the last two columns in Supplementary Table 4.4.1.

We generated a circus plot (Figure 4.4.2) depicting methylation levels for the six genetic classes (*SDHB*, *VHL*, *EPAS1*, *RET*, *NF1*, and *MAX*). The heatmaps in Figure 4.4.2 and box plots in Figure 4.4.3 A clearly shows varying degrees of methylation among the six genetic groups of PPGLs. SDHB-related tumors had the highest levels of DNA methylation among the experimental groups. *VHL*- and *EPAS1*-related PPGLs showed intermediate levels of DNA methylation, while *RET*-, *NF1*-, and *MAX*-related tumors had the lowest levels of DNA methylation. The difference in levels of global DNA methylation was significant between the genotypes (ANOVA; P=0.001) (Figure 4.4.3 A). These results verify that *SDHB*-related tumors display a CpG island methylator phenotype (high-CIMP).

4.4.3. Supervised analyses identifies PPGL experimental group specific CpGs

Initially with PPGLs from DS1, comparisons between the different genetic groups and the *SDHB* tumors identified numerous hypermethylated and hypomethylated CpGs (Table 4.4.1). To validate the above DNA methylation patterns associated with each genetic background, the same analyses were performed in PPGLs from VS1. We filtered out those probes that were not significant and/or with insufficient difference in methylation levels. We were able to perform these analyses with *VHL*, *RET*, *NF1*, *MAX*, and *SDHB* mutated tumors in VS1, but we were not able to replicate results with *EPAS1* mutant samples as none were available in VS1 (Table 4.4.1). To further determine genotype specific CpGs, as well as those common among all genotypes, we performed another Venn diagram analysis with these confirmed probes (Figure 4.4.3 B). As expected, CpGs for *SDHB*-related tumors were almost all hypermethylated, while the other experimental groups showed a higher proportion of hypomethylated CpGs.

Table 4.4.1. Differentially methylated CpGs for PPGL experimental group comparisons

Comparison	CpGs in DS[a]		Replicated in VS1[b]	
	Hyper	Hypo	Hyper	Hypo[d]
VHL vs. *SDHB*	143	1265	28	1049
EPAS1 vs.	4	172	N/A[d]	N/A[d]
RET vs. *SDHB*	145	1266	8	1114
NF1 vs. *SDHB*	12	1476	6	1345
MAX vs. *SDHB*	8	782	2	560

a) CpGs initially identified in Discovery Series. b) CpG successfully replicated in Validation Series 1. c) Hypermethylated CpGs. d) Hypomethylated CpGs. d) Not available due to lack of EPAS1 samples in VS1.

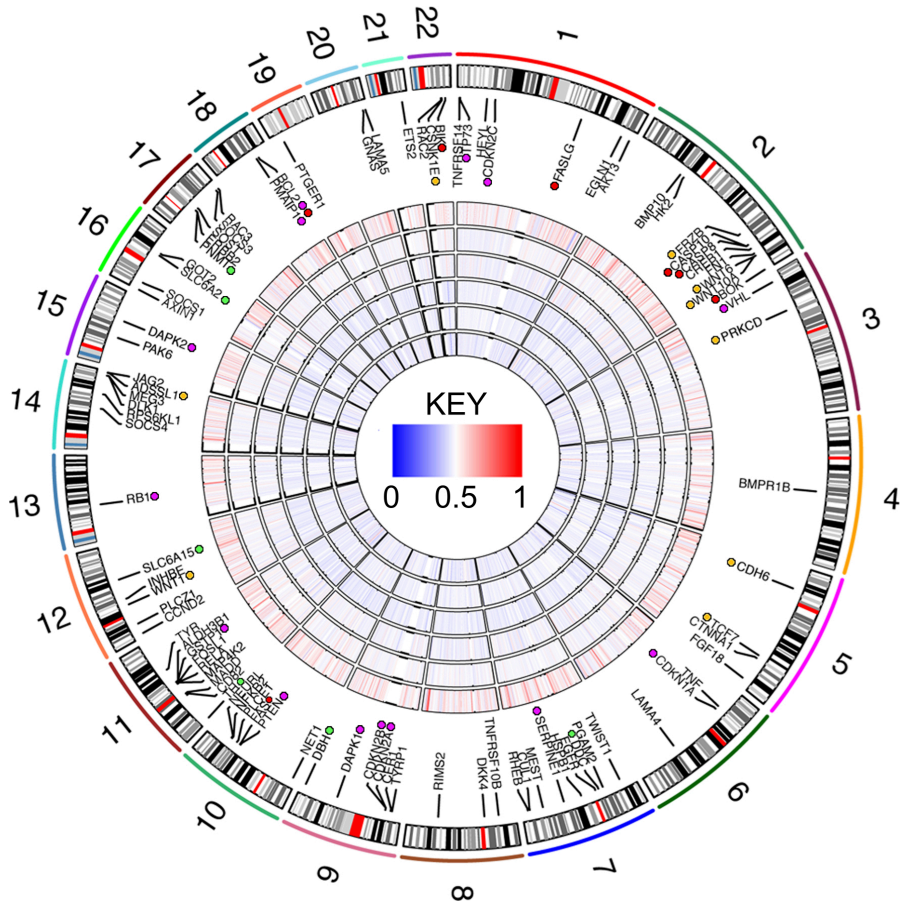

Figure 4.4.2. Circos plot of CpG methylation levels for PPGL genetic groups. From outside to in, first track provides chromosome cytobands, followed by heatmaps (A-F) showing DNA methylation for PPGL genetic groups with mutations in: (A) *SDHB*, (B) *VHL*, (C) *EPAS1*, (D) *RET*, (C) *NF1*, and (F) *MAX*. Well known tumor suppressor genes are indicated by purple dot. Genes with functions in apoptotic signaling are indicated by red dot. Genes involved with WNT signaling are indicated with a yellow dot. Green dots indicate genes involved in catecholamine biosynthesis and secretion. Heatmap legend in center: DNA methylation shown as β-values with hypermethylation in red ($0<\beta<0.5$) and hypomethylation in blue ($0.5<\beta<1$).

4.4.4. Potential pathways affected by PPGL DNA methylation

Using both David Bioinformatics Resources (DBR) and PantherDB, we performed pathway analysis using genes corresponding to differentially methylated CpGs for each comparison between genetic groups of PPGLs. Comparisons versus *SDHB*-associated PPGLs showed enrichment in pathways with key roles in tumorigenesis, such as "pathways in cancer", "MAPK signaling pathway", "p53 signaling pathways", "ECM-receptor interaction", "focal adhesion", and "apoptosis". Among the genes showing hypermethylation in *SDHB*-related tumors, where numerous well known tumor suppressor genes (TSGs) and mediators of apoptosis, as shown in Figure 4.4.2.

The most over-represented pathways among *VHL*-, *RET*-, *NF1*-, and *MAX*-related tumors relative to their *SDHB* counterparts was the "WNT signaling" pathway, followed by the "cadherin signaling", "angiogenesis", "integrin signaling", and "adrenaline and noradrenaline biosynthesis" pathways. As shown in Figure 4.4.2., *VHL*-, *RET*-, *NF1*-, and *MAX*-related tumors showed hypomethylation of key components involved in "WNT signaling".

Among the genes in the adrenaline and noradrenaline biosynthesis and signaling pathways (Figure 4.4.2.), differential methylation of *PNMT* (phenylethanolamine N-methyltransferase) and *NET* (norepinephrine transporter, *SLC6A2*) was of particular interest. *PNMT* was hypermethylated in *SDHB*-related PPGLs, while *RET* mutant specimens showed the lowest levels of methylation. Interestingly, VHL and MAX PPGLs showed intermediate and low levels of PNMT methylation, respectively. Although this study only included two *HRAS*-associated PPGLs, we observed hypomethylation of *PNMT* in these tumors (data not shown). Also of interest was the hypermethylation of *MEG3* (maternally expressed gene 3) in *MAX*-related PPGLs.

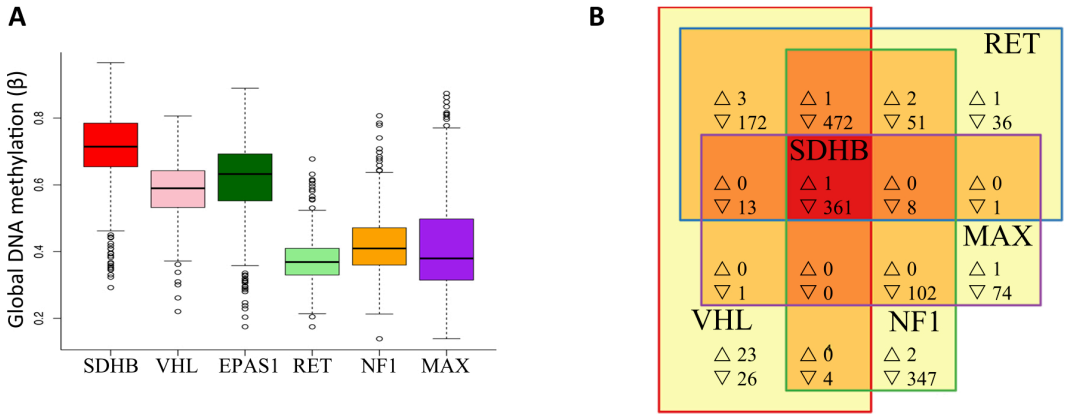

Figure 4.4.3. Global DNA methylation and group specific CpGs.
A) Global DNA methylation levels for each PPGL genetic group. Global DNA methylation represented as β-values (0<β<0.5: Hypomethylated; 0.5<β<1: hypermethylated). B) Group-specific CpGs. Venn diagram analysis performed with only those CpGs that had been replicated in VS1. All comparisons were performed relative to *SDHB* tumors. Thus, the 361 "hypomethylated" CpGs indicated in the SDHB box (red) means that these CpGs were hypomethylated relative to the other experimental groups. Thus, these 361 CpGs were actually hypermethylated in *SDHB*.

4.4.5. CpGs associated with malignancy and progression

Initial selection of CpG candidates from DS PPGLs, identified 86 differentially methylated probes (with FDR<0.10, Δβ>|0.2|, and present in at least 50% of metastatic tumors). Fifty-two CpGs were successfully replicated in VS1 (Table 4.4.2). As shown in the heatmaps in Figure 4.4.4 A, there was a high degree of concordance in methylation levels for these 52 CpGs (corresponding to 47 genes) between those tumors with and without metastases in DS and VS1.

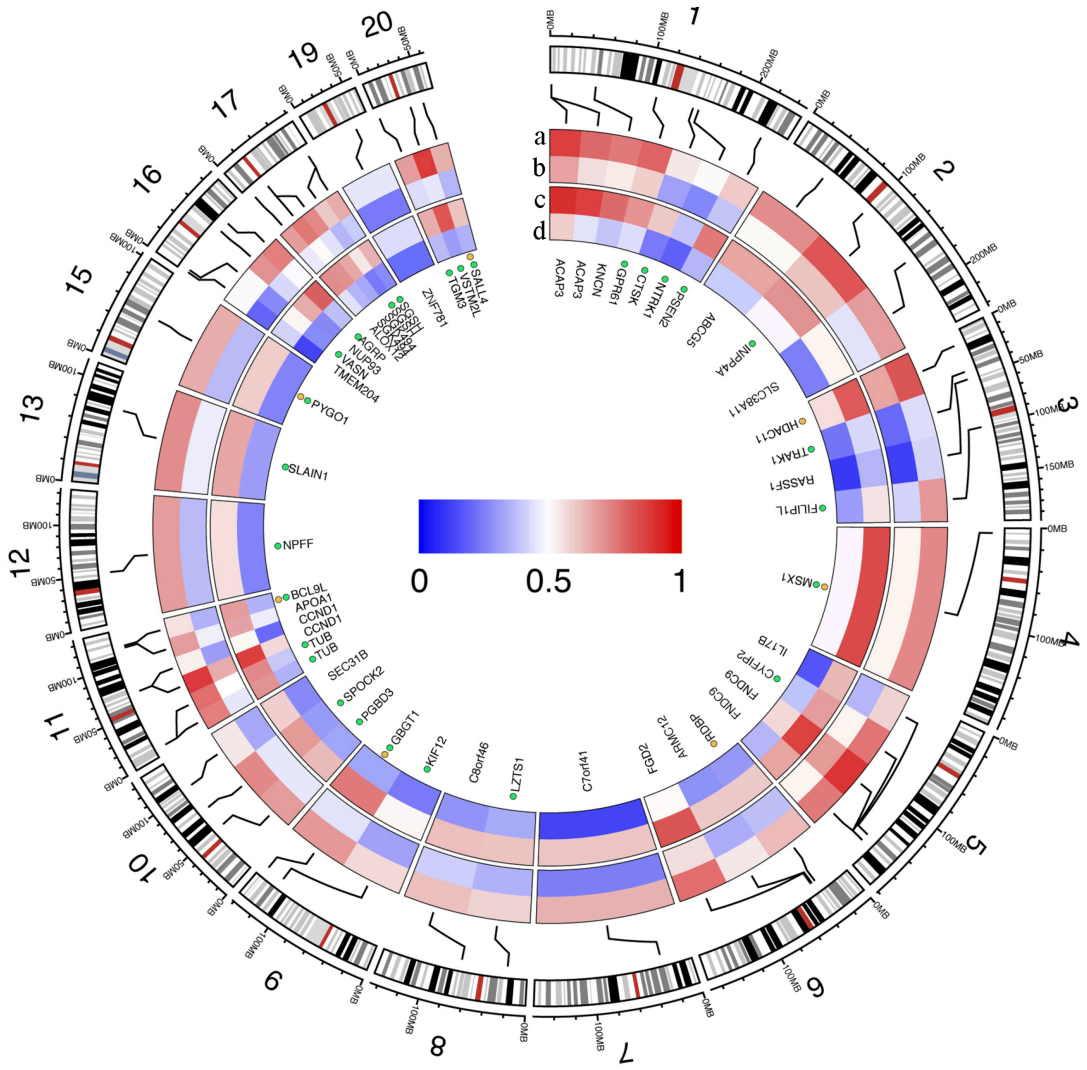

Figure 4.4.4. Circos plot showing 52 validated malignancy-associated CpGs. Outermost track provides ideogram for all chromosomes, except chromosomes 14, 18, 21, 22, X, and Y. Heatmaps show methylation levels for 52 validated CpG associated with PPGL malignancy. a) Tumors with metastasis in Discovery series (DS). b) Tumors without metastasis in DS. c) Tumors with metastasis in Validation Series 1 (VS1). d) Tumors without metastasis in VS1. Green dots indicate gene with functions in nervous system development, while genes involved with transcriptional regulation at gene promoters are indicated by orange dots. Hypermethylated CpGs are indicated in red, whereas hypomethylated CpGs are indicated in blue.

As we were interested in finding CpGs associated with malignant behavior, we verified that the above probes were not included among those reported by Letouzé and colleges as associated with *SDHB*-related tumors [66]. Survival analyses were performed using 277 tumors of which 48 were malignant. Forty-eight out from the 52 CpGs described

above showed significant associations with progression free survival (PSF), even after adjusting for the presence of *SDHB* mutations, series origin, and multiple testing including all the probes (FDR<0.1), shown in Table 4.4.2.

Table 4.4.2. Confirmed CpGs associated with PPGL malignancy

Probe ID[a]	Gene	Discovery Series			Validation Series 1			Cox Regression	
		Δβ[b]	%M[c]	FDR[d]	Δβ[b]	%M	FDR[d]	Hazard[e]	FDR[d,f]
cg25781162	ABCG5	0.21	62.5	0.04473	0.27	66.7	4.2E-05	1.6 (1.2-2.1)	0.053
cg06810461	AGRP	0.26	70.8	0.01856	0.43	83.3	1.0E-06	1.8 (1.4-2.4)	0.006
cg08946332	ALOX12	0.22	66.7	0.02038	0.27	50.0	0.00024	2.5 (1.2-2.0)	0.036
cg19324627	APOA1	0.22	62.5	0.04037	0.20	62.5	0.00787	1.5 (1.0-2.1)	0.182
cg20029201	BCL9L	0.21	62.5	0.04178	0.34	54.2	2.2E-06	1.8 (1.3-2.4)	0.012
cg17706173	TMEM204	0.29	70.8	0.0028	0.29	50.0	2.7E-06	1.7 (1.4-2.3)	0.005
cg11599505	VSTM2L	0.43	58.3	0.0707	0.50	58.3	1.3E-06	1.4 (1.2-1.7)	0.023
cg25994725	ARMC12	0.20	50.0	0.08303	0.31	50.0	2.0E-05	1.5 (1.1-2.1)	0.095
cg23704362	C8orf46	0.21	50.0	0.00848	0.33	62.5	3.3R-07	1.9 (1.4-2.6)	0.014
cg07426960	CCND1	0.21	83.3	0.0094	0.30	83.3	6.6E-06	1.9 (1.3-2.7)	0.022
cg13608094	CCND1	0.22	58.3	0.01253	0.31	83.3	3.3E-05	1.5 (1.2-2.0)	0.028
cg25203980	ACAP3	0.23	75.0	0.01253	0.43	70.8	8.1E-08	2.0 (1.5-2.6)	0.001
cg18565510	ACAP3	0.20	79.2	0.02306	0.32	75.0	3.1E-08	2.0 (1.5-2.6)	0.002
cg20802392	CTSK	0.22	62.5	0.02306	0.36	62.5	4.7E-07	2.0 (1.4-2.8)	0.007
cg00986320	CYFIP2	0.24	66.7	0.05905	0.30	66.7	1.4E-05	2.1 (1.5-2.9)	0.006
cg06436504	FILIP1L	0.28	75.0	0.00024	0.24	50.0	1.0E-06	2.1 (1.6-2.9)	0.002
cg08972170	C7orf41	0.39	54.2	0.00605	0.47	54.2	1.5E-07	1.7 (1.3-2.1)	0.005
cg00226923	FGD2	0.22	79.2	0.04389	0.33	79.2	0.00012	1.5 (1.2-2.0)	0.045
cg09076584	SGK494	0.28	70.8	0.00382	0.34	83.3	6.4R-08	2.4 (1.7-3.4)	0.001
cg22686523	SGK494	0.26	83.3	0.01037	0.36	79.2	2.7E-07	2.5 (1.6-3.8)	0.006
cg19782598	SLAIN1	0.25	62.5	0.04932	0.35	70.8	6.1E-07	2.1 (1.5-2.9)	0.006
cg19987219	KNCN	0.22	70.8	0.0552	0.39	79.2	1.7R-05	1.5 (1.1-1.9)	0.054
cg10710439	ZNF781	0.22	62.5	0.0051	0.22	70.8	0.00011	1.6 (1.2-2.2)	0.038
cg04143809	SLC38A11	0.24	75.0	0.00157	0.26	54.2	1.6E-05	2.1 (1.5-3.0)	0.006
cg01169778	GBGT1	0.25	58.3	0.04516	0.42	70.8	8.7E-08	1.9 (1.5-2.4)	0.001
cg23749046	GPR61	0.21	75.0	0.07435	0.26	62.5	0.05922	1.2 (0.9-1.5)	0.500
cg05446471	HDAC11	0.20	79.2	0.04394	0.26	75.0	0.00067	1.4 (1.1-1.8)	0.078
cg25141490	IL17B	0.22	58.3	0.01456	0.47	75.0	5.3E-07	2.0 (1.5-2.7)	0.004
cg01169610	INPP4A	0.21	66.7	0.06837	0.23	62.5	0.00114	1.4 (1.4-1.9)	0.129
cg02838492	KIF12	0.25	58.3	0.00294	0.28	79.2	9.8E-07	1.8 (1.4-2.3)	0.001
cg26917999	LZTS1	0.23	62.5	0.04651	0.27	50.0	8.3E-05	1.5 (1.1-2.0)	0.089
cg20189782	FNDC9	0.23	70.8	0.00705	0.31	62.5	1.2E-06	1.8 (1.3-2.4)	0.012
cg26790059	FNDC9	0.21	70.8	0.036	0.31	87.5	1.0E-06	1.8 (1.3-2.4)	0.012
cg09748975	MSX1	0.20	62.5	0.01988	0.36	54.2	1.1E-07	1.5 (1.2-1.9)	0.012
cg01657380	NPFF	0.31	62.5	0.00428	0.29	66.7	8.7E-08	2.1 (1.5-2.8)	0.002
cg00626119	NTRK1	0.23	62.5	0.00092	0.20	54.2	1.1E-05	1.8 (1.3-2.6)	0.029
cg10586756	NUP93	0.28	66.7	0.03922	0.39	62.5	2.3E-06	1.8 (1.3-2.4)	0.013
cg01982597	PGBD3	0.23	66.7	0.02358	0.30	75.0	8.7E-08	2.3 (1.6-3.3)	0.002
cg25514304	PSEN2	0.20	50.0	0.0389	0.39	50.0	4.2E-07	1.8 (1.3-2.4)	0.013
cg23412777	PYGO1	0.29	50.0	0.02347	0.33	62.5	4.0E-08	2.0 (1.5-2.6)	0.002
cg21554552	RASSF1	0.30	58.3	0.01604	0.24	50.0	0.00027	1.4 (1.1-1.7)	0.052
cg06351503	RDBP	0.25	50.0	0.00103	0.30	70.8	4.0E-07	2.1 (1.6-2.8)	0.001
cg06303238	SALL4	0.29	50.0	0.00983	0.26	50.0	2.5E-06	1.7 (1.3-2.1)	0.006
cg26705561	SEC31B	0.21	66.7	0.01526	0.31	54.2	5.2E-06	1.8 (1.3-2.5)	0.018
cg07675682	SGSH	0.25	66.7	0.00113	0.30	66.7	8.2E-07	2.2 (1.5-3.0)	0.005
cg05140736	SGSH	0.26	75.0	0.00144	0.38	54.2	7.5E-07	1.7 (1.3-2.2)	0.009
cg09276451	VASN	0.23	66.7	0.00762	0.24	50.0	0.00034	1.4 (1.3-1.9)	0.189
cg01861509	SPOCK2	0.27	83.3	0.01892	0.39	70.8	4.6E-05	1.7 (1.3-2.2)	0.017
cg21611708	TGM3	0.25	66.7	0.0279	0.28	66.7	0.00135	1.5 (1.2-2.0)	0.050
cg24877842	TRAK1	0.23	83.3	0.00092	0.20	54.2	6.8E-05	2.0 (1.4-2.7)	0.007
cg15480475	TUB	0.28	70.8	0.00171	0.36	70.8	2.5E-07	2.0 (1.5-2.7)	0.002
cg05492113	TUB	0.28	70.8	0.00294	0.33	79.2	4.9E-07	2.2 (1.6-3.2)	0.005

a) Illumina 27k probe ID. b) Δβ = βmalignant-βBenign. c) %M: Percent malignant tumors with alteration. d) FDR: False discovery rate, corrected over all probes in analysis (n=25,457). e) Hazard ratio (95% confidence interval) f) FDR corrected for *SDHB* mutation status and series origin.

Pathway analysis performed with genes corresponding to these 52 CpGs indicated that biological processes involving "regulation of transcription from RNA polymerase II promoter" and "nervous system development" were potentially affected (indicated in Figure 4.4.4.).

4.4.6. Validation of malignancy-associated CpGs by Pyrosequencing

To further confirm our results, we selected three malignancy-associated CpGs for validation in an independent series of FFPE PPGLs (VS2), which contained 19 metastatic tumors. These three CpGs corresponded to the following genes: *RDBP, HDAC11* (histone deacetylase 11), and *CYFIP2* (cytoplasmic FMR1 interacting protein 2). As mentioned above, these three CpGs also showed highly significant associations with progression free survival (Figure 4.4.5. A-C). Of the CpGs selected for validation, hypermethylation of *RDBP* in malignant PPGL was confirmed in VS2 with an average methylation of 39.2% in tumors without metastases and 68.0% in malignant tumors (p=0.003).

4.4.7. RDBP KO in T47D cells and PPGLs

To identify potential RDBP target genes, we downloaded gene expression data for T47D breast cancer cells with and without *RDBP* knockout from GEO under accession number GSE19940 [153]. In total, 700 genes were differentially expressed upon *RDBP* knockdown (FDR<0.05 and Log2-fold>|1.0|). Among these, many important genes were downregulated, such as *PDZK1*, *RERG*, *GPX3*, *TIMP1*, and *CDKN2C*, We also observed a mild, but significant induction of *JUNB* upon *RDBP* knockout in the T47D cell data. Pathway analysis of differentially expressed genes showed enrichment in "DNA replication" and "p53 signaling pathway", "WNT signaling", "cell cycle", "homologous recombination", "mismatch repair", "nucleotide excision repair", "Integrin signaling", "inflammation mediated by chemokine and cytokine signaling", and "FAS signaling" pathways.

Using previously available gene expression data, we found decreased expression of *PDZK1* (PDZ domain containing 1), *RERG* (Ras-like, estrogen-regulated, growth-inhibitor), and *GPX3* (glutathione peroxidase 3) genes in metastatic PPGL. Unfortunately, we could not evaluate *RDBP* expression in this dataset as this gene was not represented in the gene expression array.

5. DISCUSSION

5.1. Part 1. MicroRNA expression in PPGL

During the execution of this study, three miRNA expression profiling studies in PPGL were published [121-123]. Meyer-Rochow and coworkers analyzed miRNA expression in a cohort of 12 malignant and 12 benign PPGL [121]. In this study, miR-483-5p, as well as its host gene (*IGF2*), was upregulated in malignant tumors, while loss of miR-15a and miR-16 was reported in malignant PPGLs [121]. In another study, Tombol et al. investigated miRNA expression in *VHL* mutant, *RET* mutant, *NF1* mutant, sporadic benign, and sporadic recurring tumors, totaling 21 samples [122]. Latter, Patterson and colleges studied miRNA expression in 69 tumors containing 12 *SDHB*, 9 *RET*, 1 *VHL*, and 1 *NF1* mutants [123].

Although miRNA expression in some genetic groups of PPGLs have been investigated in small sample sizes of tumors, miRNA expression has not been thoroughly studied and remains to be characterized in other genetic groups of PPGLs. The availability of a large and well characterized cohort of tumors of diverse genetic background and normal adrenal medulla tissues allowed us to identify not only miRNAs specific to PPGL genetic background, but also microRNAs commonly deregulated among all PPGLs. To verify our miRNA expression profiles we selected and validated eight miRNAs in an independent series of paraffin embedded PPGLs by RT-qPCR, which demonstrated their utility as molecular markers.

5.1.1. PPGLs classified according to miRNA expression

Global miRNA expression profiling was performed in a large series of PPGLs with diverse genetic backgrounds. Unsupervised hierarchical cluster analysis of miRNA expression levels classified PPGL specimens into two main clusters: cluster 1 containing *VHL*/*SDHB*/*SDHD*/nAM samples and cluster 2 with *RET*/*NF1*/*MAX*/*TMEM127* tumors. Our findings demonstrate that miRNA expression profiles are capable of classifying PPGL specimens into different tumor subgroups according to genetic background with equal or better accuracy than previous studies with mRNA expression profiles.

5.1.2. miRNA as markers in PPGL

We identified miRNAs specific to PPGL genetic background (Figure 4.1.2.). Of our reduced list of candidates, eight miRNAs specific to or common among genetic group(s) were validated in this study. Among them, upregulation of miR-885-5p and miR-488 was unique to *RET*-related PPGLs; the former miRNA was also described by Tombol et al (2010) as a *RET*-specific and reported to suppress cell migration through modulation of focal adhesion activity [122,176]. In neuroblastoma, miR-885-5p has been reported as a tumor suppressor gene, which targets cyclin-dependent kinase 2 (*CDK2*) and mini-chromosome maintenance protein 5 (*MCM5*) [177]. Although further studies are necessary to determine the precise roles played by these miRNAs in these tumors, it is

clear that upregulation of miR-488 and miR-885-5p is *RET* specific and could in part explain their relatively benign nature.

Upregulation of miR-133b, whose function appears to be cell-type specific, was confirmed as unique to VHL-related PPGLs. It has been reported that this miRNA targets PITX3 to regulate the maturation and function in midbrain dopaminergic neurons, while it suppresses BMP2-induced osteogenesis by targeting runt-related transcription factor 2 (*RUNX2)* [178,179]. Moreover, its downregulation promoted tumorigenesis in esophageal squamous cell carcinoma and colorectal cancer by targeting fascin homolog 1 (*FSCN1*) [180]. Thus, it is difficult to speculate as to whether miR-133b functions as an oncogene or a tumor suppressor gene in *VHL*-related PPGLs, and further studies are warranted to determine its role in the context of these tumor cells.

5.1.3. *VHL* and *SDHB* tumors overexpress pseudohypoxic miRNA

MicroRNA-210 was found robustly and moderately upregulated in *VHL*- and *SDHB*-related PPGLs, respectively. Overexpression of miR-210 has been described in many hypoxic tumors [181-183], such that its upregulation in *VHL* and *SDHB* mutant PPGLs was not surprising given their pseudohypoxic gene signature [32,102,103,106,184,185]. miR-210 modulates the cellular hypoxic response through a wide range of actions. Its promoter contains a functioning hypoxia response element, recognized by HIF1α, which induces its transcription upon exposure to hypoxia [182]. The higher expression of miR-210 in *VHL*- vs. *SDHB*-associated PPGLs reported here is also consistent with our previous mRNA expression profiling results [102], which indicated a predominant stabilization of HIF1α in *VHL*- compared with *SDHB*-related PPGLs, as reflected by the more robust induction of HIF1α target genes, including miR-210 in the former.

5.1.4. *SDHB*-specific miR-183/96 facilitate escape from neuronal apoptosis

In addition to miR-183, which was recently reported in PPGLs [123], we also identified robust Overexpression of miR-96 uniquely in *SDHB*-associated tumors. Previously, Vohwinkel et al. reported that high CO2 levels induced miR-183 and observed a decrease in IDH2 mRNA and protein, but the miR-183-IDH2 interaction was not conclusively confirmed [186]. Although the exact role of IDH1/2 in tumorigenesis is unclear, these enzymes convert isocitrate to α-ketoglutarate, which is a citrate acid cycle metabolite and a cofactor for more than 60 enzymes, known as 2-oxoglutarate (2-OG)-dependent dioxygenases, including EGL-Nine (EGLN) homologs [185,187]. *IDH1/2* mutations decrease availability of 2-OG resulting in both altered cellular metabolism and inhibition of enzymes that require it as a cofactor [185,187]. Taking into account the fundamental role of EGLN3 in mediating neuronal apoptosis during normal development [18,74] and that succinate accumulation due to an *SDHB* mutation competitively inhibits EGLN3 activity [18,74,185], we suggest that miR-183 overexpression in *SDHB*-related PPGLs could further contribute to EGLN3 inhibition, by downregulating *IDH2* and thus decreasing α-ketoglutarate availability, in agreement with the recent findings reported by Tanaka et al. in glioma cells [188].

5.1.5. Differential expression of miRNAs in *MAX* tumors

Two miRNAs, miR-137 and miR-382 were overexpressed in most PPGLs, and therefore can be regarded as general PPGL markers. In *MAX*-associated tumors, however, these two miRNAs were downregulated, thus suggesting that *MAX* mutations could result in distinct alterations of miRNA expression in comparison to other PPGL genetic groups. MiRNA-137 has been described to modulate differentiation, maturation, and proliferation of neurons by targeting several genes, such as RUNX2 and histone H3 Lys4 demethylase (*KDM5B*) [189]. In osteosarcoma cells, miR-382 has been shown to induce both differentiation followed by apoptosis and loss of epithelial characteristics in renal cells [190,191]. Interestingly, the *c-MYC* (*MYC)* oncogene is among the validated miR-382 targets [190], this might be relevant as the product of the *MAX* gene forms part of the c-MYC transcriptional network.

5.1.6. Closing remarks

In summary, we have demonstrated that miRNA expression in PPGL is strongly influenced by genetic background. PPGLs were grouped into two clusters according to their miRNA signatures: one was enriched in SDHB/*SDHD*/*VHL*-related tumors, while the other contained *RET*/*NF1*/*TMEM127*/*MAX*- related tumors, in accordance with the results obtained for previous mRNA transcriptional profiling studies [102,103,105,106]. In addition, it was possible to identify and validate several miRNAs associated with the primary mutation, as well as miRNAs common among PPGLs, which could be used to guide genetic study.

5.2. Part 2. Integration of miRNA-mRNA expression

MicroRNAs play critical roles in regulating various biological processes, as well as in tumor pathogenesis [192]. It is estimated that one third of all metazoan protein-coding genes are subject to regulation by miRNAs. miRNAs bind to semi-complimentary sites at the 3'-UTR of targeted mRNA, which can result in transcript degradation and/or translational truncation [60,116], and thus can affect gene expression. One miRNA can target several genes [116]. Therefore, deregulation of relatively few miRNAs could have global consequences.

After having characterized miRNA expression in PPGLs, the second objective of this study focused on investigating potential biological implications of aberrant miRNA expression in these tumors. Integration of matched miRNA and mRNA expression profiles identified miRNA-regulated gene expression networks that may contribute to PPGL pathogenesis. These results indicated that miR-183 and miR-96, which we previously validated as *SDHB*-specific miRNAs, could affect neuronal/neuroendocrine-like differentiation [174]. To test this hypothesis, a series of experiments were designed and performed, including functional studies in PC12 cells and proteomic analyses of *SDHB*- and *MAX*-related tumors.

5.2.1. Integration reveals possible roles in neuronal differentiation

Clustering of miRNA genes is common within the genome, with 38% of known miRNA genes residing in clusters [193]. Previously, our profiling data showed deregulation of several miRNA clusters, miR-193b/365 (chromosome 16p13.12), miR-183/96 (on chromosome 7q32.2), and DLK1/MEG3 miRNA cluster (chromosome 14q32.2) in all PPGLs, and *SDHB*- and *MAX*-associated tumors respectively. Evolutionary conservation of clustered miRNA genes suggests an important common biological function, co-regulating identical targets or components in the same pathway [194]. In fact, several miRNAs mapping to 14q32.2 were predicted to target the same target genes. Loss of expression of this miRNA cluster or other genes in close proximity has been previously reported in PPGL, as well as other cancers [190,195]. In osteosarcoma, downregulation of 14q32.2 miRNAs stabilizes *c-MYC*, facilitates escape from developmental apoptosis, and sustains tumorigenesis [190]. Altogether, this suggests that loss of expression of miRNAs clustered at 14q32.2 further deregulates the MYC network in which MAX forms part, and likely contributes to *MAX*-related PPGL development.

Commonly deregulated miRNAs in PPGLs showed enrichment in pathways implicated in neuronal and neuroendocrine-like differentiation. As shown in Supplementary Table 4.1.3, the "breast cancer regulation by STMN1" pathway was among those potentially regulated by common differentially expressed miRNAs in PPGLs. Our results predicted *STMN1* as a potential miR-193b target, and in fact, this regulatory interaction was recently confirmed [196]. High *STMN1* expression has been described in the developing nervous system and shown to play a role in axonal elongation and neuronal regeneration [197]. Furthermore, *STMN1* overexpression was previously reported in malignant PPGLs [198]. Although we observed an inverse correlation between miR-193b and *STMN1* expression, it was not possible to assess a potential relationship between miR-193b,

STMN1, and malignancy because our series lacked sufficient numbers of malignant tumors. IPA analysis of the commonly downregulated miRNAs also showed enrichment in "CREB signaling in neurons" and "ERK5 (MAPK7) signaling" pathways. In response to factors that elevate intracellular cAMP or Ca^{2+} levels, CREB signaling has been shown to mediate survival, proliferation, and glucose metabolism [199]. In PC12 cells, EGF and NGF have been shown to activate MAPK7 that in turn stabilizes tyrosine hydroxylase (TH) and promotes survival [200].

Although the miRNA signature associated with each of PPGL genetic group differed, there was some overlap between significantly enriched pathways. In this regards, in agreement with current knowledge about gene signature associated with cluster 2 tumors, containing *RET*-, *NF1*-, *TMEM127*-, and *MAX*-related PPGLs [201], we observed common enrichment of predicted miRNA-regulated pathways related to PI3K/AKT, RAS, and mTOR signaling.

5.2.2. miR183/96 interfering with NGF-induced differentiation

Here, we provide evidence that *SDHB*-specific miRNAs, miR-183 and/or miR-96, contribute to tumorigenesis in PPGLs by interfering with neuronal differentiation upon stimulation with NGF. In cells capable of neuronal differentiation, such as PC12 cell, stimulation with NGF initiates a signal cascade that culminates in the transcriptional activation/repression of targets, as well as post-translational modification of the activity for already present proteins [202]. According to our results, the overexpression of miR-183 and/or miR-96 in PC12 cells possibly downregulates NFG-induced genes necessary for neuronal differentiation. In this regard, Weeraratne et al. showed reduced viability and migration in medulloblastoma cells after miR-183 and miR-96 knockdown [203]. These cells acquired a more flattened appearance with projections indicative of neurite outgrowth, as well as presented an increased proneuronal gene expression signature [203].

Furthermore, our results also suggested that miR-183 and miR-96 may target the same or similar genes, as cotransfection of both miRNAs did not produce an additive or synergistic effect in cellular length, border length, and roundness as individual miR-183 or miR-96 transfections. These results were in agreement with our integration analysis, through which we identified numerous potential miR-183/96 targets with reported involvement in neuronal differentiation. For instance, *CTDSP1*, an inversely correlated potential miR-183 target, has been shown to be involved in silencing neuronal genes through interaction with REST/NRSF [204]. Also, *CTDSP1* inactivation was found to promote neuronal differentiation of P19 stem cells [204]. On the other hand, knockdown of *ARHGAP18*, a potential miR-183 target, enhanced stress fiber formation and induced rounding of cells [205]. Likewise, potential miR-96 target genes included *FARP1* and *LGI1*. *FARP1* that has been described to promote dendritic growth of spinal motor neurons subtypes [206], while *LGI1* that has been implicated in the formation, differentiation, maintenance, and plasticity of neuronal synapses [207]. Altogether, these experimental evidences are consistent with our results showing that upregulation of miR-183 and miR-96 would have a negative effect on neuronal differentiation.

5.2.3. Proteomic analysis

Label-free proteomic profiling was performed in two *SDHB*- and two *MAX*- related PPGLs. These proteomic analyses allowed us to evaluate the robustness of our miRNA–mRNA integration, as well as assess possible modes of post-transcriptional regulation by miRNAs. Our results indicated that miRNA-mediated regulation of gene expression occurs through mRNA degradation rather than translational truncation, at least in PPGL.

Approximately 11% of predicted miRNA–mRNA interactions were confirmed at the protein level. This low proportion could be due to an inherent bias of mass spectrometry detection toward most abundant proteins. As we focused on miRNAs that were generally upregulated in one experimental group relative to the other, their corresponding targets would have lower levels of expression at both mRNA and protein levels.

Nevertheless, we confirmed the predicted miR-183/96 interaction with *EZR* mRNA at the protein level. This is highly relevant given that EZR together with radixin and/or moesin form ERM complexes that connect actin to other membrane proteins [208]. Sperka et al. showed that activation of RAS required the essential participation of ERM complexes and actin, and that disrupting either the interaction of the ERM proteins with coreceptors or by downregulation of ERM proteins abolished growth factor-induced RAS activation [208]. The NGF-induced neuronal differentiation initiates a signal cascade requiring activation of RAS signaling, and interfering with the activity or function of RAS has been shown to impede or abolish NGF-induced differentiation [208,209]. Taken altogether, disruption of RAS signaling by downregulation of *EZR* by miR-183 and/or miR-96 could in part explain our results showing that these miRNAs impede NGF-induced differentiation in PC12 cells. Thus, aberrant upregulation of miR-183 and miR-96 in *SDHB*-related PPGLs could contribute to their resistance to the process of differentiation and developmental apoptosis that occurs naturally as sympathoadrenal precursors mature and acquire a chromaffin or sympathetic neuron phenotype.

5.2.4. Closing remarks

In summary, through integration with matched mRNA profiles, we found a number of potentially miRNA-regulated pathways involved in neuronal differentiation that may contribute to the development of these tumors. Functional assays showed that miR-183 and/or miR-96 overexpression impeded neuronal differentiation of PC12 cells in the presence of NGF, and global proteomic analysis suggested that this could be due to in part by disruption of growth factor-induced RAS activation.

5.3. Part 3. Chromosomal aberrations in PPGL

Since the discovery of the Philadelphia chromosome in chronic myelogenous leukemia by Peter Nowell and David Hungerford in 1961 [210], hundreds of different genetic alterations have been identified and described in human malignancies. Human malignancies show a diversity of genetic alterations, ranging from chromosome-scale lesions, such as translocations, gain, and losses of large chromosomal segments, to small nucleotide substitutions, insertions, and deletions. Now it has been well established that genetic alterations are central to the development of cancers, determining their biological or clinical behaviors. In fact, some genetic lesions are highly specific to particular disease types or closely linked to tumor histology, while others are commonly observed in a wide spectrum of cancer types, indicating more general roles of these genetic changes in tumorigenesis.

Previously, numerous studies have investigated chromosomal alterations in PPGL using numerous techniques ranging from LOH typing and conventional comparative genomic hybridization (CGH) to high-resolution array-CGH (A-CGH) [128,211,212]. Although much has been learned from those early studies, the constant evolution of our understanding of PPGL has fueled novel questions that those studies never addressed. The majority of cytogenetic data in PPGL has dealt with *VHL* and *RET* mutant tumors, seemingly *sporadic* cases, and benign and malignant tumors. The last comprehensive update of chromosomal aberrations in genetic groups of PPGL was in 2004 by Hensen et al., describing chromosomal alterations in *SDHC*/*D*/*B* mutant tumors [34]. Over the past 5 years, at least five new PPGL susceptibility genes (*TMEM127*, *MAX*, *EPAS1*, *HRAS*, *FH*) have been described and the list is expected to continue growing [55,59,63,66,213]. Consequently, nothing is known about the cytogenetics in these new genetic entities of PPGL.

This study represents the first comprehensive analysis of chromosomal alterations in a large series of PPGLs using high-density SNP genotyping arrays. In addition to *VHL*-, *RET*-, *SDHB*-, and *SDHD*-associated tumors, which have been previously studied, here we investigate chromosomal alterations in four recently described genetic groups of PPGL (*MAX*, *EPAS1*, *HRAS*, and *TMEM127* mutants). Additionally, new advancements in bioinformatics analyses of high-density SNP genotyping arrays now permit us to examine chromosomal alterations, which traditionally have been used for genome wide association studies (GWAS).

5.3.1. Benefits and pitfalls of SNP-array analysis

Here high-density SNP-array (SNP-A) genotyping has been applied for the first time to study chromosomal aberrations in PPGL. Use of high-density SNP genotyping has its benefits as well as its disadvantages over conventional high-resolution cytogenetic techniques, such as array-CGH. In terms of resolution, both SNP-A and A-CGH technologies have similar performances. Also, chromosomal losses and gains can be accurately detected by both technologies.

For copy number analysis, the relative intensities of the SNP-specific signals are compared across all SNP loci to calculate whole-genome allele-specific copy number profiles. Additionally, implementing the ASCAT algorithm, we were able to estimate the fraction of aberrant cells and the tumor ploidy for SNP-A data [139]. This has the added advantage that matched normal germline DNA is no longer necessary to study chromosomal changes in solid tumor samples, usually composed of an admixture of normal cells and aberrant cells, and frequently deviate from the diploid state.

Copy-neutral chromosomal events have recently gained interest in cancer genetics. Copy-neutral events represent an abnormal allelic status in which both of the two existing alleles have a single parental origin, and thus it is also called "uniparental disomy" or UPD. Copy neutral events are thought to occur by duplication of one allele accompanied by loss of the other. UPD has been established as one of the common mechanisms for biallelic inactivation of tumor-suppressor gene, by which the intact allele is lost and replaced by the mutant allele. Recent evidences suggest that a UPD may accompany not only loss-of-function of tumor suppressor genes but also gain-of-function of oncogenes [64,214].

However, disadvantages to application of A-SNP technology to study chromosomal alterations arise as a result of the above benefits. The amount of data produced from SNP-A is rather large, which becomes tedious when analyzing large numbers of samples. Besides more data, the addition of copy neutral variations to conventional chromosomal gains and losses adds another dimension, further complicates matters. These factors should be taken into account when considering whether to use one technology or the other.

5.3.2. Cytogenetic landscape in PPGL

Our results indicated that PPGL samples generally a ploidy less than 2.0, which represented 69% of tumors. This is consistent with data from other studies reporting for the most part chromosomal losses in these tumors [127]. *EPAS1* mutant tumors were an exception, as these groups had an average ploidy of 2.64.

We were also able to assess PPGL tumor composition, as the estimated aberrant cell fraction. The aberrant cell fraction, calculated by the ASCAT algorithm showed that on average our tumors contained a median of 27% normal cells. These values are consistent with the histopathological assessment conducted prior to this study, which qualifying the tumors as containing at least 80% tumor cells. Interestingly, *SDHD*-related PPGLs showed substantially lower aberrant cell fractions (mean 36%). It is possible that *SDHD*-associated PPGLs, which generally occur in the head and neck region, have different composition than their abdominal/thoracic and adrenal counterparts. Unfortunately, the only head and neck tumors included in this study had mutations in the *SDHD* gene, and thus we could not explore this possibility. Further studies are warranted to determine if there is an "origin of tumor" effect in PPGLs of different anatomical locations.

5.3.3. Chromosomal alterations in PPGL

We and others found a very high incidence of 1p loss in PPGL, suggesting that it might be an important event in tumorigenesis [128,211,212]. Deletions of chromosome 1p are common in several other human malignancies, including neuroblastoma, another neuroectodermally derived tumor closely related to PPGLs [215]. In this study, no tumors were found with regional losses in chromosome 1p and all had complete loss of chromosome 1p, thus we could not pinpoint any candidate regions. The high frequency of chromosome 1p loss in not only PPGL but also other tumors, supports the notion that this arm harbors one or more tumor suppressor genes. In fact, numerous candidate tumor suppressor genes mapping to 1p have been proposed, including *KIF1β* [74]. Previously, mutations in *KIF1β* have been described in PPGL [74,216]. Also, KIF1β was found to function downstream of EGLN3 to induce developmental neuronal apoptosis in chromaffin precursor cells [74].

Although loss of 1p was generally observed in our PPGLs, it was less frequent in *VHL*- and *SDHD*-associated tumors. Interestingly, it has been previously reported that loss of 1p is associated with malignant PPGL [133]. Although we lacked sufficient malignant tumors to make an assessment, we did observe loss of 1p in almost all SDHB-related tumors. As the *SDHB* gene is located at chromosome 1p36, somatic loss of chromosome 1p in *SDHB*-associated tumors would result in loss of the remaining WT *SDHB* allele. Now it is well known that *SDHB* mutant PPGLs present a higher risk to develop metastasis. Thus, the previously reported association between loss of 1p and malignancy could actually represent the frequent loss of 1p in *SDHB*-related tumors that are also more metastatic.

In most cases, loss of 1p was accompanied by loss of 3q, which occurred in 71% of all cases. Loss of chromosome 3q was the second most common chromosomal alteration, present in 51% of tumors. Present in 87% and 88% of tumors, it was worthy to note that concurrent loss of chromosomes 1p and 3q was associated with *RET* and *NF1* mutant tumors, respectively. While *SDHB*-associated tumors showed loss of 1p, they rarely showed concurrent loss of 3q.

Apart from the large group of PPGLs displaying concurrent loss of 1p and 3q, a smaller group of tumors was characterized by loss of 11p. Loss of 11p was also a relatively frequent even found in 42% of tumors. Similar to the above situation, tumors with loss of 11p also showed loss of chromosome 3p. Concurrent loss of chromosome 3p and 11p was associated with *VHL*-related PPGLs. Loss of chromosome 3p in *VHL* mutant tumors is not surprising as chromosome 3p harbors the *VHL* gene.

Although loss of chromosome 17p was another frequent alteration in PPGLs affecting 29% of tumors. Loss of chromosome 17p was previously described in PPGL [217]. Interestingly, loss of chromosome 17p was associated with *RET* PPGLs, while *NF1* mutant tumors showed loss of chromosome 17q. Although not surprising, this was significant as chromosome 17q contains the *NF1* gene. Burnichon et al. reported frequent loss of 17q in "seeming sporadic" PPGLs, which were later found to have mutations in the *NF1* gene [29]. Diagnosis of *NF1*-associated PPGLs is usually

determined clinically. *NF1* screening is not usually offered by diagnostic laboratories, as it is the largest gene in the human genome with 60 exons spanning over 350 kb. Thus, loss of chromosome 17q or at least the *NF1* locus at 17q11.2 might represent a cytogenetic marker for potential *NF1* mutations and thus could help guide genetic counsel [29,30,64].

In addition to losses affecting chromosomes 1p, 3p, 3q, 11p, and 17p, we observed the highest frequency of loss in chromosome 21 and 22, concerning 23% and 30% of all PPGLs, respectively. Loss of chromosomes 21 and 22 has previously been reported in PPGL with similar frequencies [126-128,133]. Loss of chromosome 21 was particularly associated with *RET* mutant tumors. Interestingly, all tumors with loss of chromosome 21 and/or 22 also showed loss of chromosome 1p.

5.3.4. Exclusive gain of chromosome 2p in *EPAS1* tumors

The only consistent chromosomal gain we observed in our *EPAS1* tumors was gain of 2p, as our lab previously reported [64]. Here we see that the three tumors (3/4) with *EPAS1* mutations had clearly visible gain of chromosome 2p on their ASCAT profiles. In that previous study, the fourth *EPAS1* tumor was found to harbor a small regional gain of 2p, containing the *EPAS1* gene, using a multiplex-PCR capable of detecting chromosomal rearrangement under the limits of detection of the SNP-array assay [64].

Unexpectedly, in that study by Comino-Mendez and colleagues (2013) found that the gain of 2p affected both the mutated and unmutated alleles of *EPAS1*. This was unexpected due to what is known about the genetic mechanisms behind aberrant oncogene activation. Oncogenes gain-of-function can occur as a result of activating mutations, chromosomal rearrangements, and gene amplifications. It is widely accepted that gain-of-function of a single copy of an oncogene is sufficient to deregulate cellular growth, but some examples of copy number variation at an oncogene locus have been described in other neoplasms, including PPGL and neuroblastoma [218]. Amplifications of the NMYC locus, which is also on chromosome 2p, have been reported in about 20% of neuroblastomas [219]. In PPGL, patients with activating mutations in *RET* could also harbor somatic loss of the wild type *RET* allele or duplication of the mutated allele [219]. Duplication of the mutated *EPAS1* allele would lead to larger amounts of constitutively stabilized EPAS1 protein, than when only a single mutated EPAS1 allele. One the other hand, somatic gain of the wild type allele in conjunction with an activating mutation in the other EPAS1 allele would also result in increased levels of EPAS1 protein. Either way, both mechanisms would lead to aberrant activation of EPAS1 signaling.

5.3.5. Chromosome 14 UPD in *MAX* tumors

Loss of chromosome 14 was detected in 15.6% of tumors. However, only MAX mutant specimens presented UPD of chromosome 14. Our data suggest this event occurs early in MAX tumors, as UPD of chromosome 14 was present in all these cases. Previously we reported complete loss expression of the imprinted MEG3/DLK1 miRNA cluster located at 14q32 [174].. Loss of imprinting of the 14q32 locus has previously been described in neuroblastomas (25%), Wilms' tumors (2.5%),

and PPGLs (10%) [195]. In that study, Astuti and colleges attributed loss of imprinting at the 14q32 locus to aberrant hypermethylation, as allelic loss excluded in these tumors [195]. Notwithstanding, it appears that the loss of imprinting at 14q32 region, either by aberrant hypermethylation or chromosomal alterations, suggest this event could be important for tumorigenesis in some PPGLs, especially for MAX-associated tumors. Interestingly, chromosome 14 also houses the MAX gene, but it is currently unknown the exact role UPD of chromosome 14 plays in the development of these tumors.

5.3.6. Closing remarks

Here we demonstrate the usefulness of SNP-array technology in analyzing chromosomal alterations in PPGL, which enabled us to detect copy neutral events. In this regard, we reported uniparental disomy of chromosome 14 specifically in MAX-related tumors. We integrated miRNA, mRNA, SNP-array, and methylation data to obtain a complete prospective of the molecular events at chromosome 14 in MAX mutant tumors. Decreased expression of the MEG3 gene and 14q32.2 miRNA cluster, as well as loss of unmethylated allele of the MEG3 promoter, provide evidence showing loss of the maternal (unmethylated MEG3 allele) copy of chromosome 14, as well as confirm SNP-array analysis results showing copy neutral loss of chromosome 14.

5.4. Part 4. DNA methylation patterns PPGL

DNA methylation patterns are involved in long-term gene expression programming of cell-type identity and thus, provide a novel reservoir to hunt for possible prognostic markers. DNA methylation patterns have already proven valuable as prognostic markers in other neoplasms, such as colon, breast, and ovarian cancers. Therefore, it is reasonable to consider that PPGLs with metastasis might have a unique profile of DNA methylation that not only differentiates them from those without metastasis, but also could predict clinical outcome. Early attempts to discover PPGL malignancy associated DNA methylation markers focused on a short list of candidate genes, generally hypermethylation of tumor suppressor genes [220,221]. Now, whole genome DNA methylation patterns can be interrogated using high-throughput technologies. In fact, global DNA hypermethylation was recently described in *SDHx*-related PPGLs caused by Krebs cycle dysfunction [66,222]. However, the data so far are limited and the prognostic value of these DNA methylation signatures is unclear.

Thus the fourth and final objective of this study was to characterize DNA methylation in a large series of genetically diverse PPGLs (n=123) that was also enriched with malignant tumors (n=24). DNA methylation was investigated in several PPGL genetic groups (*VHL*, *SDHB*, *SDHD*, *EPAS1*, *RET*, *NF1*, *MAX*, and *HRAS*), as well as in malignant tumors. We identified numerous malignancy associated CpGs and validated a number of them in an independent series of 154 PPGLs. Bioinformatics analyses suggested that aberrantly methylated CpGs in malignant PPGLs could possibly affect transcriptional regulation at RNA polymerase II promoters and nervous system development. Finally, hypermethylation of *RDBP*, whose protein product has functions in transcriptional regulation, was further validated in another independent series of FFPE samples by pyrosequencing.

5.4.1. PPGL genetic background affects DNA methylation

In the present work, whole-genome DNA methylation profiles were obtained using the 27K platform (Illumina). Although the newer 450K platform has replaced the 27K platform, evidences indicate that in terms of general performance both produce consistent and comparable results as demonstrated by Letouzé and coworkers [66]. Our results verified that DNA methylation patterns in PPGL are strongly influenced by genetic background, exemplified by unsupervised hierarchical cluster analysis showing two main clusters: a "pseudohypoxic" cluster (*VHL*, *SDHx*, and *EPAS1*) and the other containing classical "cluster 2" PPGLs (*RET*, *NF1*, *TMEM127*, and *MAX*). In addition, unsupervised analysis of DNA methylation profiles proved capable of differentiating *SDHx* mutant PPGLs from *VHL*/*EPAS1*- and *RET*/*NF1*/*MAX*-associated tumors. However, hierarchical cluster

analysis of DNA methylation profiles was unable to further differentiate the cluster 2 samples. As expected the two *HRAS*-related tumors included in the DS were grouped along with the other cluster 2 tumors. This was not surprising as *HRAS*-related PPGLs and the classical cluster 2 tumors (*RET*, *NF1*, *TMEM127*, and *MAX*) converge on a common molecular mechanism characterized by aberrant regulation of MAPK signaling.

5.4.2. *SDHx* PPGLs have high-CIMP

PPGL experimental groups showed varying levels of global DNA methylation. This difference was highly significant ($p<0.0001$). Tumors with *SDHB* mutations had the highest levels of DNA methylation, while *RET*-, *NF1*-, *TMEM127*-, and *MAX*-related PPGLs showed the lowest levels. *VHL*- and *EPAS1*-related tumors had intermediate levels of global DNA methylation with *EPAS1*-related PPGLs having slightly higher levels than *VHL* mutants. Our results showed that the vast majority of CpGs in *SDHB*-related PPGLs were hypermethylated, and verifies previous reports suggesting these tumors displayed a high-CIMP [66,222]. A wide variety of human neoplasms, including glioblastoma, neuroblastoma, and hematopoietic malignancies, have been described with high-CIMP [223-225]. Prognosis associated with high-CIMP depends on the cell type involved. In glioblastoma and pediatric T-cell acute lymphoblastic leukemia, a high-CIMP is associated with a more favorable prognosis, while poor prognosis has been reported for neuroblastoma and PPGL [66,223-225]. *SDHx* mutant PPGLs, in particular *SDHB*-related specimens have a high risk to develop metastatic disease relative to other genetic groups [47,226]. Similarly, *FH* mutations were recently described as having a high risk of developing metastatic disease [67]. The Letouzé et al. study was conducted with 14 malignant specimens of whom one had an *FH* mutation and six a mutation in *SDHB*. *FH* mutations, similar to those in the *SDHx* and isocitrate dehydrogenase genes, lead to global hypermethylation due to inhibition of alpha-ketoglutarate-dependent dioxygenases, including histone demethylases and TET 5-methylcytosine dioxygenases, caused by severe metabolic dysfunction [66,222,227]. However, it is likely that the reported associations between poor prognosis and the hypermethylator phenotype in PPGLs are linked to the presence of *SDHB* and *FH* mutations, as mutations in these genes are in themselves associated with poor clinical outcome. Our hierarchical cluster analysis, showing malignant PPGLs distributed throughout the dendrogram, provided further evidence indicating that global hypermethylation, while undoubtedly relevant, is not necessarily sufficient to give rise to metastasis.

5.4.3. DNA methylation influences secretory phenotype

Differential methylation of the *PNMT* gene was of particular interest due to the role of this gene has as a marker of chromaffin cell differentiation and in steroid-induced catecholamine

biosynthesis [228]. We verified the findings by Letouzé and colleagues showing high-CIMP, including the hypermethylation of *PNMT*, in *SDHx*-associated PPGLs. On the other hand, intermediate methylation of PNMT in *VHL* tumors and highly hypomethylated in *RET*- and *NF1*-associated tumors were observed, highly consistent with current data about their neurochemical phenotypes [66,87,229]. However, this model does not explain why other cluster 1 tumors do not display an adrenergic phenotype, even when the *PNMT* gene is intermediately methylated. Also, this does not explain why *MAX*-associated tumors, showing *PNMT* hypomethylation levels comparable to those in *RET* and *NF1* tumors, do not display a predominantly adrenergic phenotype. In this context, Qin and colleagues provided evidence that addressed these paradoxes in other cluster 1 tumors characterized by both *EPAS1* expression and stabilization of HIF protein [87]. In that study, the authors showed that EPAS1 completely blocked effects of steroid-induced *PNMT* expression in PC12 cells [229]. Altogether this provides a rational explaining why "cluster 1" adrenal pheochromocytomas, including those without a high-CIMP phenotype (e.g., *VHL* and *EPAS1* mutants), do not or very rarely produce epinephrine, as well as the unexpected noradrenergic phenotype presented by MAX tumors.

5.4.4. *MEG3* hypermethylated verified in *MAX* tumors

Hypermethylation of *MEG3* was observed in *MAX*-related PPGLs. *MEG3* is a non-coding tumor suppressor gene located on chromosome 14q32 that has been shown to interact with p53 [230]. Down-regulation of *MEG3* in *MAX*-related PPGLs has been previously reported [59], and here we confirm that it is indeed caused by aberrant hypermethylation due to a unipaternal disomy or deletion of part of entire chromosome 14.

5.4.5. DNA methylation associated with PPGL malignancy

We identified and confirmed 52 CpGs that were differentially methylated between malignant and benign tumors. Although not selected for validation by pyrosequencing, it merits mention that the other CpGs associated with metastasic PPGL were not only identified in the DS, but also replicated in VS1. In addition, none of these were contained in the *SDHB*-related list, which suggested that these CpGs were indeed associated with malignancy and not to genetic background. Not to mention that many also showed a significant association with progression free survival even after adjusting for *SDHB* mutation.

For instance, *HDAC11* expression has been described to correlate inversely with proliferative status in non-transformed fibroblasts [231]. Also among other candidate CpGs, hypermethylation of the *RASSF1* promoter has been previously described in association with metastatic PPGL and

neuroblastoma, as well as in association with *SDHB* mutated tumors [66,220,221]. The probe described by Letouzé et al. differed from the one identified in the present study, as these CpGs mapped to different genomic loci, which explained why it was not removed from our list of candidates when we filtered for *SDHB*-associated CpGs [66].

Bioinformatics analyses indicated that these CpGs could be involved in nervous system development, as well as regulation of transcription at RNA polymerase II promoters. Initially described as an oncogene, *NTRK1* is primarily expressed in sensory and sympathetic neurons and considered a critical receptor that promotes neuronal survival in the presence of NGF. However, recent evidences indicate that NTRK1 acts as a "dependence receptor," as expression of NTRK1 in itself was described to cause cell death of neurons and that this activity was prevented by addition of NGF [232,233]. It is widely accepted that PPGL arise though a common mechanism that impedes neuronal apoptosis of sympathoadrenal precursors when NGF becomes limiting, a mechanism in which NTRK1 in is involved [18]. Also described with roles in nervous system development, *CYFIP2* is a p53-inducible gene that leads to caspase activation and apoptosis [234,235]. Similarly, CYFIP2 also has been shown to negatively modulate cellular survival of colon cancer cells [236]. Epigenetic inactivation of *SPOCK2* gene is involved in the malignant transformation of ovarian endometriosis [237] [238]. Interestingly, PYGO1 and BCL9L, hypermethylated in PPGL presenting metastasis, participate in the nuclear beta-catenin/TCF complex. In beta-catenin/TCF complex, its composition of transactivators, like BCL9L, PYGO1, and PYGO2, mediates its activity and target gene specificity to effect fundamental patterning processes, involving reciprocal epithelial-mesenchymal interactions during tumorigenesis and normal development (e.g. nervous system development) [239]. The inverse relationship between proliferation and differentiation is well known, and intimately involved in PPGL development. Thus, the collective disruption of these factors by aberrant DNA methylation may contribute to PPGL malignancy by impairing numerous aspects of nervous system development, such as migration, cellular identity, and differentiation.

Interestingly, we observed methylation of numerous regulators of transcription in PPGLs showing metastasis. In fact, the difference in *RDBP* methylation in metastatic PPGLs was rather large (31.1%) as shown by bisulfite pyrosequencing, which indicated its potential diagnostic utility in the clinical setting. The *RDBP* gene (also known as *NELFE*) encodes the smallest subunit (subunit E) of the NELF (negative elongation factor) complex. Composed of 5 subunits (A, B, C, D, and E), the NELF complex that induces transcriptional pausing by cooperative binding to elongating RNAPII[240,241]. RNA polymerase pausing at promoters represents an important mechanism in transcriptional regulation of many genes, including JUNB [242]. Recognized as a key player in neuronal apoptosis as a C-JUN antagonist, depletion of *RDBP* by RNAi has been described to

enhance *JUNB* expression in human liver cancer cells [18,242]. From T47D breast cancer cells upon RDBP silencing helped us to identify potential RDBP target genes, including *JUNB.* Besides its involvement in neuronal apoptosis, JUNB has also been reported to increase the invasive and angiogenic potential in numerous tumors, such as renal cell carcinoma, by inducing *MMP-2/9* [243]. *RDBP* knockout decreased the expression of *TIMP1*, which was shown to suppress invasion and metastasis in various human tumors through inhibition of MMP-2/9 [244]. Another RDBP target gene identified in the T47D data, *CDKN2C* has been described as a tumor suppressor involved in PPGL and medullary thyroid carcinoma development [245].

Although it was not possible to integrate the gene expression and DNA methylation data due to the low numbers of metastatic PPGLs common in both the gene expression and DNA methylation datasets, we were able to observe downregulation of three genes (*PDZK1*, *RERG*, and *GPX3*) both in the T47D data after RDBP KO and in metastatic PPGL from previously gene expression data. This suggests that the expression of these three genes may also represent potential markers for metastatic PPGLs. GPX3 silencing has been reported metastatic tumors, such as in gastric carcinomas, where it increased cellular migration and impaired mechanisms regulating reactive oxygen species [246]. RERG was reported as a prognostic marker in breast cancer, whose expression correlated inversely proliferation, patient survival, and development of distant metastasis [247]. It has been reported that PDZK1 forms a complex between linking somatostatin receptors and phospholipase C-β (PLC-β), necessary for the specific activation of PLC-β3 and subsequent physiologic responses by somatostatins [248]. Although further studies are warranted, epigenetic silencing of *RDBP* may contribute to PPGL malignancy by causing global changes in chromatin and/or gene transcription, possibly affecting the expression of genes (e.g. *JUNB*, *PDZK1*, *RERG*, *GPX3*) not only involved with cellular response to apoptotic stimuli, but also those involved with invasion, proliferation, and metabolism.

5.4.6. Closing remarks

In conclusion, this is the first high-throughput study to explore DNA methylation patterns in the context metastatic PPGL, as well as in PPGLs with diverse genetic backgrounds. Here we demonstrate that DNA methylation patterns differ according to PPGL genotype, and verify previous data showing that *SDHx*-related tumors have global hypermethylation. Also, our results indicate that PPGLs presenting metastasis are not necessarily associated with the hypermethylator phenotype previously described in relation to SDHx/FH mutations. Most importantly, we identified and validated 52 CpGs associated with the development of metastasis in two large, independent cohorts of these rare tumors. Aberrant methylation of these CpGs

could make tumor cells less sensitive to the effect of proapoptotic signals and it warrants further investigation. Of these, forty-eight CpGs showed significant associations with progression free survival. Our bioinformatics analyses and previous experimental evidences suggest that nervous system development and transcriptional regulation could be affected by aberrant methylation of these CpGs in malignant PPGLs. Finally, *RDBP* hypermethylation was further confirmed in malignant PPGL by pyrosequencing in an independent series of FFPE archival samples and should be assessed as a new prognostic marker of malignancy for PPGL.

6. CONCLUSIONS

CONCLUSIONES in English

1. We demonstrated that miRNA expression in PPGL is strongly influenced by genetic background. PPGLs were grouped into two clusters according to their miRNA signatures: one was enriched in *SDHB*/*SDHD*/*VHL*-related tumors, while the other contained *RET*/*NF1*/*TMEM127*/*MAX*- related tumors.

2. Differential expression analysis of microRNA between various genetic entities of these tumors and normal adrenal medulla allowed us miRNAs specific to genetic background, as well as those commonly deregulated among all PPGLs. Those specific ones could be used to guide genetic study and the common ones may also offer novel targets for therapeutic intervention.

3. Integration of matched global miRNA and mRNA profiles identified miRNA-regulated pathways, being neuronal differentiation a common theme among PPGLs with different genetic background.

4. *SDHB*-specific miRNAs, miRNA-183 and miRNA-96, contribute to PPGL tumorigenesis by antagonizing neuronal differentiation by NGF stimulation in a rat pheochromocytoma cellular model (PC12). This effect could in part be due to disruption of growth factor-induced RAS activation, according to our results from proteomic analyses.

5. Global proteomic analysis suggested that miRNA-mediated regulation of gene expression proceeded predominately through target transcript degradation, rather than through translational truncation.

6. The use of the SNP-array technology detected a subgroup of PPGLs displaying uniparental disomy at chromosome 14 specific to *MAX*-related tumors. Integration of miRNA, mRNA, SNP-array, and methylation data provided a detailed portrait of the molecular events occurring at chromosome 14 in *MAX* mutant tumors. Decreased expression of the *MEG3* gene and 14q32.2 miRNA cluster, as well as loss of unmethylated allele of the *MEG3* promoter, provide evidence showing loss of the maternal (unmethylated *MEG3* allele) copy of chromosome 14, as well as confirm SNP-array analysis results showing copy neutral loss of chromosome 14.

7. Our results demonstrate that DNA methylation patterns differ according to PPGL genotype, and verify previous data showing that *SDHx*-related tumors have global hypermethylation.

8. PPGL presenting metastasis are not necessarily associated with hypermethylator phenotype described previously in relation to *SDHx*/*FH*-associated tumors. In fact, we identified and validated 52 CpGs associated with the development of metastasis in two large and independent cohorts of these rare tumors. Of these, forty-eight CpGs showed significant associations with progression free survival. All together suggested that these CpGs could be utilized as predictors of metastatic potential in PPGL

9. *RDBP* hypermethylation may contribute to PPGL malignancy by disrupting gene expression networks involved not only in cellular response to but also those promoting migration, invasion, and neoangiogenesis.

CONCLUSIONES en Español

1. Hemos demostrado que la expresión de miRNA en PPGL está fuertemente influenciada por los antecedentes genéticos. PPGLs se agruparon en dos grupos según sus firmas de miRNA: uno contenía los tumores relacionados con *SDHB*/*SDHD*/*VHL*, mientras que el otro contenía los tumores relacionados con *RET*/*NF1*/*TMEM127*/*MAX*.

2. El análisis de la expresión diferencial de microRNA entre diversas entidades genéticas de estos tumores y la médula suprarrenal normal nos permitió identificar miRNAs específicos al perfil genético, así como aquellos desregulados comúnmente en todos los PPGLs. Aquellos específicos podrían utilizarse para guiar el estudio genético y los comunes podrían ofrecer nuevas dianas para la intervención terapéutica.

3. La integración de los perfiles de miRNA y mRNA identificó las vías reguladas por miRNA, siendo la diferenciación neuronal un tema común entre PPGLs con diferentes perfiles genéticos.

4. Los miRNAs específicos de los tumores *SDHB*, miRNA-183 y miRNA-96, contribuyen a la tumorigénesis PPGL antagonizando la diferenciación neuronal de cellulas chromafinas mediate la estimulación de NGF en un modelo celular de feocromocitoma de rata (PC12). Este efecto podría ser en parte debido a la interrupción de la activación de RAS inducida por el factor de crecimiento, según los resultados de los análisis proteómicos.

5. EL análisis proteómico global sugiere que la regulacion mediado por miRNAs en la expresión génica proviene predominantemente de la degradación de la transcripción de la diana, en lugar de truncamiento traslacional.

6. El uso de la tecnología de SNP-array detectó un subgrupo de PPGLs que mostraban disomía uniparental en el cromosoma 14 específicos para tumores relacionados con *MAX*. Integración de datos de metilación, mRNA, SNP-array y miRNA ha proporcionado un retrato detallado de los eventos moleculares que ocurren en el cromosoma 14 en tumores con mutaciones en *MAX*. La expresión disminuida del gen *MEG3* y el entero "cluster" de miRNAs localizados en 14q32.2, así como la pérdida del alelo no metilado del promotor *MEG3*, proporcionan evidencia de la pérdida materna (alelo de *MEG3* no metilado) de la copia del cromosoma 14, así como confirma los resultados del análisis de SNP-array que muestran pérdida del cromosoma 14 materna y duplicación de la copia paterna.

7. Nuestros resultados demuestran que los patrones de metilación del ADN difieren según el genotipo de los PPGL y verifican los datos anteriores que mostraban que los tumores relacionados con *SDHx* tienen una hipermetilación global.

8. Los PPGL que presentan metástasis no están necesariamente asociados con fenotipo hipermetilador descrito anteriormente en relación con los tumores *SDHx*/*FH*-asociado. De hecho, se identificaron y validaron 52 GPC asociados con el desarrollo de metástasis en dos cohortes grandes e independientes de estos tumores raros. De éstos, cuarenta y ocho CpGs mostraron asociación significativa con la supervivencia libre de progresión. Todo junto sugiere que estas CpGs podrían ser utilizadas como predictores de potencial metastático en PPGL.

9. La hipermetilación de *RDBP* puede contribuir a la malignidad de los PPGL interrumpiendo las redes de expresión génica involucradas no sólo en la respuesta celular sino también promoviendo la migración, invasión y neoangiogénesis.

7. REFERENCES

1 Baysal, B. E. Hereditary paraganglioma targets diverse paraganglia. *J Med Genet* **39**, 617-622 (2002).

2 Eisenhofer, G. *et al.* Pheochromocytoma catecholamine phenotypes and prediction of tumor size and location by use of plasma free metanephrines. *Clin Chem* **51**, 735-744, doi:clinchem.2004.045484 [pii] 10.1373/clinchem.2004.045484 (2005).

3 Maher, E. R. *et al.* Von Hippel-Lindau disease: a genetic study. *Journal of medical genetics* **28**, 443-447 (1991).

4 Latif, F. *et al.* Identification of the von Hippel-Lindau disease tumor suppressor gene. *Science* **260**, 1317-1320 (1993).

5 Maher, E. R. *et al.* Clinical features and natural history of von Hippel-Lindau disease. *Q J Med* **77**, 1151-1163 (1990).

6 Maher, E. R. *et al.* Phenotypic expression in von Hippel-Lindau disease: correlations with germline VHL gene mutations. *Journal of medical genetics* **33**, 328-332 (1996).

7 Crossey, P. A. *et al.* Identification of intragenic mutations in the von Hippel-Lindau disease tumour suppressor gene and correlation with disease phenotype. *Human molecular genetics* **3**, 1303-1308 (1994).

8 Zbar, B. *et al.* Germline mutations in the Von Hippel-Lindau disease (VHL) gene in families from North America, Europe, and Japan. *Human mutation* **8**, 348-357, doi:10.1002/(SICI)1098-1004(1996)8:4<348::AID-HUMU8>3.0.CO;2-3 (1996).

9 Richards, F. M. *et al.* Molecular analysis of de novo germline mutations in the von Hippel-Lindau disease gene. *Hum Mol Genet* **4**, 2139-2143 (1995).

10 Kaelin, W. G., Jr. Treatment of kidney cancer: insights provided by the VHL tumor-suppressor protein. *Cancer* **115**, 2262-2272, doi:10.1002/cncr.24232 (2009).

11 McNeill, A. *et al.* Genotype-phenotype correlations in VHL exon deletions. *American journal of medical genetics. Part A* **149A**, 2147-2151, doi:10.1002/ajmg.a.33023 (2009).

12 Cascon, A. *et al.* Loss of the actin regulator HSPC300 results in clear cell renal cell carcinoma protection in Von Hippel-Lindau patients. *Human mutation* **28**, 613-621, doi:10.1002/humu.20496 (2007).

13 Crossey, P. A. *et al.* Molecular genetic diagnosis of von Hippel-Lindau disease in familial phaeochromocytoma. *Journal of medical genetics* **32**, 885-886 (1995).

14 Neumann, H. P. *et al.* Consequences of direct genetic testing for germline mutations in the clinical management of families with multiple endocrine neoplasia, type II. *JAMA : the journal of the American Medical Association* **274**, 1149-1151 (1995).

15 Hoffman, M. A. *et al.* von Hippel-Lindau protein mutants linked to type 2C VHL disease preserve the ability to downregulate HIF. *Human molecular genetics* **10**, 1019-1027 (2001).

16 Ong, K. R. *et al.* Genotype-phenotype correlations in von Hippel-Lindau disease. *Hum Mutat* **28**, 143-149, doi:10.1002/humu.20385 (2007).

17 Clifford, S. C. *et al.* Contrasting effects on HIF-1alpha regulation by disease-causing pVHL mutations correlate with patterns of tumourigenesis in von Hippel-Lindau disease. *Hum Mol Genet* **10**, 1029-1038 (2001).

18 Lee, S. *et al.* Neuronal apoptosis linked to EglN3 prolyl hydroxylase and familial pheochromocytoma genes: developmental culling and cancer. *Cancer cell* **8**, 155-167, doi:10.1016/j.ccr.2005.06.015 (2005).

19 Mulligan, L. M. *et al.* Germ-line mutations of the RET proto-oncogene in multiple endocrine neoplasia type 2A. *Nature* **363**, 458-460, doi:10.1038/363458a0 (1993).

20 Durbec, P. *et al.* GDNF signalling through the Ret receptor tyrosine kinase. *Nature* **381**, 789-793, doi:10.1038/381789a0 (1996).

21 Raue, F. & Frank-Raue, K. Update multiple endocrine neoplasia type 2. *Fam Cancer* **9**, 449-457, doi:10.1007/s10689-010-9320-2 (2010).

22 Besset, V., Scott, R. P. & Ibanez, C. F. Signaling complexes and protein-protein interactions involved in the activation of the Ras and phosphatidylinositol 3-kinase pathways by the c-Ret receptor tyrosine kinase. *J Biol Chem* **275**, 39159-39166, doi:10.1074/jbc.M006908200 M006908200 [pii] (2000).

23 Quayle, F. J., Fialkowski, E. A., Benveniste, R. & Moley, J. F. Pheochromocytoma penetrance varies by RET mutation in MEN 2A. *Surgery* **142**, 800-805; discussion 805 e801, doi:S0039-6060(07)00530-2 [pii] 10.1016/j.surg.2007.09.013 (2007).

24 Boyd, K. P., Korf, B. R. & Theos, A. Neurofibromatosis type 1. *J Am Acad Dermatol* **61**, 1-14; quiz 15-16, doi:S0190-9622(09)00405-8 [pii] 10.1016/j.jaad.2008.12.051 (2009).

25 Martin, G. A. *et al.* The GAP-related domain of the neurofibromatosis type 1 gene product interacts with ras p21. *Cell* **63**, 843-849, doi:0092-8674(90)90150-D [pii] (1990).

26 Johannessen, C. M. *et al.* TORC1 is essential for NF1-associated malignancies. *Curr Biol* **18**, 56-62, doi:S0960-9822(07)02358-5 [pii] 10.1016/j.cub.2007.11.066 (2008).

27 Zinnamosca, L. *et al.* Neurofibromatosis type 1 (NF1) and pheochromocytoma: prevalence, clinical and cardiovascular aspects. *Archives of dermatological research* **303**, 317-325, doi:10.1007/s00403-010-1090-z (2011).

28 Welander, J., Soderkvist, P. & Gimm, O. The NF1 gene: a frequent mutational target in sporadic pheochromocytomas and beyond. *Endocrine-related cancer* **20**, C13-17, doi:10.1530/ERC-13-0046 (2013).

29 Burnichon, N. *et al.* Somatic NF1 inactivation is a frequent event in sporadic pheochromocytoma. *Human molecular genetics* **21**, 5397-5405, doi:10.1093/hmg/dds374 (2012).

30 Welander, J. *et al.* Integrative genomics reveals frequent somatic NF1 mutations in sporadic pheochromocytomas. *Human molecular genetics* **21**, 5406-5416, doi:10.1093/hmg/dds402 (2012).

31 Briere, J. J. *et al.* Succinate dehydrogenase deficiency in human. *Cellular and molecular life sciences : CMLS* **62**, 2317-2324, doi:10.1007/s00018-005-5237-6 (2005).

32 Baysal, B. E. *et al.* Mutations in SDHD, a mitochondrial complex II gene, in hereditary paraganglioma. *Science* **287**, 848-851 (2000).

33 Yeap, P. M. *et al.* Molecular analysis of pheochromocytoma after maternal transmission of SDHD mutation elucidates mechanism of parent-of-origin effect. *The Journal of clinical endocrinology and metabolism* **96**, E2009-2013, doi:10.1210/jc.2011-1244 (2011).

34 Hensen, E. F. *et al.* Somatic loss of maternal chromosome 11 causes parent-of-origin-dependent inheritance in SDHD-linked paraganglioma and phaeochromocytoma families. *Oncogene* **23**, 4076-4083, doi:10.1038/sj.onc.1207591 (2004).

35 Pigny, P. *et al.* Paraganglioma after maternal transmission of a succinate dehydrogenase gene mutation. *The Journal of clinical endocrinology and metabolism* **93**, 1609-1615, doi:10.1210/jc.2007-1989 (2008).

36 Benn, D. E. *et al.* Clinical presentation and penetrance of pheochromocytoma/paraganglioma syndromes. *J Clin Endocrinol Metab* **91**, 827-836, doi:jc.2005-1862 [pii] 10.1210/jc.2005-1862 (2006).

37 Ricketts, C. J. *et al.* Tumor risks and genotype-phenotype-proteotype analysis in 358 patients with germline mutations in SDHB and SDHD. *Human mutation* **31**, 41-51, doi:10.1002/humu.21136 (2010).

38 Neumann, H. P. *et al.* Distinct clinical features of paraganglioma syndromes associated with SDHB and SDHD gene mutations. *JAMA* **292**, 943-951, doi:10.1001/jama.292.8.943 292/8/943 [pii] (2004).

39 Hao, H. X. *et al.* SDH5, a gene required for flavination of succinate dehydrogenase, is mutated in paraganglioma. *Science* **325**, 1139-1142, doi:1175689 [pii] 10.1126/science.1175689 (2009).

40 Bayley, J. P. *et al.* SDHAF2 mutations in familial and sporadic paraganglioma and phaeochromocytoma. *The Lancet. Oncology* **11**, 366-372, doi:10.1016/S1470-2045(10)70007-3 (2010).

41 Casey, R. *et al.* Universal genetic screening uncovers a novel presentation of an SDHAF2 mutation. *The Journal of clinical endocrinology and metabolism* **99**, E1392-1396, doi:10.1210/jc.2013-4536 (2014).

42 Piccini, V. *et al.* Head and neck paragangliomas: genetic spectrum and clinical variability in 79 consecutive patients. *Endocrine-related cancer* **19**, 149-155, doi:10.1530/ERC-11-0369 (2012).

43 Niemann, S. & Muller, U. Mutations in SDHC cause autosomal dominant paraganglioma, type 3. *Nat Genet* **26**, 268-270, doi:10.1038/81551 (2000).

44 Bickmann, J. K. *et al.* Phenotypic variability and risk of malignancy in SDHC-linked paragangliomas: lessons from three unrelated cases with an identical germline mutation (p.Arg133*). *The Journal of clinical endocrinology and metabolism* **99**, E489-496, doi:10.1210/jc.2013-3486 (2014).

45 Peczkowska, M. *et al.* Extra-adrenal and adrenal pheochromocytomas associated with a germline SDHC mutation. *Nat Clin Pract Endocrinol Metab* **4**, 111-115, doi:ncpendmet0726 [pii] 10.1038/ncpendmet0726 (2008).

46 Astuti, D. *et al.* Gene mutations in the succinate dehydrogenase subunit SDHB cause susceptibility to familial pheochromocytoma and to familial paraganglioma. *Am J Hum Genet* **69**, 49-54, doi:S0002-9297(07)61444-X [pii] 10.1086/321282 (2001).

47 Amar, L. *et al.* Succinate dehydrogenase B gene mutations predict survival in patients with malignant pheochromocytomas or paragangliomas. *J Clin Endocrinol Metab* **92**, 3822-3828, doi:jc.2007-0709 [pii] 10.1210/jc.2007-0709 (2007).

48 van Nederveen, F. H., Korpershoek, E., Lenders, J. W., de Krijger, R. R. & Dinjens, W. N. Somatic SDHB mutation in an extraadrenal pheochromocytoma. *N Engl J Med* **357**, 306-308, doi:357/3/306 [pii] 10.1056/NEJMc070010 (2007).

49 Cascon, A. *et al.* Genetics of pheochromocytoma and paraganglioma in Spanish pediatric patients. *Endocrine-related cancer* **20**, L1-6, doi:10.1530/ERC-12-0339 (2013).

50 Schiavi, F. *et al.* Are we overestimating the penetrance of mutations in SDHB? *Human mutation* **31**, 761-762, doi:10.1002/humu.21269 (2010).

51 Horvath, R. *et al.* Leigh syndrome caused by mutations in the flavoprotein (Fp) subunit of succinate dehydrogenase (SDHA). *J Neurol Neurosurg Psychiatry* **77**, 74-76, doi:77/1/74 [pii] 10.1136/jnnp.2005.067041 (2006).

52 Burnichon, N. *et al.* SDHA is a tumor suppressor gene causing paraganglioma. *Hum Mol Genet* **19**, 3011-3020, doi:ddq206 [pii] 10.1093/hmg/ddq206 (2010).

53 Castelblanco, E. *et al.* Usefulness of negative and weak-diffuse pattern of SDHB immunostaining in assessment of SDH mutations in paragangliomas and pheochromocytomas. *Endocrine pathology* **24**, 199-205, doi:10.1007/s12022-013-9269-4 (2013).

54 Korpershoek, E. *et al.* SDHA immunohistochemistry detects germline SDHA gene mutations in apparently sporadic paragangliomas and pheochromocytomas. *The Journal of clinical endocrinology and metabolism* **96**, E1472-1476, doi:10.1210/jc.2011-1043 (2011).

55 Qin, Y. *et al.* Germline mutations in TMEM127 confer susceptibility to pheochromocytoma. *Nature genetics* **42**, 229-233, doi:10.1038/ng.533 (2010).

56 Qin, Y. *et al.* The tumor susceptibility gene TMEM127 is mutated in renal cell carcinomas and modulates endolysosomal function. *Human molecular genetics* **23**, 2428-2439, doi:10.1093/hmg/ddt638 (2014).

57 Yao, L. *et al.* Spectrum and prevalence of FP/TMEM127 gene mutations in pheochromocytomas and paragangliomas. *JAMA : the journal of the American Medical Association* **304**, 2611-2619, doi:10.1001/jama.2010.1830 (2010).

58 Neumann, H. P. *et al.* Germline mutations of the TMEM127 gene in patients with paraganglioma of head and neck and extraadrenal abdominal sites. *The Journal of clinical endocrinology and metabolism* **96**, E1279-1282, doi:10.1210/jc.2011-0114 (2011).

59 Comino-Mendez, I. *et al.* Exome sequencing identifies MAX mutations as a cause of hereditary pheochromocytoma. *Nature genetics* **43**, 663-667, doi:10.1038/ng.861 (2011).

60 Bartel, D. P. MicroRNAs: genomics, biogenesis, mechanism, and function. *Cell* **116**, 281-297 (2004).

61 Liu, Z., Sall, A. & Yang, D. MicroRNA: An emerging therapeutic target and intervention tool. *Int J Mol Sci* **9**, 978-999, doi:10.3390/ijms9060978 (2008).

62 Burnichon, N. *et al.* MAX mutations cause hereditary and sporadic pheochromocytoma and paraganglioma. *Clinical cancer research : an official journal of the American Association for Cancer Research* **18**, 2828-2837, doi:10.1158/1078-0432.CCR-12-0160 (2012).

63 Lorenzo, F. R. *et al.* A novel EPAS1/HIF2A germline mutation in a congenital polycythemia with paraganglioma. *Journal of molecular medicine* **91**, 507-512, doi:10.1007/s00109-012-0967-z (2013).

64 Comino-Mendez, I. *et al.* Tumoral EPAS1 (HIF2A) mutations explain sporadic pheochromocytoma and paraganglioma in the absence of erythrocytosis. *Human molecular genetics* **22**, 2169-2176, doi:10.1093/hmg/ddt069 (2013).

65 Toledo, R. A. *et al.* In vivo and in vitro oncogenic effects of HIF2A mutations in pheochromocytomas and paragangliomas. *Endocr Relat Cancer* **20**, 349-359, doi:ERC-13-0101 [pii] 10.1530/ERC-13-0101 (2013).

66 Letouze, E. *et al.* SDH mutations establish a hypermethylator phenotype in paraganglioma. *Cancer cell* **23**, 739-752, doi:10.1016/j.ccr.2013.04.018 (2013).

67 Castro-Vega, L. J. *et al.* Germline mutations in FH confer predisposition to malignant pheochromocytomas and paragangliomas. *Human molecular genetics* **23**, 2440-2446, doi:10.1093/hmg/ddt639 (2014).

68 Downward, J. Targeting RAS signalling pathways in cancer therapy. *Nature reviews. Cancer* **3**, 11-22, doi:10.1038/nrc969 (2003).

69 Oudijk, L. *et al.* H-RAS mutations are restricted to sporadic pheochromocytomas lacking specific clinical or pathological features: data from a multi-institutional series. *The Journal of clinical endocrinology and metabolism* **99**, E1376-1380, doi:10.1210/jc.2013-3879 (2014).

70 Raue, F. & Zink, A. Clinical features of multiple endocrine neoplasia type 1 and type 2. *Horm Res* **38 Suppl 2**, 31-35 (1992).

71 Brandi, M. L. *et al.* Guidelines for diagnosis and therapy of MEN type 1 and type 2. *J Clin Endocrinol Metab* **86**, 5658-5671 (2001).

72 Ladroue, C. *et al.* PHD2 mutation and congenital erythrocytosis with paraganglioma. *N Engl J Med* **359**, 2685-2692, doi:359/25/2685 [pii] 10.1056/NEJMoa0806277 (2008).

73 Yang, C. *et al.* Germ-line PHD1 and PHD2 mutations detected in patients with pheochromocytoma/paraganglioma-polycythemia. *Journal of molecular medicine*, doi:10.1007/s00109-014-1205-7 (2014).

74 Schlisio, S. *et al.* The kinesin KIF1Bbeta acts downstream from EglN3 to induce apoptosis and is a potential 1p36 tumor suppressor. *Genes & development* **22**, 884-893, doi:10.1101/gad.1648608 (2008).

75 Astuti, D. *et al.* Mutation analysis of HIF prolyl hydroxylases (PHD/EGLN) in individuals with features of phaeochromocytoma and renal cell carcinoma susceptibility. *Endocrine-related cancer* **18**, 73-83, doi:10.1677/ERC-10-0113 (2011).

76 Ladroue, C. *et al.* Distinct deregulation of the hypoxia inducible factor by PHD2 mutants identified in germline DNA of patients with polycythemia. *Haematologica* **97**, 9-14, doi:10.3324/haematol.2011.044644 (2012).

77 Welander, J. *et al.* Rare germline mutations identified by targeted next-generation sequencing of susceptibility genes in pheochromocytoma and paraganglioma. *The Journal of clinical endocrinology and metabolism* **99**, E1352-1360, doi:10.1210/jc.2013-4375 (2014).

78 Ham, J. *et al.* A c-Jun dominant negative mutant protects sympathetic neurons against programmed cell death. *Neuron* **14**, 927-939, doi:0896-6273(95)90331-3 [pii] (1995).

79 Schlingensiepen, K. H. *et al.* The role of Jun transcription factor expression and phosphorylation in neuronal differentiation, neuronal cell death, and plastic adaptations in vivo. *Cell Mol Neurobiol* **14**, 487-505 (1994).

80 Okuda, H. *et al.* Direct interaction of the beta-domain of VHL tumor suppressor protein with the regulatory domain of atypical PKC isotypes. *Biochem Biophys Res Commun* **263**, 491-497, doi:10.1006/bbrc.1999.1347 S0006291X99913475 [pii] (1999).

81 Kieser, A. *et al.* Protein kinase C-zeta reverts v-raf transformation of NIH-3T3 cells. *Genes Dev* **10**, 1455-1466 (1996).

82 De Vita, G. *et al.* Tyrosine 1062 of RET-MEN2A mediates activation of Akt (protein kinase B) and mitogen-activated protein kinase pathways leading to PC12 cell survival. *Cancer Res* **60**, 3727-3731 (2000).

83 Vogel, K. S., Brannan, C. I., Jenkins, N. A., Copeland, N. G. & Parada, L. F. Loss of neurofibromin results in neurotrophin-independent survival of embryonic sensory and sympathetic neurons. *Cell* **82**, 733-742, doi:0092-8674(95)90470-0 [pii] (1995).

84 Eisenhofer, G. *et al.* Plasma methoxytyramine: a novel biomarker of metastatic pheochromocytoma and paraganglioma in relation to established risk factors of tumour size, location and SDHB mutation status. *European journal of cancer* **48**, 1739-1749, doi:10.1016/j.ejca.2011.07.016 (2012).

85 Timmers, H. J. *et al.* Clinical presentations, biochemical phenotypes, and genotype-phenotype correlations in patients with succinate dehydrogenase subunit B-associated pheochromocytomas and paragangliomas. *J Clin Endocrinol Metab* **92**, 779-786, doi:jc.2006-2315 [pii] 10.1210/jc.2006-2315 (2007).

86 Eisenhofer, G. *et al.* Measurements of plasma methoxytyramine, normetanephrine, and metanephrine as discriminators of different hereditary forms of pheochromocytoma. *Clin Chem* **57**, 411-420, doi:clinchem.2010.153320 [pii] 10.1373/clinchem.2010.153320 (2011).

87 Qin, N. *et al.* Opposing effects of HIF1alpha and HIF2alpha on chromaffin cell phenotypic features and tumor cell proliferation: Insights from MYC-associated factor X. *International journal of cancer. Journal international du cancer* **135**, 2054-2064, doi:10.1002/ijc.28868 (2014).

88 Ilias, I. *et al.* Comparison of 6-18F-fluorodopamine PET with 123I-metaiodobenzylguanidine and 111in-pentetreotide scintigraphy in localization of nonmetastatic and metastatic pheochromocytoma. *J Nucl Med* **49**, 1613-1619, doi:jnumed.108.052373 [pii] 10.2967/jnumed.108.052373 (2008).

89 van der Harst, E. *et al.* [(123)I]metaiodobenzylguanidine and [(111)In]octreotide uptake in begnign and malignant pheochromocytomas. *J Clin Endocrinol Metab* **86**, 685-693 (2001).

90 Bhatia, K. S. *et al.* 123I-metaiodobenzylguanidine (MIBG) scintigraphy for the detection of adrenal and extra-adrenal phaeochromocytomas: CT and MRI correlation. *Clin Endocrinol (Oxf)* **69**, 181-188, doi:CEN3256 [pii] 10.1111/j.1365-2265.2008.03256.x (2008).

91 Eisenhofer, G. *et al.* Malignant pheochromocytoma: current status and initiatives for future progress. *Endocr Relat Cancer* **11**, 423-436 (2004).

92 Lehnert, H., Mundschenk, J. & Hahn, K. Malignant pheochromocytoma. *Front Horm Res* **31**, 155-162 (2004).

93 Chrisoulidou, A., Kaltsas, G., Ilias, I. & Grossman, A. B. The diagnosis and management of malignant phaeochromocytoma and paraganglioma. *Endocr Relat Cancer* **14**, 569-585, doi:14/3/569 [pii] 10.1677/ERC-07-0074 (2007).

94 Nomura, K. *et al.* Survival of patients with metastatic malignant pheochromocytoma and efficacy of combined cyclophosphamide, vincristine, and dacarbazine chemotherapy. *J Clin Endocrinol Metab* **94**, 2850-2856, doi:jc.2008-2697 [pii] 10.1210/jc.2008-2697 (2009).

95 Timmers, H. J. *et al.* Metastases but not cardiovascular mortality reduces life expectancy following surgical resection of apparently benign pheochromocytoma. *Endocr Relat Cancer* **15**, 1127-1133, doi:ERC-08-0049 [pii] 10.1677/ERC-08-0049 (2008).

96 Ayala-Ramirez, M. *et al.* Clinical risk factors for malignancy and overall survival in patients with pheochromocytomas and sympathetic paragangliomas: primary tumor size and primary tumor location as prognostic indicators. *J Clin Endocrinol Metab* **96**, 717-725, doi:jc.2010-1946 [pii] 10.1210/jc.2010-1946 (2011).

97 Feng, F. *et al.* Predictive factors for malignant pheochromocytoma: analysis of 136 patients. *J Urol* **185**, 1583-1590, doi:S0022-5347(10)05392-9 [pii]10.1016/j.juro.2010.12.050 (2011).

98 Zelinka, T. *et al.* Metastatic pheochromocytoma: does the size and age matter? *Eur J Clin Invest* **41**, 1121-1128, doi:10.1111/j.1365-2362.2011.02518.x (2011).

99 Linnoila, R. I., Keiser, H. R., Steinberg, S. M. & Lack, E. E. Histopathology of benign versus malignant sympathoadrenal paragangliomas: clinicopathologic study of 120 cases including unusual histologic features. *Hum Pathol* **21**, 1168-1180 (1990).

100 Thompson, L. D. Pheochromocytoma of the Adrenal gland Scaled Score (PASS) to separate benign from malignant neoplasms: a clinicopathologic and immunophenotypic study of 100 cases. *Am J Surg Pathol* **26**, 551-566 (2002).

101 Kimura, N., Watanabe, T., Noshiro, T., Shizawa, S. & Miura, Y. Histological grading of adrenal and extra-adrenal pheochromocytomas and relationship to prognosis: a clinicopathological analysis of 116 adrenal pheochromocytomas and 30 extra-adrenal sympathetic paragangliomas including 38 malignant tumors. *Endocr Pathol* **16**, 23-32, doi:EP:16:1:023 [pii] (2005).

102 Lopez-Jimenez, E. *et al.* Research resource: Transcriptional profiling reveals different pseudohypoxic signatures in SDHB and VHL-related pheochromocytomas. *Molecular endocrinology* **24**, 2382-2391, doi:10.1210/me.2010-0256 (2010).

103 Favier, J. *et al.* The Warburg effect is genetically determined in inherited pheochromocytomas. *PloS one* **4**, e7094, doi:10.1371/journal.pone.0007094 (2009).

104 Dahia, P. L. *et al.* A HIF1alpha regulatory loop links hypoxia and mitochondrial signals in pheochromocytomas. *PLoS Genet* **1**, 72-80, doi:10.1371/journal.pgen.0010008 (2005).

105 Eisenhofer, G. *et al.* Distinct gene expression profiles in norepinephrine- and epinephrine-producing hereditary and sporadic pheochromocytomas: activation of hypoxia-driven angiogenic pathways in von Hippel-Lindau syndrome. *Endocrine-related cancer* **11**, 897-911, doi:10.1677/erc.1.00838 (2004).

106 Dahia, P. L. & Familial Pheochromocytoma, C. Transcription association of VHL and SDH mutations link hypoxia and oxidoreductase signals in pheochromocytomas. *Annals of the New York Academy of Sciences* **1073**, 208-220, doi:10.1196/annals.1353.023 (2006).

107 Powers, J. F., Evinger, M. J., Zhi, J., Picard, K. L. & Tischler, A. S. Pheochromocytomas in Nf1 knockout mice express a neural progenitor gene expression profile. *Neuroscience* **147**, 928-937, doi:S0306-4522(07)00598-2 [pii] 10.1016/j.neuroscience.2007.05.008 (2007).

108 Lee, R. C., Feinbaum, R. L. & Ambros, V. The C. elegans heterochronic gene lin-4 encodes small RNAs with antisense complementarity to lin-14. *Cell* **75**, 843-854, doi:0092-8674(93)90529-Y [pii] (1993).

109 Reinhart, B. J. *et al.* The 21-nucleotide let-7 RNA regulates developmental timing in Caenorhabditis elegans. *Nature* **403**, 901-906, doi:10.1038/35002607 (2000).

110 Bartel, D. P. & Chen, C. Z. Micromanagers of gene expression: the potentially widespread influence of metazoan microRNAs. *Nat Rev Genet* **5**, 396-400, doi:10.1038/nrg1328 nrg1328 [pii] (2004).

111 Cai, X., Hagedorn, C. H. & Cullen, B. R. Human microRNAs are processed from capped, polyadenylated transcripts that can also function as mRNAs. *RNA* **10**, 1957-1966, doi:rna.7135204 [pii] 10.1261/rna.7135204 (2004).

112 Lee, Y. *et al.* MicroRNA genes are transcribed by RNA polymerase II. *EMBO J* **23**, 4051-4060, doi:10.1038/sj.emboj.7600385 7600385 [pii] (2004).

113 Bohnsack, M. T., Czaplinski, K. & Gorlich, D. Exportin 5 is a RanGTP-dependent dsRNA-binding protein that mediates nuclear export of pre-miRNAs. *RNA* **10**, 185-191 (2004).

114 Chendrimada, T. P. *et al.* TRBP recruits the Dicer complex to Ago2 for microRNA processing and gene silencing. *Nature* **436**, 740-744, doi:nature03868 [pii] 10.1038/nature03868 (2005).

115 Maroney, P. A., Yu, Y., Fisher, J. & Nilsen, T. W. Evidence that microRNAs are associated with translating messenger RNAs in human cells. *Nat Struct Mol Biol* **13**, 1102-1107, doi:nsmb1174 [pii] 10.1038/nsmb1174 (2006).

116 Lim, L. P. *et al.* Microarray analysis shows that some microRNAs downregulate large numbers of target mRNAs. *Nature* **433**, 769-773, doi:10.1038/nature03315 (2005).

117 Orom, U. A., Nielsen, F. C. & Lund, A. H. MicroRNA-10a binds the 5'UTR of ribosomal protein mRNAs and enhances their translation. *Mol Cell* **30**, 460-471, doi:S1097-2765(08)00328-6 [pii] 10.1016/j.molcel.2008.05.001 (2008).

118 Grimson, A. *et al.* MicroRNA targeting specificity in mammals: determinants beyond seed pairing. *Mol Cell* **27**, 91-105, doi:S1097-2765(07)00407-8 [pii] 10.1016/j.molcel.2007.06.017 (2007).

119 Betel, D., Wilson, M., Gabow, A., Marks, D. S. & Sander, C. The microRNA.org resource: targets and expression. *Nucleic Acids Res* **36**, D149-153, doi:gkm995 [pii] 10.1093/nar/gkm995 (2008).

120 Dweep, H., Sticht, C., Pandey, P. & Gretz, N. miRWalk--database: prediction of possible miRNA binding sites by "walking" the genes of three genomes. *J Biomed Inform* **44**, 839-847, doi:S1532-0464(11)00078-5 [pii] 10.1016/j.jbi.2011.05.002 (2011).

121 Meyer-Rochow, G. Y. *et al.* MicroRNA profiling of benign and malignant pheochromocytomas identifies novel diagnostic and therapeutic targets. *Endocrine-related cancer* **17**, 835-846, doi:10.1677/ERC-10-0142 (2010).

122 Tombol, Z. *et al.* MicroRNA expression profiling in benign (sporadic and hereditary) and recurring adrenal pheochromocytomas. *Modern pathology : an official journal of the United States and Canadian Academy of Pathology, Inc* **23**, 1583-1595, doi:10.1038/modpathol.2010.164 (2010).

123 Patterson, E. *et al.* The microRNA expression changes associated with malignancy and SDHB mutation in pheochromocytoma. *Endocrine-related cancer* **19**, 157-166, doi:10.1530/ERC-11-0308 (2012).

124 Stratton, M. R., Campbell, P. J. & Futreal, P. A. The cancer genome. *Nature* **458**, 719-724, doi:nature07943 [pii] 10.1038/nature07943 (2009).

125 Balmain, A., Gray, J. & Ponder, B. The genetics and genomics of cancer. *Nat Genet* **33 Suppl**, 238-244, doi:10.1038/ng1107 ng1107 [pii] (2003).

126 Dannenberg, H. *et al.* Losses of chromosomes 1p and 3q are early genetic events in the development of sporadic pheochromocytomas. *The American journal of pathology* **157**, 353-359, doi:10.1016/S0002-9440(10)64547-6 (2000).

127 van Nederveen, F. H. *et al.* Array-comparative genomic hybridization in sporadic benign pheochromocytomas. *Endocrine-related cancer* **16**, 505-513, doi:10.1677/ERC-08-0241 (2009).

128 Edstrom, E. *et al.* Comparative genomic hybridization reveals frequent losses of chromosomes 1p and 3q in pheochromocytomas and abdominal paragangliomas, suggesting a common genetic etiology. *The American journal of pathology* **156**, 651-659, doi:10.1016/S0002-9440(10)64769-4 (2000).

129 Jarbo, C. *et al.* Detailed assessment of chromosome 22 aberrations in sporadic pheochromocytoma using array-CGH. *Int J Cancer* **118**, 1159-1164, doi:10.1002/ijc.21385 (2006).

130 Korpershoek, E., Stobbe, C. K., van Nederveen, F. H., de Krijger, R. R. & Dinjens, W. N. Intra-tumoral molecular heterogeneity in benign and malignant pheochromocytomas and extra-adrenal sympathetic paragangliomas. *Endocr Relat Cancer* **17**, 653-662, doi:ERC-10-0072 [pii] 10.1677/ERC-10-0072 (2010).

131 Cascon, A. *et al.* A novel candidate region linked to development of both pheochromocytoma and head/neck paraganglioma. *Genes Chromosomes Cancer* **42**, 260-268, doi:10.1002/gcc.20139 (2005).

132 Sandgren, J. *et al.* Integrative epigenomic and genomic analysis of malignant pheochromocytoma. *Exp Mol Med* **42**, 484-502, doi:emm.2010.42.050 [pii] 10.3858/emm.2010.42.7.050 (2010).

133 Sandgren, J. *et al.* Recurrent genomic alterations in benign and malignant pheochromocytomas and paragangliomas revealed by whole-genome array comparative genomic hybridization analysis. *Endocrine-related cancer* **17**, 561-579, doi:10.1677/ERC-09-0310 (2010).

134 Bausch, B. *et al.* Germline NF1 mutational spectra and loss-of-heterozygosity analyses in patients with pheochromocytoma and neurofibromatosis type 1. *J Clin Endocrinol Metab* **92**, 2784-2792, doi:jc.2006-2833 [pii] 10.1210/jc.2006-2833 (2007).

135 Holland, A. J. & Cleveland, D. W. Boveri revisited: chromosomal instability, aneuploidy and tumorigenesis. *Nat Rev Mol Cell Biol* **10**, 478-487, doi:nrm2718 [pii] 10.1038/nrm2718 (2009).

136 Rajagopalan, H. & Lengauer, C. Aneuploidy and cancer. *Nature* **432**, 338-341, doi:nature03099 [pii] 10.1038/nature03099 (2004).

137 Campbell, L. L. & Polyak, K. Breast tumor heterogeneity: cancer stem cells or clonal evolution? *Cell Cycle* **6**, 2332-2338, doi:4914 [pii] (2007).

138 Witz, I. P. & Levy-Nissenbaum, O. The tumor microenvironment in the post-PAGET era. *Cancer Lett* **242**, 1-10, doi:S0304-3835(05)01056-6 [pii] 10.1016/j.canlet.2005.12.005 (2006).

139 Van Loo, P. *et al.* Allele-specific copy number analysis of tumors. *Proceedings of the National Academy of Sciences of the United States of America* **107**, 16910-16915, doi:10.1073/pnas.1009843107 (2010).

140 Blackhall, F. H. *et al.* Stability and heterogeneity of expression profiles in lung cancer specimens harvested following surgical resection. *Neoplasia* **6**, 761-767, doi:10.1593/neo.04301 (2004).

141 Cedar, H. & Bergman, Y. Programming of DNA methylation patterns. *Annu Rev Biochem* **81**, 97-117, doi:10.1146/annurev-biochem-052610-091920 (2012).

142 Lister, R. *et al.* Human DNA methylomes at base resolution show widespread epigenomic differences. *Nature* **462**, 315-322, doi:nature08514 [pii] 10.1038/nature08514 (2009).

143 Meissner, A. *et al.* Genome-scale DNA methylation maps of pluripotent and differentiated cells. *Nature* **454**, 766-770, doi:nature07107 [pii] 10.1038/nature07107 (2008).

144 Illingworth, R. *et al.* A novel CpG island set identifies tissue-specific methylation at developmental gene loci. *PLoS Biol* **6**, e22, doi:07-PLBI-RA-3186 [pii] 10.1371/journal.pbio.0060022 (2008).

145 Illingworth, R. S. *et al.* Orphan CpG islands identify numerous conserved promoters in the mammalian genome. *PLoS Genet* **6**, e1001134, doi:10.1371/journal.pgen.1001134 (2010).

146 Deaton, A. M. & Bird, A. CpG islands and the regulation of transcription. *Genes Dev* **25**, 1010-1022, doi:25/10/1010 [pii] 10.1101/gad.2037511 (2011).

147 Irizarry, R. A. *et al.* The human colon cancer methylome shows similar hypo- and hypermethylation at conserved tissue-specific CpG island shores. *Nat Genet* **41**, 178-186, doi:ng.298 [pii] 10.1038/ng.298 (2009).

148 Doi, A. *et al.* Differential methylation of tissue- and cancer-specific CpG island shores distinguishes human induced pluripotent stem cells, embryonic stem cells and fibroblasts. *Nat Genet* **41**, 1350-1353, doi:ng.471 [pii] 10.1038/ng.471 (2009).

149 Ji, H. *et al.* Comprehensive methylome map of lineage commitment from haematopoietic progenitors. *Nature* **467**, 338-342, doi:nature09367 [pii]10.1038/nature09367 (2010).

150 Wisniewski, J. R., Zougman, A. & Mann, M. Combination of FASP and StageTip-based fractionation allows in-depth analysis of the hippocampal membrane proteome. *Journal of proteome research* **8**, 5674-5678, doi:10.1021/pr900748n (2009).

151 Hellemans, J., Mortier, G., De Paepe, A., Speleman, F. & Vandesompele, J. qBase relative quantification framework and software for management and automated analysis of real-time quantitative PCR data. *Genome biology* **8**, R19, doi:10.1186/gb-2007-8-2-r19 (2007).

152 Hamada, N. *et al.* MicroRNA expression profiling of NGF-treated PC12 cells revealed a critical role for miR-221 in neuronal differentiation. *Neurochemistry international* **60**, 743-750, doi:10.1016/j.neuint.2012.03.010 (2012).

153 Sun, J. & Li, R. Human negative elongation factor activates transcription and regulates alternative transcription initiation. *The Journal of biological chemistry* **285**, 6443-6452, doi:10.1074/jbc.M109.084285 (2010).

154 Wisniewski, J. R., Zougman, A., Nagaraj, N. & Mann, M. Universal sample preparation method for proteome analysis. *Nature methods* **6**, 359-362, doi:10.1038/nmeth.1322 (2009).

155 Cox, J. & Mann, M. MaxQuant enables high peptide identification rates, individualized p.p.b.-range mass accuracies and proteome-wide protein quantification. *Nature biotechnology* **26**, 1367-1372, doi:10.1038/nbt.1511 (2008).

156 Luber, C. A. *et al.* Quantitative proteomics reveals subset-specific viral recognition in dendritic cells. *Immunity* **32**, 279-289, doi:10.1016/j.immuni.2010.01.013 (2010).

157 Simon-Sanchez, J. *et al.* Genome-wide SNP assay reveals structural genomic variation, extended homozygosity and cell-line induced alterations in normal individuals. *Human molecular genetics* **16**, 1-14, doi:10.1093/hmg/ddl436 (2007).

158 Bibikova, M. *et al.* Genome-wide DNA methylation profiling using Infinium(R) assay. *Epigenomics* **1**, 177-200, doi:10.2217/epi.09.14 (2009).

159 Murphy, S. K. *et al.* Epigenetic detection of human chromosome 14 uniparental disomy. *Human mutation* **22**, 92-97, doi:10.1002/humu.10237 (2003).

160 Zeschnigk, M., Lich, C., Buiting, K., Doerfler, W. & Horsthemke, B. A single-tube PCR test for the diagnosis of Angelman and Prader-Willi syndrome based on allelic methylation differences at the SNRPN locus. *European journal of human genetics : EJHG* **5**, 94-98 (1997).

161 Kubota, T. *et al.* Methylation-specific PCR simplifies imprinting analysis. *Nature genetics* **16**, 16-17, doi:10.1038/ng0597-15 (1997).

162 Gentleman, R. C. *et al.* Bioconductor: open software development for computational biology and bioinformatics. *Genome biology* **5**, R80, doi:10.1186/gb-2004-5-10-r80 (2004).

163 Lopez-Romero, P., Gonzalez, M. A., Callejas, S., Dopazo, A. & Irizarry, R. A. Processing of Agilent microRNA array data. *BMC research notes* **3**, 18, doi:10.1186/1756-0500-3-18 (2010).

164 de Hoon, M. J., Imoto, S., Nolan, J. & Miyano, S. Open source clustering software. *Bioinformatics* **20**, 1453-1454, doi:10.1093/bioinformatics/bth078 (2004).

165 Morrissey, E. R. & Diaz-Uriarte, R. Pomelo II: finding differentially expressed genes. *Nucleic acids research* **37**, W581-586, doi:10.1093/nar/gkp366 (2009).

166 Sales, G. *et al.* MAGIA, a web-based tool for miRNA and Genes Integrated Analysis. *Nucleic acids research* **38**, W352-359, doi:10.1093/nar/gkq423 (2010).

167 Cox, J. *et al.* Andromeda: a peptide search engine integrated into the MaxQuant environment. *Journal of proteome research* **10**, 1794-1805, doi:10.1021/pr101065j (2011).

168 Peiffer, D. A. *et al.* High-resolution genomic profiling of chromosomal aberrations using Infinium whole-genome genotyping. *Genome research* **16**, 1136-1148, doi:10.1101/gr.5402306 (2006).

169 Bibikova, M. *et al.* High-throughput DNA methylation profiling using universal bead arrays. *Genome research* **16**, 383-393, doi:10.1101/gr.4410706 (2006).

170 Du, P., Kibbe, W. A. & Lin, S. M. lumi: a pipeline for processing Illumina microarray. *Bioinformatics* **24**, 1547-1548, doi:10.1093/bioinformatics/btn224 (2008).

171 Du, P. *et al.* Comparison of Beta-value and M-value methods for quantifying methylation levels by microarray analysis. *BMC bioinformatics* **11**, 587, doi:10.1186/1471-2105-11-587 (2010).

172 Wilkerson, M. D. & Hayes, D. N. ConsensusClusterPlus: a class discovery tool with confidence assessments and item tracking. *Bioinformatics* **26**, 1572-1573, doi:10.1093/bioinformatics/btq170 (2010).

173 Gu, Z., Gu, L., Eils, R., Schlesner, M. & Brors, B. circlize implements and enhances circular visualization in R. *Bioinformatics*, doi:10.1093/bioinformatics/btu393 (2014).

174 de Cubas, A. A. *et al.* Integrative analysis of miRNA and mRNA expression profiles in pheochromocytoma and paraganglioma identifies genotype-specific markers and potentially regulated pathways. *Endocrine-related cancer* **20**, 477-493, doi:10.1530/ERC-12-0183 (2013).

175 Carling, T., Du, Y., Fang, W., Correa, P. & Huang, S. Intragenic allelic loss and promoter hypermethylation of the RIZ1 tumor suppressor gene in parathyroid tumors and pheochromocytomas. *Surgery* **134**, 932-939; discussion 939-940, doi:10.1016/S0039 (2003).

176 Song, J., Kim, D. & Jin, E. J. MicroRNA-488 suppresses cell migration through modulation of the focal adhesion activity during chondrogenic differentiation of chick limb mesenchymal cells. *Cell biology international* **35**, 179-185, doi:10.1042/CBI20100204 (2011).

177 Afanasyeva, E. A. *et al.* MicroRNA miR-885-5p targets CDK2 and MCM5, activates p53 and inhibits proliferation and survival. *Cell death and differentiation* **18**, 974-984, doi:10.1038/cdd.2010.164 (2011).

178 Li, Z. *et al.* A microRNA signature for a BMP2-induced osteoblast lineage commitment program. *Proceedings of the National Academy of Sciences of the United States of America* **105**, 13906-13911, doi:10.1073/pnas.0804438105 (2008).

179 Kim, J. *et al.* A MicroRNA feedback circuit in midbrain dopamine neurons. *Science* **317**, 1220-1224, doi:10.1126/science.1140481 (2007).

180 Kano, M. *et al.* miR-145, miR-133a and miR-133b: Tumor-suppressive miRNAs target FSCN1 in esophageal squamous cell carcinoma. *International journal of cancer. Journal international du cancer* **127**, 2804-2814, doi:10.1002/ijc.25284 (2010).

181 Miko, E. *et al.* Differentially expressed microRNAs in small cell lung cancer. *Experimental lung research* **35**, 646-664, doi:10.3109/01902140902822312 (2009).

182 Chan, S. Y. & Loscalzo, J. MicroRNA-210: a unique and pleiotropic hypoxamir. *Cell cycle* **9**, 1072-1083 (2010).

183 Puissegur, M. P. *et al.* miR-210 is overexpressed in late stages of lung cancer and mediates mitochondrial alterations associated with modulation of HIF-1 activity. *Cell death and differentiation* **18**, 465-478, doi:10.1038/cdd.2010.119 (2011).

184 Maher, E. R. & Eng, C. The pressure rises: update on the genetics of phaeochromocytoma. *Human molecular genetics* **11**, 2347-2354 (2002).

185 Raimundo, N., Baysal, B. E. & Shadel, G. S. Revisiting the TCA cycle: signaling to tumor formation. *Trends in molecular medicine* **17**, 641-649, doi:10.1016/j.molmed.2011.06.001 (2011).

186 Vohwinkel, C. U. *et al.* Elevated CO(2) levels cause mitochondrial dysfunction and impair cell proliferation. *The Journal of biological chemistry* **286**, 37067-37076, doi:10.1074/jbc.M111.290056 (2011).

187 Borodovsky, A., Seltzer, M. J. & Riggins, G. J. Altered cancer cell metabolism in gliomas with mutant IDH1 or IDH2. *Current opinion in oncology* **24**, 83-89, doi:10.1097/CCO.0b013e32834d816a (2012).

188 Tanaka, H. *et al.* MicroRNA-183 upregulates HIF-1alpha by targeting isocitrate dehydrogenase 2 (IDH2) in glioma cells. *Journal of neuro-oncology* **111**, 273-283, doi:10.1007/s11060-012-1027-9 (2013).

189 Tarantino, C. *et al.* miRNA 34a, 100, and 137 modulate differentiation of mouse embryonic stem cells. *FASEB journal : official publication of the Federation of American Societies for Experimental Biology* **24**, 3255-3263, doi:10.1096/fj.09-152207 (2010).

190 Thayanithy, V. *et al.* Perturbation of 14q32 miRNAs-cMYC gene network in osteosarcoma. *Bone* **50**, 171-181, doi:10.1016/j.bone.2011.10.012 (2012).

191 Kriegel, A. J. *et al.* MicroRNA-target pairs in human renal epithelial cells treated with transforming growth factor beta 1: a novel role of miR-382. *Nucleic acids research* **38**, 8338-8347, doi:10.1093/nar/gkq718 (2010).

192 Garzon, R., Calin, G. A. & Croce, C. M. MicroRNAs in Cancer. *Annual review of medicine* **60**, 167-179, doi:10.1146/annurev.med.59.053006.104707 (2009).

193 Altuvia, Y. *et al.* Clustering and conservation patterns of human microRNAs. *Nucleic acids research* **33**, 2697-2706, doi:10.1093/nar/gki567 (2005).

194 Yuan, X. *et al.* Clustered microRNAs' coordination in regulating protein-protein interaction network. *BMC systems biology* **3**, 65, doi:10.1186/1752-0509-3-65 (2009).

195 Astuti, D. *et al.* Epigenetic alteration at the DLK1-GTL2 imprinted domain in human neoplasia: analysis of neuroblastoma, phaeochromocytoma and Wilms' tumour. *British journal of cancer* **92**, 1574-1580, doi:10.1038/sj.bjc.6602478 (2005).

196 Ikeda, Y., Tanji, E., Makino, N., Kawata, S. & Furukawa, T. MicroRNAs associated with mitogen-activated protein kinase in human pancreatic cancer. *Molecular cancer research : MCR* **10**, 259-269, doi:10.1158/1541-7786.MCR-11-0035 (2012).

197 Grenningloh, G., Soehrman, S., Bondallaz, P., Ruchti, E. & Cadas, H. Role of the microtubule destabilizing proteins SCG10 and stathmin in neuronal growth. *Journal of neurobiology* **58**, 60-69, doi:10.1002/neu.10279 (2004).

198 Bjorklund, P. *et al.* Stathmin as a marker for malignancy in pheochromocytomas. *Experimental and clinical endocrinology & diabetes : official journal, German Society of Endocrinology [and] German Diabetes Association* **118**, 27-30, doi:10.1055/s-0029-1202789 (2010).

199 Siu, Y. T. & Jin, D. Y. CREB--a real culprit in oncogenesis. *The FEBS journal* **274**, 3224-3232, doi:10.1111/j.1742-4658.2007.05884.x (2007).

200 Obara, Y. *et al.* ERK5 activity is required for nerve growth factor-induced neurite outgrowth and stabilization of tyrosine hydroxylase in PC12 cells. *The Journal of biological chemistry* **284**, 23564-23573, doi:10.1074/jbc.M109.027821 (2009).

201 Jiang, S. & Dahia, P. L. Minireview: the busy road to pheochromocytomas and paragangliomas has a new member, TMEM127. *Endocrinology* **152**, 2133-2140, doi:10.1210/en.2011-0052 (2011).

202 Watanabe, K. *et al.* Latent process genes for cell differentiation are common decoders of neurite extension length. *Journal of cell science* **125**, 2198-2211, doi:10.1242/jcs.097709 (2012).

203 Weeraratne, S. D. *et al.* Pleiotropic effects of miR-183~96~182 converge to regulate cell survival, proliferation and migration in medulloblastoma. *Acta neuropathologica* **123**, 539-552, doi:10.1007/s00401-012-0969-5 (2012).

204 Yeo, M. *et al.* Small CTD phosphatases function in silencing neuronal gene expression. *Science* **307**, 596-600, doi:10.1126/science.1100801 (2005).

205 Maeda, M. *et al.* ARHGAP18, a GTPase-activating protein for RhoA, controls cell shape, spreading, and motility. *Molecular biology of the cell* **22**, 3840-3852, doi:10.1091/mbc.E11-04-0364 (2011).

206 Zhuang, B., Su, Y. S. & Sockanathan, S. FARP1 promotes the dendritic growth of spinal motor neuron subtypes through transmembrane Semaphorin6A and PlexinA4 signaling. *Neuron* **61**, 359-372, doi:10.1016/j.neuron.2008.12.022 (2009).

207 Ko, J. & Kim, E. Leucine-rich repeat proteins of synapses. *Journal of neuroscience research* **85**, 2824-2832, doi:10.1002/jnr.21306 (2007).

208 Sperka, T. *et al.* Activation of Ras requires the ERM-dependent link of actin to the plasma membrane. *PloS one* **6**, e27511, doi:10.1371/journal.pone.0027511 (2011).

209 Klesse, L. J., Meyers, K. A., Marshall, C. J. & Parada, L. F. Nerve growth factor induces survival and differentiation through two distinct signaling cascades in PC12 cells. *Oncogene* **18**, 2055-2068, doi:10.1038/sj.onc.1202524 (1999).

210 Nowell, P. C. & Hungerford, D. A. Chromosome studies in human leukemia. II. Chronic granulocytic leukemia. *Journal of the National Cancer Institute* **27**, 1013-1035 (1961).

211 Moley, J. F. *et al.* Consistent association of 1p loss of heterozygosity with pheochromocytomas from patients with multiple endocrine neoplasia type 2 syndromes. *Cancer research* **52**, 770-774 (1992).

212 Vargas, M. P. *et al.* Loss of heterozygosity on the short arm of chromosomes 1 and 3 in sporadic pheochromocytoma and extra-adrenal paraganglioma. *Human pathology* **28**, 411-415 (1997).

213 Crona, J. *et al.* Somatic mutations in H-RAS in sporadic pheochromocytoma and paraganglioma identified by exome sequencing. *The Journal of clinical endocrinology and metabolism* **98**, E1266-1271, doi:10.1210/jc.2012-4257 (2013).

214 Kralovics, R. *et al.* A gain-of-function mutation of JAK2 in myeloproliferative disorders. *The New England journal of medicine* **352**, 1779-1790, doi:10.1056/NEJMoa051113 (2005).

215 Komotar, R. J., Otten, M. L., Starke, R. M. & Anderson, R. C. Chromosome 1p and 11q deletions and outcome in neuroblastoma-a critical review. *Clinical medicine. Oncology* **2**, 419-420 (2008).

216 Yeh, I. T. *et al.* A germline mutation of the KIF1B beta gene on 1p36 in a family with neural and nonneural tumors. *Human genetics* **124**, 279-285, doi:10.1007/s00439-008-0553-1 (2008).

217 Petri, B. J. *et al.* Frequent loss of 17p, but no p53 mutations or protein overexpression in benign and malignant pheochromocytomas. *Modern pathology : an official journal of the United States and Canadian Academy of Pathology, Inc* **21**, 407-413, doi:10.1038/modpathol.3801013 (2008).

218 Huang, S. C. *et al.* Duplication of the mutant RET allele in trisomy 10 or loss of the wild-type allele in multiple endocrine neoplasia type 2-associated pheochromocytomas. *Cancer research* **60**, 6223-6226 (2000).

219 Deyell, R. J. & Attiyeh, E. F. Advances in the understanding of constitutional and somatic genomic alterations in neuroblastoma. *Cancer genetics* **204**, 113-121, doi:10.1016/j.cancergen.2011.03.001 (2011).

220 Astuti, D. *et al.* RASSF1A promoter region CpG island hypermethylation in phaeochromocytomas and neuroblastoma tumours. *Oncogene* **20**, 7573-7577, doi:10.1038/sj.onc.1204968 (2001).

221 Geli, J. *et al.* The Ras effectors NORE1A and RASSF1A are frequently inactivated in pheochromocytoma and abdominal paraganglioma. *Endocrine-related cancer* **14**, 125-134, doi:10.1677/ERC-06-0031 (2007).

222 Killian, J. K. *et al.* Succinate dehydrogenase mutation underlies global epigenomic divergence in gastrointestinal stromal tumor. *Cancer discovery* **3**, 648-657, doi:10.1158/2159-8290.CD-13-0092 (2013).

223 Borssen, M. *et al.* Promoter DNA methylation pattern identifies prognostic subgroups in childhood T-cell acute lymphoblastic leukemia. *PloS one* **8**, e65373, doi:10.1371/journal.pone.0065373 (2013).

224 Abe, M. *et al.* CpG island methylator phenotype is a strong determinant of poor prognosis in neuroblastomas. *Cancer research* **65**, 828-834 (2005).

225 Noushmehr, H. *et al.* Identification of a CpG island methylator phenotype that defines a distinct subgroup of glioma. *Cancer cell* **17**, 510-522, doi:10.1016/j.ccr.2010.03.017 (2010).

226 Amar, L. *et al.* Genetic testing in pheochromocytoma or functional paraganglioma. *Journal of clinical oncology : official journal of the American Society of Clinical Oncology* **23**, 8812-8818, doi:10.1200/JCO.2005.03.1484 (2005).

227 Xu, W. *et al.* Oncometabolite 2-hydroxyglutarate is a competitive inhibitor of alpha-ketoglutarate-dependent dioxygenases. *Cancer cell* **19**, 17-30, doi:10.1016/j.ccr.2010.12.014 (2011).

228 Anderson, D. J. & Michelsohn, A. Role of glucocorticoids in the chromaffin-neuron developmental decision. *International journal of developmental neuroscience : the official journal of the International Society for Developmental Neuroscience* **7**, 475-487 (1989).

229 Huynh, T. T. *et al.* Transcriptional regulation of phenylethanolamine N-methyltransferase in pheochromocytomas from patients with von Hippel-Lindau syndrome and multiple endocrine neoplasia type 2. *Annals of the New York Academy of Sciences* **1073**, 241-252, doi:10.1196/annals.1353.026 (2006).

230 Lu, K. H. *et al.* Long non-coding RNA MEG3 inhibits NSCLC cells proliferation and induces apoptosis by affecting p53 expression. *BMC cancer* **13**, 461, doi:10.1186/1471-2407-13-461 (2013).

231 Bagui, T. K., Sharma, S. S., Ma, L. & Pledger, W. J. Proliferative status regulates HDAC11 mRNA abundance in nontransformed fibroblasts. *Cell cycle* **12**, 3433-3441, doi:10.4161/cc.26433 (2013).

232 Nikoletopoulou, V. *et al.* Neurotrophin receptors TrkA and TrkC cause neuronal death whereas TrkB does not. *Nature* **467**, 59-63, doi:10.1038/nature09336 (2010).

233 Bredesen, D. E., Mehlen, P. & Rabizadeh, S. Receptors that mediate cellular dependence. *Cell death and differentiation* **12**, 1031-1043, doi:10.1038/sj.cdd.4401680 (2005).

234 Jackson, R. S., 2nd, Cho, Y. J., Stein, S. & Liang, P. CYFIP2, a direct p53 target, is leptomycin-B sensitive. *Cell cycle* **6**, 95-103 (2007).

235 Pittman, A. J., Gaynes, J. A. & Chien, C. B. nev (cyfip2) is required for retinal lamination and axon guidance in the zebrafish retinotectal system. *Developmental biology* **344**, 784-794, doi:10.1016/j.ydbio.2010.05.512 (2010).

236 Mongroo, P. S. *et al.* IMP-1 displays cross-talk with K-Ras and modulates colon cancer cell survival through the novel proapoptotic protein CYFIP2. *Cancer research* **71**, 2172-2182, doi:10.1158/0008-5472.CAN-10-3295 (2011).

237 Ren, F., Wang, D. B. & Li, T. [Epigenetic inactivation of SPOCK2 in the malignant transformation of ovarian endometriosis]. *Zhonghua fu chan ke za zhi* **46**, 822-825 (2011).

238 Schnepp, A. *et al.* Mouse testican-2. Expression, glycosylation, and effects on neurite outgrowth. *The Journal of biological chemistry* **280**, 11274-11280, doi:10.1074/jbc.M414276200 (2005).

239 Kramps, T. *et al.* Wnt/wingless signaling requires BCL9/legless-mediated recruitment of pygopus to the nuclear beta-catenin-TCF complex. *Cell* **109**, 47-60 (2002).

240 Yamaguchi, Y. *et al.* NELF, a multisubunit complex containing RD, cooperates with DSIF to repress RNA polymerase II elongation. *Cell* **97**, 41-51 (1999).

241 Yamaguchi, Y., Inukai, N., Narita, T., Wada, T. & Handa, H. Evidence that negative elongation factor represses transcription elongation through binding to a DRB sensitivity-inducing factor/RNA polymerase II complex and RNA. *Molecular and cellular biology* **22**, 2918-2927 (2002).

242 Aida, M. *et al.* Transcriptional pausing caused by NELF plays a dual role in regulating immediate-early expression of the junB gene. *Molecular and cellular biology* **26**, 6094-6104, doi:10.1128/MCB.02366-05 (2006).

243 Kanno, T. *et al.* JunB promotes cell invasion and angiogenesis in VHL-defective renal cell carcinoma. *Oncogene* **31**, 3098-3110, doi:10.1038/onc.2011.475 (2012).

244 Stamenkovic, I. Matrix metalloproteinases in tumor invasion and metastasis. *Seminars in cancer biology* **10**, 415-433, doi:10.1006/scbi.2000.0379 (2000).

245 van Veelen, W. *et al.* P18 is a tumor suppressor gene involved in human medullary thyroid carcinoma and pheochromocytoma development. *International journal of cancer. Journal international du cancer* **124**, 339-345, doi:10.1002/ijc.23977 (2009).

246 Peng, D. F. *et al.* Silencing of glutathione peroxidase 3 through DNA hypermethylation is associated with lymph node metastasis in gastric carcinomas. *PloS one* **7**, e46214, doi:10.1371/journal.pone.0046214 (2012).

247 Habashy, H. O. *et al.* RERG (Ras-like, oestrogen-regulated, growth-inhibitor) expression in breast cancer: a marker of ER-positive luminal-like subtype. *Breast cancer research and treatment* **128**, 315-326, doi:10.1007/s10549-010-1073-y (2011).

248 Kim, J. K. *et al.* PDZ domain-containing 1 (PDZK1) protein regulates phospholipase C-beta3 (PLC-beta3)-specific activation of somatostatin by forming a ternary complex with PLC-beta3 and somatostatin receptors. *The Journal of biological chemistry* **287**, 21012-21024, doi:10.1074/jbc.M111.337865 (2012).

8. SUPPLEMENTARY MATERIAL

All supplemental material provided in attached CD.

Supplementary Table 3.1. Detailed description of samples used in miRNA study.

Supplementary Table 3.2. Detailed description of samples used in methylation study

Supplementary Table 4.2.1. Differentially expressed miRNAs

Supplementary Table 4.2.2. Predicted miRNA-mRNA interactions by MAGIA integration

Supplementary Table 4.2.3. Pathway Analysis for commonly deregulated miRNAs

Supplementary Table 4.2.4. Pathway analysis of miRNAs in each PPGL genetic group

Supplementary Table 4.2.5. Pathway analysis for 14q32.2 miRNA cluster

9. PRIMARY PUBLICATIONS

These publications involved the use of high-throughput technologies described within this thesis, Publication 9.10 was included because, although I had just joined the Lab, I was included as a coauthor, and I basically learned how to do these analyses starting from this publication.

9.1. DNA methylation profiling of pheochromocytoma and paraganglioma reveals malignancy-associated CpGs independent of genetic background.

de Cubas AA, Koepershoek E, Inglada-Pérez L, Letouzé E, Maria Currás-Freixes, Fernández AF, Comino-Méndez I, Schiavi F, Mancikova V, Eisenhofer G, Mannelli M, Opocher G, Timmers H, Beuschlein F, de Krijger R, Cascon A, Fraga MF, Favier J, Gimenez-Roqueplo A, Robledo M.

Clin Cancer Res. 2014. (Submitted).

9.2. Krebs Cycle Metabolite Profiling for Indentification and stratification of Pheochromocytomas/Paragangliomas due to Succinate Dehydrogenase Deficiency.

Richter S, Peitzsch M, Rapizzi E, Lenders JW, Qin N, de Cubas AA, Schiavi F, Rao JU, Beuschlein F, Quinkler M, Timmers HJ, Opocher G, Mannelli M, Pacak K, Robledo M, Eisenhofer G.

J Clin Endocrinol Metab. 2014 Jul 11.

9.3. Opposing effects of HIF1α and HIF2α on chromaffin cell phenotypic features and tumor cell proliferation: insights from MYC-associated factor X.

Qin N, de Cubas AA, Garia-Martin R, Richter S, Peitzsch M, Menschikowski M, Lender JW, Timmers HJ, Mannelli M, Opocher G, Economopoulou M, Siegert G, Chavakis T, Pacak K, Robledo M, Eisenhofer G.

Int J Cancer. 2014 Nov; 135(9):2054-64.

9.4. Germline mutations in FH confer predisposition to malignant pheochromocytomas and paragangliomas.

Castro-Vega LJ*, Buffet A*, De Cubas AA*, Cascón A, Menara M, Khalifa E, Amar L, Azriel S, Bourdeau I, Chabre O, Currás-Freixes M, Franco-Vidal V, Guillaud-Bataille M, Simian C, Morin A, Letón R, Gómez-Graña A, Pollard PJ, Rustin P, Robledo M#, Favier J#, Gimenez-Roqueplo AP#.

Hum Mol Genet. 2014 May; 23(9):2440-6.

*: First Authors. #: Second Authors.

9.5. Integrative analysis of miRNA and mRNA expression profiles in pheochromocytoma and paraganglioma identifies genotype-specific markers and potentially regulated pathways.

de Cubas AA, Leandro-García LJ, Schiavi F, Mancikova V, Comino-Méndez I, Inglada-Pérez L, Perez-Martinez M, Ibarz N, Ximénez-Embún P, López-Jiménez E, Maliszewska A, Letón R, Gómez Graña A, Bernal C, Alvarez-Escolá C, Rodríguez-Antona C, Opocher G, Muñoz J, Megias D, Cascón A, Robledo M.

Endocr Relat Cancer. 2013 Jun 24;20(4):477-93.

9.6. Tumoral EPAS1 (HIF2A) mutations explain sporadic pheochromocytoma and paraganglioma in the absence of erythrocytosis.

Comino-Méndez I, de Cubas AA, Bernal C, Álvarez-Escolá C, Sánchez-Malo C, Ramírez-Tortosa CL, Pedrinaci S, Rapizzi E, Ercolino T, Bernini G, Bacca A, Letón R, Pita G, Alonso MR, Leandro-García LJ, Gómez-Graña A, Inglada-Pérez L, Mancikova V, Rodríguez-Antona C, Mannelli M, Robledo M, Cascón A.

Hum Mol Genet. 2013 Jun 1;22(11):2169-76.

9.7. MAX mutations cause hereditary and sporadic pheochromocytoma and paraganglioma.

Burnichon N, Cascón A, Schiavi F, Morales NP, Comino-Méndez I, Abermil N, Inglada-Pérez L, de Cubas AA, Amar L, Barontini M, de Quirós SB, Bertherat J, Bignon YJ, Blok MJ, Bobisse S, Borrego S, Castellano M, Chanson P, Chiara MD, Corssmit EP, Giacchè M, de Krijger RR, Ercolino T, Girerd X, Gómez-García EB, Gómez-Graña A, Guilhem I, Hes FJ, Honrado E, Korpershoek E, Lenders JW, Letón R, Mensenkamp AR, Merlo A, Mori L, Murat A, Pierre P, Plouin PF, Prodanov T, Quesada-Charneco M, Qin N, Rapizzi E, Raymond V, Reisch N, Roncador G, Ruiz-Ferrer M, Schillo F, Stegmann AP, Suarez C, Taschin E, Timmers HJ, Tops CM, Urioste M, Beuschlein F, Pacak K, Mannelli M, Dahia PL, Opocher G, Eisenhofer G, Gimenez-Roqueplo AP, Robledo M.

Clin Cancer Res. 2012 May 15;18(10):2828-37.

9.8. Thyroid paraganglioma. Report of 3 cases and description of an immunohistochemical profile useful in the differential diagnosis with medullary thyroid carcinoma, based on complementary DNA array results.

Castelblanco E, Gallel P, Ros S, Gatius S, Valls J, De-Cubas AA, Maliszewska A, Yebra-Pimentel MT, Menarguez J, Gamallo C, Opocher G, Robledo M, Matias-Guiu X.

Hum Pathol. 2012 Jul;43(7):1103-12.

9.9. Exome sequencing identifies MAX mutations as a cause of hereditary pheochromocytoma.

Comino-Méndez I*****, Gracia-Aznárez FJ*****, Schiavi F, Landa I, Leandro-García LJ, Letón R, Honrado E, Ramos-Medina R, Caronia D, Pita G, Gómez-Graña A, de Cubas AA, Inglada-Pérez L, Maliszewska A, Taschin E, Bobisse S, Pica G, Loli P, Hernández-Lavado R, Díaz JA, Gómez-Morales M, González-Neira A, Roncador G, Rodríguez-Antona C, Benítez J, Mannelli M, Opocher G, Robledo M[#], Cascón A.[#]

Nat Genet. 2011 Jun 19;43(7):663-7.

*: First Authors. #: Second Authors.

9.10. Research resource: Transcriptional profiling reveals different pseudohypoxic signatures in SDHB and VHL-related pheochromocytomas.

López-Jiménez E, Gómez-López G, Leandro-García LJ, Muñoz I, Schiavi F, Montero-Conde C, de Cubas AA, Ramires R, Landa I, Leskelä S, Maliszewska A, Inglada-Pérez L, de la Vega L, Rodríguez-Antona C, Letón R, Bernal C, de Campos JM, Diez-Tascón C, Fraga MF, Boullosa C, Pisano DG, Opocher G, Robledo M, Cascón A.

Mol Endocrinol. 2010 Dec;24(12):2382-91.

10. OTHER PUBLICATIONS

VEGF, VEGFR3, and PDGFRB Protein Expression Is Influenced by RAS Mutations in Medullary Thyroid Carcinoma.

Mancikova V, Inglada-Pérez L, Curras-Freixes M, de Cubas AA, Gómez A, Letón R, Kersten I, Leandro-García LJ, Comino-Méndez I, Apellaniz-Ruiz M, Sánchez L, Cascón A, Sastre-Marcos J, García JF, Rodríguez-Antona C, Robledo M. *Thyroid.* 2014 Aug; 24(8):1251-5.

H-RAS mutations are restricted to sporadic pheochromocytomas lacking specific clinical or pathological feature: data from a multi-institutional series.

Oudijk L, de Krijger RR, Rapa I, Beuschlein F, de Cubas AA, Dei Tos AP, Dinjens WN, Korpershoek E, Mancikova V, Mannelli M, Papotti M, Vatrano S, Robledo M, Volante M. *J Clin Endcrinol Metab.* 2014 Jul; 99(7):E1376-80.

DNA methylation profiling of well-differentiated thyroid cancer uncovers markers of recurrence free survival.

Mancikova V, Buj R, Castelblanco E, Inglada-Pérez L, Diez A, de Cubas AA, Curras-Freixes M, Maravall FX, Mauricio D, Matias-Guiu X, Puig-Domingo M, Capel I, Bella MR, Lerma E, Castella E, Reverter JL, Peinado MA, Jorda M, Robledo M. *Int J Cancer.* 2014 Aug; 135(3):598-610.

Usefulness of Negative and Weak-Diffuse Pattern of SDHB Immunostaining in Assessment of SDH Mutations in Paraganglioma and Pheochromocytoma.

Castelblanco E, Santacana M, Valls J, de Cubas A, Cascón A, Robledo M, Matias-Guiu X. *Endocr Pathol.* 2013 Dec;24(4):199-205.

Influence of RET mutations on the expression of tyrosine kinases in medullary thyroid carcinoma.

Rodríguez-Antona C, Muñoz-Repeto I, Inglada-Pérez L, de Cubas AA, Mancikova V, Cañamero M, Maliszewska A, Gómez A, Letón R, Leandro-García LJ, Comino-Méndez I, Sanchez L, Alvarez-Escolá C, Aller J, Cascón A, Robledo M.

Endocr Relat Cancer. 2013 Jul 12;20(4):611-9.

Genetics of pheochromocytoma and paraganglioma in Spanish pediatric patients.

Cascón A, Inglada-Pérez L, Comino-Méndez I, de Cubas AA, Letón R, Mora J, Marazuela M, Galofré JC, Quesada-Charneco M, Robledo M. *Endocr Relat Cancer.* 2013 May 30;20(3):L1-6.

Differential gene expression of medullary thyroid carcinoma reveals specific markers associated with genetic conditions.

Maliszewska A, Leandro-Garcia LJ, Castelblanco E, Macià A, de Cubas A, Goméz-López G, Inglada-Pérez L, Álvarez-Escolá C, De la Vega L, Letón R, Gómez-Graña Á, Landa I, Cascón A, Rodríguez-Antona C, Borrego S, Zane M, Schiavi F, Merante-Boschin I, Pelizzo MR, Pisano DG, Opocher G, Matias-Guiu X, Encinas M, Robledo M. *Am J Pathol.* 2013 Feb;182(2):350-62.

Hematologic β-tubulin VI isoform exhibits genetic variability that influences paclitaxel toxicity.

Leandro-García LJ, Leskelä S, Inglada-Pérez L, Landa I, de Cubas AA, Maliszewska A, Comino-Méndez I, Letón R, Gómez-Graña Á, Torres R, Ramírez JC, Álvarez S, Rivera J, Martínez C, Lozano ML, Cascón A, Robledo M, Rodríguez-Antona C. *Cancer Res.* 2012 Sep 15;72(18):4744-52.

Regulatory polymorphisms in β-tubulin IIa are associated with paclitaxel-induced peripheral neuropathy.

Leandro-García LJ, Leskelä S, Jara C, Gréen H, Avall-Lundqvist E, Wheeler HE, Dolan ME, Inglada-Perez L, Maliszewska A, de Cubas AA, Comino-Méndez I, Mancikova V, Cascón A, Robledo M, Rodríguez-Antona C. *Clin Cancer Res.* 2012 Aug 15;18(16):4441-8.